The Stacked Value of Battery Energy Storage Systems

Final Project Report

M-41

Power Systems Engineering Research Center
Empowering Minds to Engineer
the Future Electric Energy System

The Stacked Value of Battery Energy Storage Systems

Final Project Report

Project Team

Meng Wu, Project Leader
Arizona State University

Josue Campos do Prado
Washington State University

Graduate Students

Reza Khalilisenobari
Mohammad Mousavi
Zhongxia Zhang
Arizona State University

Ugonna Chikezie
Washington State University

PSERC Publication 21-07

August 2021

For information about this project, contact:

Meng Wu
Arizona State University
School of Electrical, Computer and Energy Engineering
P.O. Box 875706
Tempe, AZ, 85287-5706
Phone: (480) 965-8706
Email: mwu@asu.edu

Power Systems Engineering Research Center

The Power Systems Engineering Research Center (PSERC) is a multi-university Center conducting research on challenges facing the electric power industry and educating the next generation of power engineers. More information about PSERC can be found at the Center's website: http://www.pserc.org.

For additional information, contact:

Power Systems Engineering Research Center
Arizona State University
527 Engineering Research Center
Tempe, Arizona 85287-5706
Phone: 480-965-1643
Fax: 480-727-2052

Notice Concerning Copyright Material

Acknowledgements

This is the final report for the Power Systems Engineering Research Center (PSERC) research project titled "The Stacked Value of Battery Energy Storage Systems" (Project M-41).

The authors would like to thank all the industry advisors for their valuable feedback: Liwei Hao (GE), Yazhou Jiang (GE), Jesse Gantz (Centrica), Bernardo Orvananos (Centrica), Tongxin Zheng (ISO-NE), Di Shi (GEIRI North America), Zhiwei Wang (GEIRI North America), Xiaohu Zhang (GEIRI North America), Zhe Yu (GEIRI North America), Yishen Wang (GEIRI North America), Robert Hess (SRP-Retired), Harvey Scribner (SPP), Jay Caspary (SPP), Doug Bowman (SPP), Ben Kroposki (NREL), Yingchen Zhang (NREL), Santosh Veda (NREL), Akshay Korad (MISO), Michaela Flagg (MISO), Aditya Jayam Prabhakar (MISO), Mark Westendorf (MISO), Jau J Guo (AEP), Evan R. Wilcox (AEP), Yazan M. Alsmadi (AEP), Tom Weaver III (AEP), John H. Tucker (AEP), Cho Wang (AEP), Yohan Sutjandra (The Energy Authority).

Executive Summary

This project is motivated by the growing integration of utility-scale and distributed energy storage resources in both transmission and distribution systems. As US Federal Energy Regulatory Commission (FERC) Orders No. 841 and No. 2222 request all the US system operators to completely open their energy and ancillary services markets to both utility-scale and retail-scale (distributed) energy storage resources, these energy storage resources bring in various challenges to the wholesale market operation and participation. This research focuses on three core areas: 1) understanding market participation activities of utility-scale batteries in the wholesale energy, reserve, and regulation markets; 2) data-driven day-ahead and real-time price forecasting approaches for profit-seeking utility-scale batteries and aggregators of distributed batteries; and 3) the distribution system operator (DSO) framework for coordinating market participation activities of distributed batteries and other distributed resources. The research is presented in six chapters (Chapters 2-7).

Chapters 2-3 present a comprehensive modeling framework for studying various market participation activities and operating patterns of utility-scale batteries in the energy and ancillary services markets, with detailed consideration of batteries' regulation market participation models and degradation cost models. Analysis on the impact of battery degradation on market participation strategies of utility-scale batteries is presented in Chapter 3.

Chapter 4 describes a framework for integrating BESSs in the wholesale and retail electricity markets and presents a case study on the integration of BESSs and virtual bidding on the decision-making model of an electricity retailer through a two-stage stochastic optimization framework.

Chapter 5-6 propose data-driven price forecasting approaches with improved forecasting accuracy, for profit-seeking battery owners and aggregators to forecast system-wide day-ahead and real- time locational marginal prices using public market data. The proposed approaches are built upon generative adversarial networks and convolutional long short-term memory networks which capture the spatio-temporal correlations among system-wide energy market data.

Chapter 7 presents a DSO framework to optimally coordinate the aggregators of various distributed resources for their wholesale market participation while operating the retail market, considering three-phase unbalanced distribution system operating constraints, as well as coordinated market clearing mechanisms between the balanced wholesale and unbalanced retail markets.

Project Publications:

[1] Reza Khalilisenobari and Meng Wu, "Optimal Participation of Price-maker Battery Energy Storage Systems in Energy, Reserve and Pay as Performance Regulation Markets," *51st North American Power Symposium (NAPS)*, Wichita, KS, USA, 2019 (Selected in Best Conference Paper Sessions).

[2] Mohammad Mousavi and Meng Wu, "A DSO Framework for Comprehensive Market Participation of DER Aggregators," *2020 IEEE PES General Meeting*, Virtual Conference, 2020.

[3] Zhongxia Zhang and Meng Wu, "Real-time Locational Marginal Price Forecasting using Generative Adversarial Network*", 2020 IEEE International Conference on Communica-*

tions, Control, and Computing Technologies for Smart Grids (SmartGridComm), Virtual Conference, 2020.

[4] Reza Khalilisenobari and Meng Wu, "Impact of Battery Degradation on Market Participation of Utility-scale Batteries: Case Studies", *52nd North American Power Symposium (NAPS)*, Virtual Conference, 2021.

[5] Mohammad Mousavi and Meng Wu, "Two-stage Stochastic Programming DSO Framework for Comprehensive Market Participation of DER Aggregators under Uncertainty", *52nd North American Power Symposium (NAPS)*, Virtual Conference, 2021.

[6] Zhongxia Zhang and Meng Wu, "Locational Marginal Price Forecasting using Convolutional Long Short-term Memory based Generative Adversarial Network", *2021 IEEE PES General Meeting*, Virtual Conference, 2021 (Selected in Best Conference Paper Sessions).

[7] Zhongxia Zhang and Meng Wu, "Predicting Real-Time Locational Marginal Prices: A GAN-Based Approach", *IEEE Transactions on Power Systems*, Accepted, to appear.

[8] U. Chikezie and Z. Chen, "Literature review of energy storage for power system economics," *2020 IEEE 3rd International Conference on Renewable Energy and Power Engineering (REPE)*, Virtual Conference, 2020.

[9] U. Chikezie, T. Karacolak, and J. C. do Prado, "Examining the applicability of blockchain to the smart grid using proof-of-authority consensus," *9th IEEE International Conference on Smart Energy Grid Engineering*, Oshawa, Canada, 2021.

[10] J. C. do Prado and U. Chikezie, "A decision model for an electricity retailer with energy storage and virtual bidding under daily and hourly CVaR assessment," *IEEE Access*, in press, DOI 10.1109/ACCESS.2021.3100815.

Table of Contents

List of Figures

List of Tables

1. Introduction

1.1 Background

This project is motivated by the growing integration of utility-scale and distributed energy storage resources in both transmission and distribution systems. As US Federal Energy Regulatory Commission (FERC) Orders No. 841 and No. 2222 request all the US system operators to completely open their energy and ancillary services markets to both utility-scale and retail-scale (distributed) energy storage resources, these energy storage resources bring in the following challenges to the wholesale market operation and participation.

- It is observed by several independent system operators that the utility-scale energy storage resources are very active for regulation service provision, despite they are also capable of providing many other services (such as energy, reserve, peak shaving, demand-side management, congestion management, etc.). To incentivize utility-scale energy storage for providing multiple services in a more balanced way, it is important to comprehensively model and analyze the market participation activities of strategic energy storage resources, considering regulation market participation and operation details as well as the impact of battery degradation on their regulation market activities.
- To improve the market revenue for profit-seeking utility-scale energy storage resources and distributed energy storage aggregators, it is important for these market participants to accurately forecast day-ahead and real-time locational marginal prices across the system, in order to determine advanced profit-seeking bidding strategies.
- As the massive integration of distributed energy storage and other distributed resources significantly increases the computational burden for the wholesale market clearing process (the unit commitment and economic dispatch) and endangers the distribution system operation (due to aggregator control actions not monitored by the distribution utilities and distribution grid models not observed by the wholesale market operators), it is important to design a distribution system operator (DSO) framework which optimally coordinates with the wholesale market clearing process as well as operates the retail markets with various distributed re- sources aggregators, considering operating constraints in three-phase unbalanced distribution grids.

This project aims at solving the above challenges in the following aspects.

- A comprehensive modeling framework is proposed to study various market participation activities of utility-scale battery energy storage resources in the energy and ancillary services markets, with detailed consideration of batteries' regulation market activities and degradation cost.
- A decision model for an electricity retailer with utility-scale BESS and virtual bidding is proposed through a two-stage stochastic optimization framework to determine its optimal participation in the wholesale electricity market considering different types of uncertainties.

- Built upon generative adversarial networks and convolutional long short-term memory networks, data-driven price forecasting approaches are proposed to forecast system-wide day-ahead and real-time locational marginal prices with improved forecasting accuracy.
- A DSO framework is proposed to optimally coordinate the aggregators of various distributed resources for their wholesale market participation while operating the retail market, considering three-phase unbalanced distribution system operating constraints, as well as coordinated market clearing mechanisms between the wholesale and retail markets.

1.2 Project Outcomes

The project outcomes and major contributions are summarized below for each chapter of this report.

1.2.1 Optimal Participation of Price-maker Battery Energy Storage Systems (BESSs) in Energy and Ancillary Services Markets Considering Degradation Cost

A comprehensive framework is proposed in Chapter 2 for studying price-maker BESSs' strategic behavior in correlated energy, reserve, and regulation markets, with a special focus on investigating BESSs' excessive regulation service provision. Built upon existing bi-level optimization models for studying price-maker BESS's strategic behavior in energy/ancillary services markets [2–11], this work further makes the following contributions.

- A realistic degradation cost model based on rainflow algorithm is deployed in the bi-level optimization framework to investigate BESS degradation cost variations when providing energy, reserve, and regulation services.
- To study impacts of BESS's AGC (automatic generation control) signal following activities on its revenue, degradation, and operating patterns, an AGC signal dispatch model is proposed to deploy AGC signals in the bi-level framework based on market outcomes. This modeling effort enhances the regulation market clearing model and enables detailed investigations on BESSs' excessive regulation service provision.
- BESS's operating characteristics across energy/ancillary services markets, BESS's regulation market participation strategies, the impact of BESS's profit maximization on wholesale market operations, and the impacts of BESS capacity, replacement cost and variations in load and reliability requirements of the grid on the BESS operation and revenue are analyzed thoroughly with this detailed modeling framework on a synthetic test case with real-world data for market parameters and BESS parameters.

Built upon this comprehensive modeling framework, case studies on a synthetic system with real-world data are performed to investigate BESS operating characteristics in the energy, reserve, and regulation markets. Key insights out of the case studies are summarized below.

Despite the profit-seeking (price-making) characteristics of utility-scale BESSs, their wholesale market participation still reduces the system total operation cost.

- BESSs tend to participate the least in the energy market which induces high degradation costs and deep charge/discharge cycles.
- BESSs contribute the most to the regulation market which induces low degradation costs and shallow charge/discharge cycles for following the AGC signals.
- The regulation revenue of BESSs tends to depend more on its charge/discharge limit, while the energy and reserve revenue of BESSs tends to depend more on its capacity.
- The regulation revenue of BESSs tends to experience more variations over different seasons/months of the year, compared to the energy and reserve revenue of BESSs. The regulation revenue variations are mainly affected by seasonal/monthly variations of system regulation requirements.

1.2.2 Impact of Battery Degradation on Market Participation of Utility-scale BESSs

Built upon our framework in Chapter 2, this chapter performs comparative case studies to investigate the impact of battery degradation on the operation scheduling and revenue/cost of a price-maker BESS in real-time energy, reserve, and pay as performance regulation markets. By including and removing the battery degradation cost model and detailed AGC signal dispatch model in the framework proposed in Chapter 2, we could determine the optimal scheduling of a price-maker BESS is real-time energy and ancillary services markets with and without considering the battery degradation cost in the decision-making process. Simulation results obtained using this framework with and without these two models (the degradation model and AGC signal dispatch model) on a synthetic test system are presented in four different cases, representing various market participation policies for the BESS. Case study results show that 1) considering degradation cost may significantly reduce BESS's energy market participation; 2) the BESS's participation pattern in the reserve and regulation markets is not significantly impacted by the battery degradation cost.

1.2.3 Integrating BESSs in the Electricity Market: Conceptual Framework and Case Study

In this chapter, a conceptual framework for the integration of BESSs in the wholesale and retail electricity markets is presented and discussed. In addition, a stochastic decision-making model for an electricity retailer with BESS and virtual bidding is proposed and validated through case studies. In this chapter, we make the following contributions:

- The proposed market framework illustrates how BESSs are integrated into the grid and how they are able to interconnect with other BESS owners locally and share resources such as peer-to-peer energy trading.
- A two-stage stochastic optimization model to determine the short-term decisions of an electricity retailer with self-production of renewable energy, BESS, and virtual bidding is proposed. The proposed model minimizes the retailer's expected procurement cost and determines the optimal bidding curves to be submitted in the wholesale electricity market. Different from previous approaches, the proposed model integrates both BESS and virtual bidding in the retailer's short-term decisions.

1.2.4 Predicting Real-Time Locational Marginal Prices (LMPs): A GAN-Based Approach

This chapter proposes a purely data-driven approach for predicting system-wide real-time locational marginal prices (RTLMPs) and day-ahead locational marginal prices (DALMPs) by learning spatio-temporal correlations among heterogeneous public market data, without requiring any confidential information on system topology, model parameters, or market operating details. In this chapter, we make the following contributions:

- We introduce a general data structure which enables efficient storage and organization of spatio-temporally correlated system-wide heterogeneous market data streams (i.e., LMPs, loads, generation offers, generation mix data, etc.) into the format of 3-dimensional (3D) tensors. This general data structure can be integrated into various LMP predictors to better capture spatio-temporal correlations among system-wide demands, supplies, and LMPs.
- We formulate the RTLMP prediction problem as a 2-dimensional (2D) array prediction problem. A conditional generative adversarial network (GAN) based prediction model is trained with multiple loss functions to learn the spatio-temporal correlations among historical market data. The discriminator model and adversarial training procedure are taken to eliminate blurry predictions. This model is applied to predict hourly system-wide RTLMPs, using only public market data. To our best knowledge, this is the first attempt toward applying conditional GANs for power system spatio-temporal data forecasts, rather than simply for synthetic power system data generations [12, 13].
- An auto-regressive moving average (ARMA) based online calibration method is proposed to solve the prediction deviations caused by generation bidding uncertainties without frequent updates to the GAN-based prediction model. To our best knowledge, this is the first study incorporating generation bidding uncertainties to the prediction and analysis of energy market data.
- The proposed LMP prediction approach is generalizable toward various types of price forecasting problems. Case studies on real-world market data verify the prediction accuracy of this approach for RTLMP and DALMP forecasts in both day-ahead and hour-ahead manner, when only annual GAN model update is required.

Although the proposed approach is applied to system-wide LMP prediction, the prediction method and the 3D tensor data structure can be generalized to system-wide load and renewable generation prediction problems. The LMP prediction problem is more challenging than the other two problems, as uncertainties from both loads and generations could reduce prediction accuracy [14, 15]. The system-wide LMP predictor (which is a general predictor for LMPs at multiple locations) can also be easily adjusted to predict LMPs at several nodes over certain sub-areas in a system. This enhances the LMP prediction for generator owners and load serving entities who buy/sell energy at these nodes/sub-areas, as well as market participants in the purely financial instruments of electricity market (such as financial transmission rights) who cares about the spatial LMP differences among different nodes.

1.2.5 Locational Marginal Price Forecasting using Convolutional Long Short-Term Memory- Based Generative Adversarial Network

This chapter proposes a convolutional LSTM (CLSTM) based generative adversarial network (GAN) to forecast system-wide LMPs from market participants' perspective, without power grid models and generator bidding details. The LMP forecasting problem is formulated as a sequence-to-sequence forecasting problem, and the LMP spatio-temporal correlations are learned by the CLSTM network during adversarial training. The proposed approach is trained to forecast most likely future LMP sequences, which maximize the conditional probability given by historical LMPs. Although the proposed CLSTM based GAN model is applied to forecast system-wide LMPs, this model offers a general neural network structure which can be utilized for other spatio-temporal forecasting problems in power systems, such as system-wide demand and wind/solar generation forecasting. In general, the LMP forecasting problem is more challenging than other power system forecasting problems (such as demand forecasting), since LMPs are highly volatile with price spikes. When conventional forecasting techniques are applied to LMP and demand forecasting problems, the typical forecasting errors could reach beyond 20% for LMP forecasting but around 2% for demand forecasting [16].

1.2.6 Retail Market Design and Operation for Distributed Energy Storage and Other Distributed Resources

This chapter integrates single-phase aggregators for distributed energy storage and other distributed energy resources (DERs) for wholesale and retail markets participation considering a market settlement procedure. This study addresses the above questions with the following major contributions:

- A distribution system operator (DSO) framework is proposed to optimally coordinate various DER aggregators, including the demand response aggregators (DRAGs), renewable energy aggregators (REAGs), energy storage aggregators (ESAGs), dispatchable distributed generation aggregators (DDGAGs), and electric vehicle charging stations (EVCSs), for the wholesale market participation while operating the retail market.
- A market settlement approach is proposed for the DSO, which coordinates with the wholesale market clearing process and ensures the DSO's non-profit characteristic.
- It is proved that at the wholesale-DSO coupling substation, the total payment received/compensated by the DSO under the wholesale price is identical to that under three single-phase distribution LMPs for each phase at the substation.
- A linearized unbalanced power flow is presented to handle the single-phase market participants while assuring three-phase balanced offers to the wholesale market.
- The DSO's market outcomes and market settlement process are investigated through case studies on small and large distribution test systems.

The proposed DSO reduces the computational burden for wholesale market clearing by moving the DER-related market clearing computations to the DSO level, while satisfying distribution

system operating constraints and being compatible with the current wholesale market structures. Case studies are performed on the 33-node balanced distribution system and the 240-node unbalanced distribution system. The results in the balanced network show that the DSO sells energy to the wholesale market when the wholesale energy price is high. The DSO assigns regulation capacity-down services to the ESAG for increasing its charge level and decreasing DSO's operating cost. The DDGAG is cleared to sell energy during peak hours. There are opportunities for the EVCS to increase its charge level by providing regulation capacity-up. The DRAG purchases energy during off-peak hours. The results in the unbalanced system show that although the DSO's retail market is unbalanced, the DSO's share for participating in the wholesale market is three-phase balanced. The DSO assigns more charging states to the ESAGs with higher energy offering prices. In the unbalanced system, the DSO may buy energy from the DDGAG with higher energy offering price to submit a balanced offer to the ISO (independent system operator). The DSO sells energy to DRAGs and EVCSs considering achieving balanced operating conditions at the DSO-ISO coupling point.

1.3 Report Organization

The report is organized as follows. Chapter 2 presents the bi-level optimization framework for investigating comprehensive market participation activities of utility-scale price-maker battery energy storage systems (BESSs) in the joint energy, reserve, and regulation markets, with detailed considerations of the regulation market's AGC (automatic generation control) signal dispatch process and the battery degradation characteristics. Chapter 3 discusses the impact of battery degradation on market participation activities of utility-scale BESSs. Chapter 4 presents a conceptual framework for the integration of BESSs in the electricity market and proposes a decision-making model for an electricity retailer with BESS and virtual bidding through a two-stage stochastic optimization framework. Chapter 5 presents a data-driven (model-free) approach for predicting system- wide real-time and day-ahead locational marginal prices (LMPs) based on generative adversarial networks (GAN). This approach can be utilized by various market participants, including the utility-scale BESS owners and distributed energy storage aggregators, for predicting day-ahead and real-time LMPs to improve their market participation strategies. Chapter 6 presents an enhanced system-wide LMP prediction approach, which is built upon the GAN-based approach in Chapter 5. This enhanced prediction approach takes advantage of the convolutional long short-term memory (LSTM) network which is designed for capturing spatio-temporal correlations among system- wide time series data. Chapter 7 proposes a retail market design and operation framework for handling market activities of distributed energy storage aggregators and other distributed resources aggregators. Chapter 8 provides concluding remarks to this report.

2. Optimal Participation of Price-maker Battery Energy Storage Systems in Energy and Ancillary Services Markets Considering Degradation Cost

Nomenclature

Abbreviations

B	Set of battery storage buses, indexed by i.
G	Set of generator buses, indexed by j.
K	Set of battery degradation cost curve segments, indexed by k.
L	Set of transmission lines, indexed by (n, w).
N	Set of all buses, indexed by n and w.
T	Set of market clearing intervals, indexed by t, t^*.
Z	Set of AGC signal sub-invervals, indexed by z.
B	Superscript for battery energy storage units.
Ch, Dis	Superscript for charge and discharge power of each degradation segment.
E	Superscript for the energy market.
G	Superscript for generators.
RgC	Superscript for the regulation capacity market.
RgM	Superscript for the regulation mileage market.
Rs	Superscript for the reserve market.
$TCh, TDis$	Superscript for total charge and discharge power in each sub-interval.

Terminology Definitions

α	Generator price offer.
$\bar{t}, \bar{z}$	The last interval and the last sub-interval.
$\Delta t, \Delta z$	Interval and sub-interval time spans.
η	Battery unit's charge/discharge efficiency.
AGC	Automatic generation control signal set points.
C^{Deg}	Slope of each degradation cost segment.
e^{Max}	Each degradation cost segment's capacity limit.
H	Transmission line susceptance.
m	Regulation mileage multiplier.
P^{Load}	System real power load.
P^{Min}, P^{Max}	Generator output power limit.
P^{Rate}	Battery unit's charge/discharge limit.
$P^{Rg,Ramp}$	Ramp limit for generator regulation provision.

$P^{Rs,Ramp}$	Ramp limit for generator reserve provision.
R	System requirements for ancillary services.
SOC^{Init}	Battery unit's initial state of charge.
SOC^{Max}	Battery unit's maximum state of charge.
SOC^{Min}	Battery unit's minimum state of charge.
TL	Transmission line thermal limit.

Symbols

β	Price offer of battery units.
π	Market clearing prices.
θ	Bus voltage angles.
e	Energy stored during each degradation segment.
P	Real power.
PF	Regulation market participation factor.
Q	Quantity offer of battery units.
v	Sub-interval charge/discharge indicator.

2.1 Introduction

Motivated by US Federal Energy Regulatory Commission Order 841 [17] requiring independent system operators (ISOs) to open energy and ancillary services markets for BESSs, many profit-seeking BESSs joined wholesale markets. From BESS market activities, several ISOs observe BESSs are very active in regulation markets, despite energy and reserve markets are also open [18, 19]. In extreme cases, BESSs' regulation service almost covers system-wide regulation service requirements and saturates regulation markets [20]. As BESSs can provide other services (energy, reserve, peak shaving, demand-side management, congestion management, etc. [21]) which, compared to regulation service, could be more important for stable/economic grid operations in some cases, it is desired to incentivize BESSs to provide multiple services in a more balanced way without concentrating exclusively on regulation service. This calls for efforts to explore mechanisms behind profit-seeking BESSs' excessive regulation market activities despite all energy/ancillary services markets are open.

Existing literature for BESS market participation falls into two categories. The first category [22–29] models the BESS as a price-taker. These works do not model impacts of BESSs' strategic behavior on market clearing results, therefore cannot obtain thorough understanding for market activities of profit-seeking large-scale BESSs. The second category [2–10] studies BESSs' strategic behavior by the price-maker BESS model, which is a bi-level optimization with interactions between BESSs' optimal bidding and ISO's wholesale market clearing. However, most works [2, 3, 5–8, 10] overlook the regulation market and only model BESSs in the energy market [2, 3, 6, 7, 10] or energy and reserve markets [5, 8]. Since BESSs are very active in regulation markets [18, 19], these works ignore the BESSs' major revenue stream (the regulation

market) and cannot accurately evaluate BESSs' strategic behavior and revenue streams in all three markets. Models in [5–10] do not properly consider impacts of BESS degradation on their market activities, by either neglecting the degradation cost [7,10] or modeling it by a linear function and/or cycling limitation model [5,6,8,9] which represents BESS degradation in a less accurate way. Since BESSs have different degradation characteristics when providing different grid services (especially regulation services which requires less BESS cycling depth compared to other services), accurately modeling degradation costs could improve the understanding for BESSs' excessive regulation market participation. Models in [4, 9] consider strategic BESSs in regulation markets (BESSs' major revenue stream). In [4, 9], AGC signals deployment is not considered in the regulation market models and regulation mileage deployment is modeled with predetermined factors. This modeling approach is not an accurate representation of the real-world regulation market structure. Besides, Reference [9] replaces the lower-level market clearing process in the bi-level optimization by predicting a 'price quota curve' [2]. This price quota curve determines how the market clearing price (MCP) changes depending on the quantity offer of a strategic participant. Compared to the full bi-level model with the clearing process of energy/ancillary services markets, this price quota curve may not capture impacts of BESS's provision of one service (regulation) on the price of another service (reserve). Therefore, it cannot capture correlations between BESSs' strategic activities in different markets.

To improve current market designs and incentivize BESSs toward providing multiple grid services in a more balanced and effective manner, a comprehensive modeling framework is needed to investigate the BESS's excessive regulation service provision despite all the energy, reserve, and regulation markets are available to BESSs. Several gaps remain between the existing literature and this desired framework. 1) The regulation market clearing details, such as the deployment of automatic generation control (AGC) signals, and the interactions between the regulation market and energy/reserve markets need to be modeled properly to capture BESS market activities; 2) The variations of BESS degradation costs when participating in different markets need to be explicitly considered; 3) The BESS's expected long-term market revenue, considering seasonal load variations, need to be investigated.

To resolve these gaps, this chapter proposes a comprehensive framework for studying price-maker BESSs' strategic behavior in correlated energy, reserve, and regulation markets, with a special focus on investigating BESSs' excessive regulation service provision. This model is developed upon our previous work [11] with a simplified model (without BESS degradation cost and AGC signal dispatch model). Built upon existing bi-level optimization models for studying price-maker BESS's strategic behavior in energy/ancillary services markets [2–11], this chapter further makes the following contributions.

- A realistic degradation cost model based on rainflow algorithm is deployed in the bi-level optimization framework to investigate BESS degradation cost variations when providing energy, reserve, and regulation services.
- To study impacts of BESS's AGC signal following activities on its revenue, degradation, and operating patterns, an AGC signal dispatch model is proposed to deploy AGC signals in the bi-level framework based on market outcomes. This modeling effort enhances the regulation market clearing model and enables detailed investigations on BESSs' excessive regulation service provision.

- BESS's operating characteristics across energy/ancillary services markets, BESS's regulation market participation strategies, the impact of BESS's profit maximization on wholesale market operations, and the impacts of BESS capacity, replacement cost and variations in load and reliability requirements of the grid on the BESS operation and revenue are analyzed thoroughly with this detailed modeling framework on a synthetic test case with real-world data for market parameters and BESS parameters.

2.2 Formulation and Methodology

This section formulates the bi-level framework for investigating the interactions between a strategic price-maker BESS's profit maximization and ISO's joint energy, reserve, and regulation markets clearing, considering 1) the degradation cost model deployed into the bi-level framework; 2) the detailed regulation market clearing process with the proposed AGC signal dispatch model. This framework contains the coupled upper-level problem (ULP) and lower-level problem (LLP). The ULP maximizes BESS's total profit across various markets. The LLP simulates ISO's joint market clearing process. Decision variables of the ULP, including BESS's quantity and price offers, serve as the input parameters for the LLP. The MCPs and BESS's scheduled power, determined by the LLP, serve as input parameters for the ULP. This bi-level problem is non-convex and is converted to a single-level mixed-integer linear programming (MILP) problem following the procedure in [30]. This MILP can be solved by commercial solvers.

2.2.1 The Upper-level Problem (ULP) Formulation

In the ULP shown below, the BESS owner with several battery units at different buses maximizes its revenue from real-time energy, reserve, and regulation markets while considering its operating limits and degradation cost.

$$\text{Max} \sum_{t\in\mathcal{T}} \sum_{i\in\mathcal{B}} \{ [\pi_{i,t}^{E} P_{i,t}^{B,E} + \pi_{t}^{Rs} P_{i,t}^{B,Rs} + \pi_{t}^{RgC} P_{i,t}^{B,RgC} + \pi_{t}^{RgM} P_{i,t}^{B,RgM}]\Delta t - \sum_{z\in\mathcal{Z}} \sum_{k\in\mathcal{K}} C_{i,k}^{Deg} P_{i,t,z,k}^{Dis} \Delta z \} \quad \text{(U1)}$$

Subject to:

$$0 \le Q_{i,t}^{SE} \le u_{i,t} P_i^{Rate} \qquad \forall i \in B, \forall t \in T \text{ (U2)}$$

$$0 \le Q_{i,t}^{DE} \le (1 - u_{i,t}) P_i^{Rate} \qquad \forall i \in B, \forall t \in T \text{ (U3)}$$

$$\beta_{i,t}^{E} \ge (1 - u_{i,t}) M \qquad \forall i \in B, \forall t \in T \text{ (U4)}$$

$$0 \le Q_{i,t}^{Rs} \le P_i^{Rate} \qquad \forall i \in B, \forall t \in T \text{ (U5)}$$

$$0 \le Q_{i,t}^{RgC} \le P_i^{Rate} \qquad \forall i \in B, \forall t \in T \text{ (U6)}$$

$$-P_i^{Rate} + P_{i,t}^{B,RgC} \le P_{i,t}^{B,E} \le P_i^{Rate} - P_{i,t}^{B,RgC} - P_{i,t}^{B,Rs} \qquad \forall i \in B, \forall t \in T \text{ (U7)}$$

$$PF_{i,t} = \frac{P_{i,t}^{B,RgM}}{R_t^{RgM}} \qquad \forall i \in B, \forall t \in T \text{ (U8)}$$

$$\sum_{i \in \mathcal{B}} PF_{i,t} \leq 1 \qquad \forall t \in T \text{ (U9)}$$

$$R_t^{RgM} = \sum_z |\, AGC_{t,z} - AGC_{t,z-1}| \qquad \forall i \in B, \forall z \in Z \text{ (U10)}$$

$$P_{i,t}^{B,E} + PF_{i,t} AGC_{t,z} = P_{i,t,z}^{TDis} - P_{i,t,z}^{TCh} \qquad \forall i \in B, \forall t \in T, \forall z \in Z \text{ (U11)}$$

$$0 \leq P_{i,t,z}^{TDis} \leq v_{i,t,z} P_i^{Rate} \qquad \forall i \in B, \forall t \in T, \forall z \in Z \text{ (U12)}$$

$$0 \leq P_{i,t,z}^{TCh} \leq (1 - v_{i,t,z}) P_i^{Rate} \qquad \forall i \in B, \forall t \in T, \forall z \in Z \text{ (U13)}$$

$$P_{i,t,z}^{TDis} (\frac{1}{\eta_i}) = \sum_{k \in \mathcal{K}} P_{i,t,z,k}^{Dis} \qquad \forall i \in B, \forall t \in T, \forall z \in Z \text{ (U14)}$$

$$P_{i,t,z}^{TCh} \eta_i = \sum_{k \in \mathcal{K}} P_{i,t,z,k}^{Ch} \qquad \forall i \in B, \forall t \in T, \forall z \in Z \text{ (U15)}$$

$$P_{i,t,z,k}^{Ch}, P_{i,t,z,k}^{Dis} \geq 0 \qquad \forall i \in B, \forall t \in T, \forall z \in Z, \forall k \in K \text{ (U16)}$$

$$e_{i,t,z,k} - e_{i,t,z-1,k} = (P_{i,t,z,k}^{Ch} - P_{i,t,z,k}^{Dis}) \Delta z \qquad \forall i \in B, \forall t \in T, \forall z \neq 1 \in Z, \forall k \in K \text{ (U17)}$$

$$e_{i,t,z,k} - e_{i,t-1,\bar{z},k} = (P_{i,t,z,k}^{Ch} - P_{i,t,z,k}^{Dis}) \Delta z \qquad \forall i \in B, \forall t \in T, \tau = 1, \forall k \in K \text{ (U18)}$$

$$0 \leq e_{i,t,z,k} \leq e_{i,k}^{Max} \qquad \forall i \in B, \forall t \in T, \forall z \in Z, \forall k \in K \text{ (U19)}$$

$$SOC_{i,t,z} = \sum_{k \in \mathcal{K}} e_{i,t,z,k} \qquad \forall i \in B, \forall t \in T, \forall z \in Z \text{ (U20)}$$

$$SOC_i^{Min} + (P_{i,t}^{B,Rs} \Delta z) \leq SOC_{i,t,z} \leq SOC_i^{Max} \qquad \forall i \in B, \forall t \in T, \forall z \in Z \text{ (U21)}$$

$$SOC_{i,t,z} - \sum_{t^*=0}^{t^*=t-1} P_{i,t^*}^{B,Rs} \Delta t - P_{i,t}^{B,Rs} z \Delta z \geq SOC^{Min} \qquad \forall i \in B, \forall t \in T, \forall z \in Z \text{ (U22)}$$

$$SOC_{i,t,z} = SOC_i^{Init} \qquad \forall i \in B, t = 0 \,\&\, z = \bar{z}, t = \bar{t} \,\&\, z = \bar{z} \text{ (U23)}$$

$$u_{i,t}, v_{i,t,z} \in \{0,1\} \qquad \forall i \in B, \forall t \in T, \forall z \in Z \text{ (U24)}$$

The objective function (U1) maximizes total revenue of a BESS owner (with multiple battery units at different buses). It considers the BESS's net revenue from the energy, reserve, regulation capacity and regulation mileage markets, as well as the BESS's degradation cost. While calculating the BESS's regulation capacity and mileage revenue, the BESS's performance score in following AGC signals is assumed to be 1, indicating the BESS's perfect AGC signals tracking accuracy due to its fast response capability. Decision variables of the ULP include each battery unit's price and quantity offers for real-time energy, spinning reserve capacity, regulation capacity, and regulation

mileage provisions. These offers serve as inputs for ISO's joint market clearing process in the LLP.

2.2.1.1 Constraints for AGC Signal Dispatch Modeling

In existing works, regulation mileage deployment (AGC dispatch) is usually modeled on the battery's state of charge (SOC) at the end of each market clearing interval (5 or 15 minutes) using predetermined factors of unit's regulation mileage participation $P_{i,t}^{RgM}$ [4, 9, 11]. However, modeling SOC with this resolution (5 or 15 minutes) cannot capture SOC changes resulted from following AGC signals, since AGC signals are usually sent out every 4 seconds. It is important to monitor SOC changes resulted from following AGC signals to understand the effect of AGC following activities on BESS's degradation costs and operation. To accurately represent BESS's AGC signal following activities, the unit-level AGC signal dispatched to each battery needs to be properly modeled. Using (U8)-(U10), a participation factor (PF) is defined to simulate the AGC signal dispatch process and obtain the unit-level AGC signal for every battery. The proposed PF and the AGC signal dispatch simulation enable us to perform detailed studies on the impact of BESS's AGC signal following activities on its SOC management and battery degradation cost.

In (U8), the PF is defined as the ratio of each battery's scheduled regulation mileage provision to system regulation mileage requirement. The summation of PFs for all batteries should not go beyond 1 (i.e., 100% of the system regulation mileage requirement), as described in (U9). In (U10), the system regulation mileage requirement for a market clearing interval is defined by accumulating differences between two system-level AGC signal setpoints obtained at adjacent AGC sub-intervals.

As mentioned, AGC signals are forecasted parameters of the optimization. Similar to the AGC dispatch method of [31], the concern of using PF for dispatching AGC signals is that the amount of dispatched AGC to each regulation unit does not exceed the unit's scheduled regulation capacity. This work addresses the issue by scaling the mileage multiplier *m* of the LLP. These PFs are then used to calculate regulation mileage payments to various batteries (i.e., the BESS's revenue for regulation mileage provision). PFs are also used for calculating the charged/discharged power of each unit in each sub-interval by Constraint (U11).

2.2.1.2 Constraints for Degradation Cost Modeling

The battery degradation cost is typically calculated based on the rainflow algorithm, which counts the number of charge/discharge cycles, determines the cycle depth, and obtains accurate degradation cost based on the cycle count and cycle depth. However, this algorithm does not have an analytical expression and cannot be integrated directly in an optimization problem [27]. This work deploys a linear approximation of the rainflow algorithm into the bi-level optimization framework. For degradation cost approximation, the battery capacity (from 0% to 100%) is uniformly divided into several segments (i.e., the degradation segments) represented by the K set. The energy capacity limit of each segment e^{Max} is a portion of the battery capacity. A piecewise linear approximation of the degradation cost (obtained from the battery cycle depth aging function) is assigned to each segment C^{Deg}. This work calculates the degradation cost in each AGC signal sub-interval. Therefore, the degradation cost caused by following AGC signal and/or energy

market participation is considered. Details on battery capacity segmentation, C^{Deg} calculation, and accuracy of the approximation are in [27]. In (U1), this degradation cost is subtracted from the BESS revenue.

During a certain AGC signal sub-interval, Constraints (U11)-(U13) specify how much the battery unit is charging or discharging by determining the sign of the value obtained by summation of battery unit's scheduled power in the energy market and the AGC signal dispatched to the battery unit. Hence, in each sub-interval, the battery unit may provide regulation up or down services while it sells or buys power in the energy market. The accumulation of these energy and regulation provisions determines the amount of power it is charging or discharging. For example, if in an interval, the battery unit buys 3 MW from energy market ($P_{i,t}^{B,E} = 3$) and receives 2 MW of AGC signal dispatch in one of the sub-intervals for regulation up service ($PF_{i,t}AGC_{t,z} = 2$), then the left hand side of (U11) will be 1 resulting in $P_{i,t,z}^{T,Ch} = 1$, which means that battery unit is charging for 1 MW during that sub-interval. Constraints (U14)-(U16) assign battery charge/discharge power during each AGC signal sub-interval to the corresponding degradation segments, while battery charge/discharge efficiency is considered. Constraints (U17)-(U18) evaluate battery stored energy in each degradation segment, by comparing difference between the stored energy in two consecutive AGC signal sub-intervals. Constraint (U17) performs this comparison for consecutive sub-intervals within the same market clearing interval, while Constraint (U18) performs this comparison between the first sub-interval of each market clearing interval and the last sub-interval of the previous market clearing interval. Constraint (U19) enforces the energy capacity limits of the degradation segments.

The above degradation cost representation (in (U1) and (U11)-(U19)) indicates in each AGC signal sub-interval, 1) if the battery unit is charging, the charged energy is allocated to the degradation segment with the lowest degradation cost which has not yet reached its maximum energy limit; 2) if the battery unit is discharging, the discharged energy is subtracted from the degradation segment with the lowest degradation cost which has been charged previously.

2.2.1.3 Constraints for Battery SOC Management

Constraint (U20) calculates the battery SOC during every AGC sub-interval by accumulating the stored energy in all segments of battery capacity. The energy in each segment is calculated through (U11)-(U19) based on the charged/discharged power resulted from following AGC signals and charged/discharged power in the energy market. Constraint (U21) limits the SOC value by the unit's maximum and minimum SOCs. In (U21), enough battery capacity is reserved for spinning reserve provision. Although spinning reserve deployment is not modeled, Constraint (U22) ensures that enough energy is stored in the battery to maintain reserve provision in the worst-case scenario for scheduled reserve deployment in all intervals. It guarantees the reliable operation of the system [32]. Constraint (U23) ensures the SOCs at the beginning and end of the simulation horizon remain at the same pre-specified value, so it is possible to expand a short-time simulation result to a longer period. Constraint (U24) defines binary variables for the battery's charging/discharging states during different sub-intervals $v_{i,t,z}$ and binary variables for the battery's supply/demand states during different market clearing intervals $u_{i,t}$.

2.2.1.4 Constraints for Battery Charge/Discharge Limits

Constraints (U2)-(U3) limit unit i of BESS to either sell ($u_{i,t} = 1$) or buy energy ($u_{i,t} = 0$) in the energy market, while its quantity offer is limited by the unit's charge/discharge rate. If it buys energy, Constraint (U4) ensures the battery's energy price offer $\beta_{i,t}^{E}$ is large enough such that the battery behaves as a self-scheduling unit like other loads in the system. Constraints (U5)-(U6) limit the battery's quantity offers for spinning reserve and regulation capacity provisions within the unit's charge/discharge rate, respectively. Constraint (U7) indicates the battery's total power scheduled for energy, reserve capacity, and regulation capacity provisions must stay below the unit's charge/discharge rate. Note that regulation capacity provision is symmetrical and represents both regulation up and down.

2.2.2 The Lower-level Problem (LLP) Formulation

The LLP below models ISO's joint market-clearing process for real-time energy, spinning reserve, and pay-as-performance regulation markets (with regulation capacity and mileage payments). It is possible to implement any choice of market clearing interval and AGC dispatch sub-interval with this model. The LLP is built upon the market structure of California ISO. The market structure details can be found in [11, 33].

$$\text{Min} \sum_{t\in\mathcal{T}}[\sum_{j\in\mathcal{G}}(\alpha_{j,t}^{E}P_{j,t}^{G,S} + \alpha_{j,t}^{Rs}P_{j,t}^{G,Rs} + \alpha_{j,t}^{RgC}P_{j,t}^{G,RgC} + \alpha_{j,t}^{RgM}P_{j,t}^{G,RgM}) + \sum_{i\in\mathcal{B}}(\beta_{i,t}^{E}P_{i,t}^{B,E} + \beta_{i,t}^{Rs}P_{i,t}^{B,Rs} + \beta_{i,t}^{RgC}P_{i,t}^{B,RgC} + \beta_{i,t}^{RgM}P_{i,t}^{B,RgM})]\Delta t \quad \text{(L1)}$$

Subject to:

$$P_{j}^{Min} + P_{j,t}^{G,RgC} \le P_{j,t}^{G,S} \le P_{j}^{Max} - P_{j,t}^{G,Rs} - P_{j,t}^{G,RgC} \quad \forall j \in G \text{ (L2)}$$

$$0 \le P_{j,t}^{G,Rs} \le P^{Rs,ramp} \quad \forall j \in G \text{ (L3)}$$

$$0 \le P_{j,t}^{G,RgC} \le P^{Rg,ramp} \quad \forall j \in G \text{ (L4)}$$

$$P_{j,t}^{G,RgC} \le P_{j,t}^{G,RgM} \le m_{j,t}P_{j,t}^{G,RgC} \quad \forall j \in G \text{ (L5)}$$

$$-Q_{i,t}^{DE} \le P_{i,t}^{B,E} \le Q_{i,t}^{SE} \quad \forall i \in B \text{ (L6)}$$

$$0 \le P_{i,t}^{B,Rs} \le Q_{i,t}^{Rs} \quad \forall i \in B \text{ (L7)}$$

$$0 \le P_{i,t}^{B,RgC} \le Q_{i,t}^{RgC} \quad \forall i \in B \text{ (L8)}$$

$$P_{i,t}^{B,RgC} \le P_{i,t}^{B,RgM} \le m_{i,t}P_{i,t}^{B,RgC} \quad \forall i \in B \text{ (L9)}$$

$$\sum\nolimits_{j\in\mathcal{G}} P_{j,t}^{G,Rs} + \sum\nolimits_{i\in\mathcal{B}} P_{i,t}^{B,Rs} \ge R_{t}^{Rs} : \pi_{t}^{Rs} \quad \text{(L10)}$$

$$\sum_{j\in\mathcal{G}} P_{j,t}^{G,RgC} + \sum_{i\in\mathcal{B}} P_{i,t}^{B,RgC} \geq R_t^{RgC} : \pi_t^{RgC} \quad \text{(L11)}$$

$$\sum_{j\in\mathcal{G}} P_{j,t}^{G,RgM} + \sum_{i\in\mathcal{B}} P_{i,t}^{B,RgM} \geq R_t^{RgM} : \pi_t^{RgM} \quad \text{(L12)}$$

$$\sum_{j\in\mathcal{G}|j=n} P_{j,t}^{G,S} + \sum_{i\in\mathcal{B}|i=n} P_{i,t}^{B,E} = P_{n,t}^{Load} + \sum_{w\in\mathcal{N}} H_{nw}(\theta_{n,t} - \theta_{w,t}) : \pi_{n,t}^{E} \quad \forall n \in N \text{ (L13)}$$

$$-TL_{nw} \leq H_{nw}\left(\theta_{n,t} - \theta_{w,t}\right) \leq TL_{nw} \quad \forall (n,w) \in L \text{ (L14)}$$

The objective function (L1) determines the system's total operating cost. The decision variables are the scheduled power of each generating/battery unit for energy, reserve, regulation capacity, and regulation mileage provisions. The LLP also determines the energy, reserve, regulation capacity, and regulation mileage prices for each battery unit. The battery's scheduled power and MCPs serve as inputs for the ULP.

2.2.2.1 Constraints for AGC Signal Dispatch Modeling

Constraints (L5) and (L9) apply to each regulation market participant (BESSs and generators) to represent the pay as performance market model. The regulation mileage multiplier *m* is assigned by the ISO to each regulating unit based on its historical performance on regulation mileage provision. These multipliers serve as parameters of the optimization problem.

To ensure the AGC signal dispatched to each regulating unit (based on the participation factor PF) does not go beyond the unit's scheduled power for regulation capacity provision, we propose to uniformly scale the unit's mileage multiplier *m* in a way that (1) always holds. Note that in most market clearing intervals, Equation (1) may hold without scaling.

$$m_{n,t} \leq \frac{R_t^{RgM}}{Max_z(|AGC_{t,z} - AGC_{t,z-1}|)} \quad \forall n \in B \cup G, \forall t \in T \text{ (1)}$$

With (1), in each market clearing interval, the regulation mileage multiplier of each regulating unit is scaled to be less than the ratio of system regulation mileage requirement to the maximum change between consecutive AGC signal setpoints. Consider a system whose regulation capacity and mileage requirements are R_t^{RgC} = 6MW and R_t^{RgM} = 12MW, respectively, in an interval. Assume Units 1, 2, and 3 provide regulation service. They have identical 2MW scheduled regulation capacity ($P_1^{RgC} = P_2^{RgC} = P_3^{RgC} = 2MW$). Based on historical performance, ISO sets their mileage multipliers as m_1 = 5, m_2 = m_3 = 3. Without uniform scaling of mileage multipliers, if Unit 1 has the lowest regulation mileage price bid and the other two units have identical bids, the units' scheduled regulation mileage will be $P_1^{RgM} = 8MW, P_2^{RgM} = P_3^{RgM} = 2MW$. Based on (U8), the units' PFs are $PF_1 = \frac{2}{3}, PF_2 = PF_3 = \frac{1}{6}$. If maximum change between consecutive system-wide AGC signals is 4 MW ($Max_z\left(\left|AGC_{t,z} - AGC_{t,z-1}\right|\right) = 4MW$), Unit 1 should provide $\frac{2}{3}$ of it (2.6 MW), which is greater than the unit's scheduled regulation capacity and is not

acceptable. By uniformly scaling mileage multipliers with a factor of $\frac{3}{5}$, the inequality in (1) is guaranteed, resulting in $m_1 = 3, m_2 = m_3 = 1.8$. Accordingly, the units' scheduled regulation mileage will be $P_1^{RgM} = 6MW, P_2^{RgM} = P_3^{RgM} = 3MW$. Hence, Unit 1 should provide 2MW of the 4MW system-wide AGC signal change, which lies within its scheduled regulation capacity. Note that Unit 1 can increase its share for regulation mileage provision by increasing its share in the regulation capacity market. Therefore, this scaling does not affect the mileage multipliers' role, which is differentiating between units based on their historical performance and ramp rates. The scaling ensures the dispatched AGC signals, based on the scheduled regulation mileage, are proportional to the scheduled regulation capacity of the units.

2.2.2.2 Constraints for Market Participants

Constraints (L2)-(L4) ensure for each generating unit, 1) its total power delivery lies within its maximum and minimum generation limits; 2) its reserve and regulation capacity provisions do not exceed the corresponding ramp rates. Constraints (L6)-(L8) ensure the battery's scheduled power in the energy, reserve, and regulation capacity markets lie within the corresponding quantity offers of the BESS (determined by the ULP).

2.2.2.3 Constraints for Market Operations

Constraints (L10)-(L12) ensure system requirements on reserve, regulation capacity, and regulation mileage services are satisfied. The dual variables of these constraints $\pi_t^{Rs}, \pi_t^{RgC}, \pi_t^{RgM}$ represent the MCPs for the corresponding services. Constraint (L13) represents the nodal power balance. Its dual variable $\pi_{n,t}^{E}$ represents the locational marginal price (LMP) at bus n. The above MCPs and LMPs serve as inputs for the ULP. Constraint (L14) represents the transmission line thermal limits.

2.3 Case Studies

The framework is evaluated on 3rd area of IEEE Reliability Test System of the Grid Modernization Laboratory Consortium (RTS-GMLC) [34], with 25 buses, 39 lines, 26 generators, and a BESS. The simulation horizon is 24 hours. The market clearing interval is 15 minutes. The AGC signal dispatch sub-interval is set at 20 seconds to reduce computational burden. System load profile and reserve/regulation capacity requirements are created using average load of the test case from June to August. System regulation mileage requirement in each market clearing interval is set at around 1.5 times corresponding regulation capacity requirement (a typical requirement in real- world markets [31]). Figure 2.1 shows 24-hour system ancillary services requirements. Sample AGC signals from ISO New England are adopted [35].

We assume generators use generation costs as energy price offers. Generator price offers for reserve, regulation capacity and mileage are created using their energy price offers multiplied by 0.15, 0.4, and 0.07, respectively, where the multipliers are corresponding average ratios in PJM historical data [36].

Parameters of the lithium-ion BESS at Bus 13 are: operation duration = 4 hours, maximum charge/discharge cycle depth = 80%, useful life = 6000 cycles at 80% cycle depth [37], replacement cost = 200k$/MWh [38], P^{Rate} = 50MW, Capacity = 200MWh, SOC^{Min} = 20MWh, SOC^{Max} = 180MWh, SOC^{Init} = 90MWh, η = 95%. Based on lithium-ion BESS's cycle depth aging function [39] and replacement cost, the degradation cost function is $C(\delta) = 52.4\,\delta^{2.03}$, where δ is the ratio of cycle depth to BESS capacity. This near quadratic function is approximated by a 16-segment piecewise linear function for degradation cost modeling.

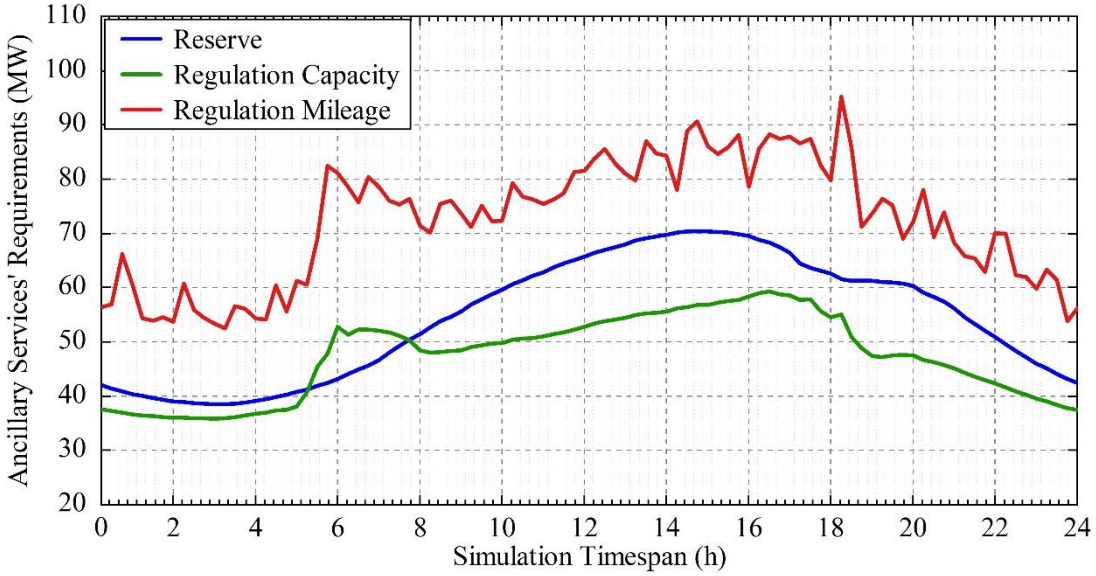

Figure 2.1 The test system's ancillary services requirements.

2.3.1 BESS Degradation Cost and Regulation Market Activities

Figure 2.2 shows 1) BESS total revenue from each market and its degradation cost; 2) system total operation cost for each market, with and without the BESS. It is observed although a price-maker BESS seeks to maximize its profit, its market participation still reduces the system total operation cost and benefits the whole system. Comparing the total operation cost of the regulation capacity market and BESS's revenue from this market, it is clear that BESS is the major contributor to the regulation capacity market. However, with the BESS, the total operation cost of the regulation capacity market still reduces. Figure 2.2 shows almost all the BESS's revenue comes from the regulation capacity and mileage markets, indicating regulation markets being the most profitable for BESS. High share of BESS in regulation market agrees with real-world observations [18–20]. Besides, in Figure 2.2, BESS gains the least revenue from energy market. This is because BESS's energy arbitrage results in deep charge/discharge cycles and increases its degradation cost. This reduces the BESS's revenue from the energy market.

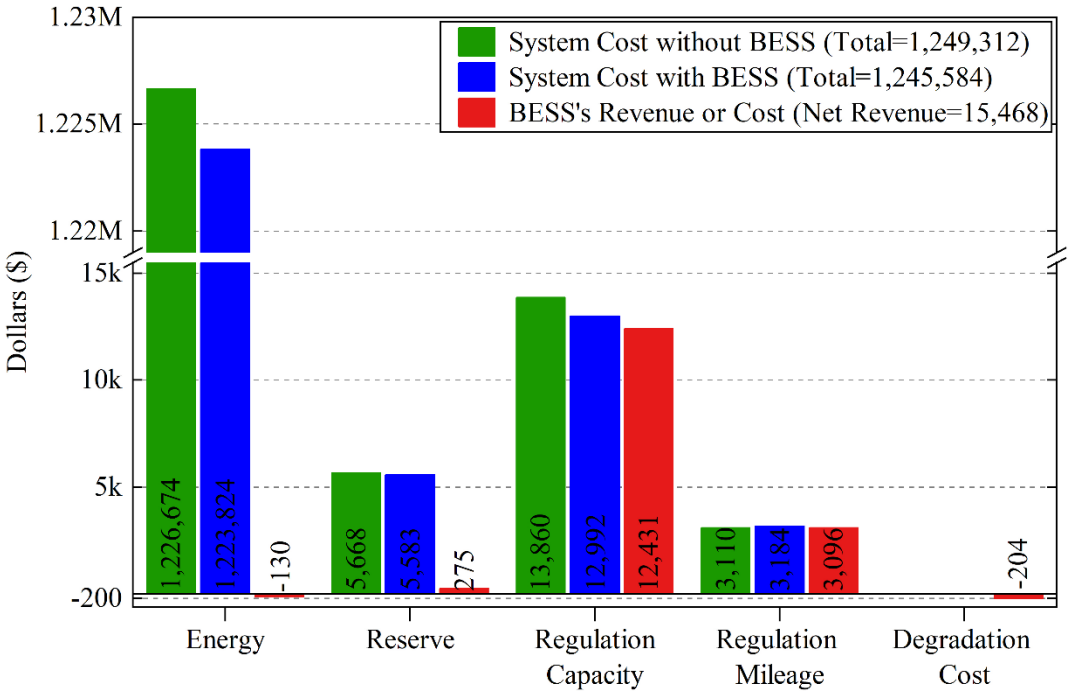

Figure 2.2 System cost with/without BESS and BESS's revenue and costs.

Figure 2.3 shows BESS scheduled power in each market and its 24-hour SOC. When system regulation capacity requirements are less than BESS charge/discharge limit (50MW), system-level regulation requirements are fully satisfied by BESS's regulation service. This indicates, compared to the energy and reserve markets, the regulation market is the primary option for the BESS. During hours 6-8 and 10-18, the system regulation capacity requirements exceed BESS charge/discharge limit, and the BESS could not provide all the required regulation services. In this case, the BESS scheduled power for regulation capacity provision is mostly fixed at the charge/discharge limit, and the system regulation requirements are jointly satisfied by the BESS and other market participants. At the beginning/end of the day when the system regulation capacity requirement falls below the charging/discharging limit, the BESS first provides all the system's regulation requirement, then optimally allocates its unused output capacity across the other markets.

The SOC curve in Figure 2.3 shows the BESS does not experience deep charge/discharge cycles. Extracting the charge/discharge cycles of this SOC curve using exact rainflow algorithm [40] reveals the BESS goes through 207 charge/discharge cycles during the simulation. The cycle depth varies between 1.72MWh and 4kWh, and the average cycle depth is 0.23MWh. These charge/discharge cycles are very shallow (less than 1% of the BESS capacity). These shallow charge/discharge cycles are caused by the BESS's AGC signal following activities. As reducing cycle depths lowers the BESS degradation cost, participating in the regulation market could reduce the BESS's degradation cost while maintaining a certain revenue level. This agrees with Figure 2.2, in which the BESS degradation cost remains low. Additionally, shallow charge/discharge cycles indicate the BESS does not use most of its capacity. Therefore, the BESS revenue depends more on its charge/discharge limit rather than its capacity.

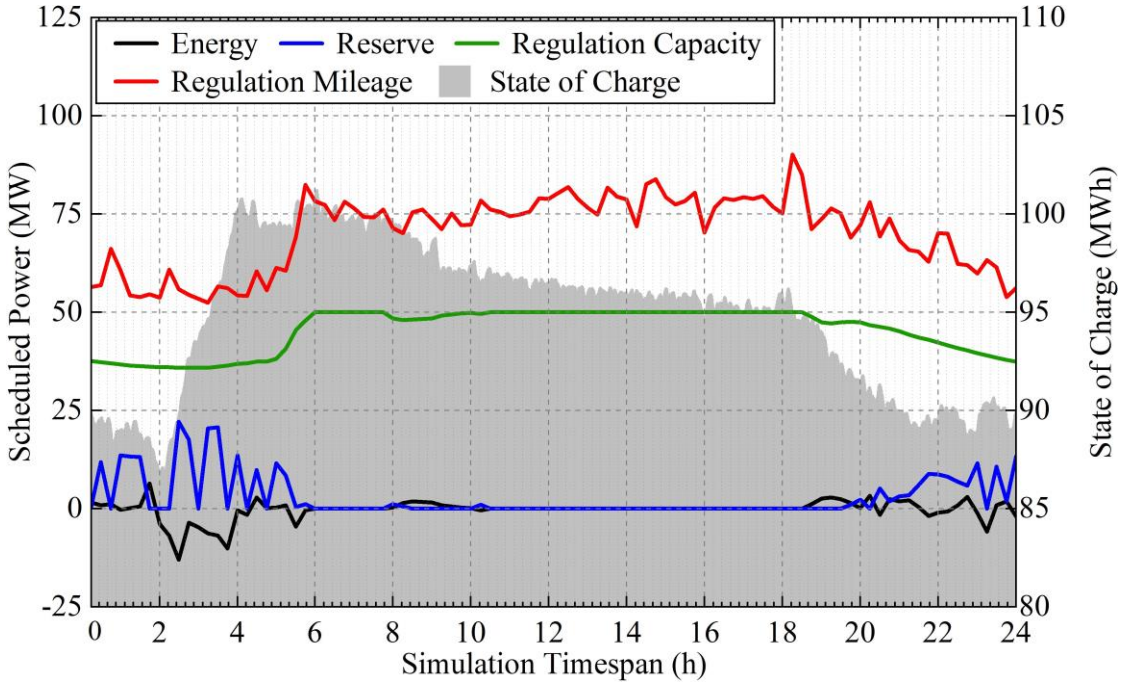

Figure 2.3 Scheduled power of BESS in each market and its state of charge.

2.3.2 Variations of System Load and Reliability Requirements

To study impacts of grid load/ancillary service requirements variations on BESS seasonal operations and long-term revenue, 12 simulations are performed in which 24-hour grid load/ancillary service requirements are the average of the test case load/ancillary service requirements in each month of the year. Across 12 load patterns, the average/maximum/minimum grid load variations in each interval are 360MW, 713MW, and 203MW, respectively, covering wide variations of grid load/ancillary service requirements. Forecasted AGC signals are regenerated to match regulation mileage requirements.

Figure 2.4 shows BESS revenue from each market and its degradation cost in 12 simulations. Over various loads/ancillary service requirements, 1) BESS participates in the regulation market the most and the energy market the least; 2) its regulation market revenue is significantly higher than its reserve market revenue, while its energy market revenue is negative; 3) it participates in energy market mainly for buying energy to compensate its discharged energy. With these simulations built upon averaged system load and ancillary service requirements for each month, the BESS's expected annual revenue (including regulation/reserve market revenue), annual costs (including degradation/energy cost), and annual net operating profit are estimated as $5,909,758, $135,635, and $5,774,123, respectively. The initial battery investment cost is not considered in the estimated net operating profit.

In Figure 2.4, BESS regulation market revenue varies the most compared to its revenue from other markets, since BESS is a major contributor to regulation market. Its regulation market revenue is more affected by system regulation requirement variations. BESS energy/reserve market revenue is less affected by system load/reserve requirement variations, due to its limited energy/reserve

market participation. During June/July when system regulation requirement is lower, BESS regulation market revenue is lower, while its energy/reserve market revenue is higher and degradation cost is lower. During this period, 1) BESS has extra capacity for reserve market participation; 2) it buys less energy to compensate energy discharged due to AGC signal following; and 3) it has lower degradation cost due to reduced AGC signal following.

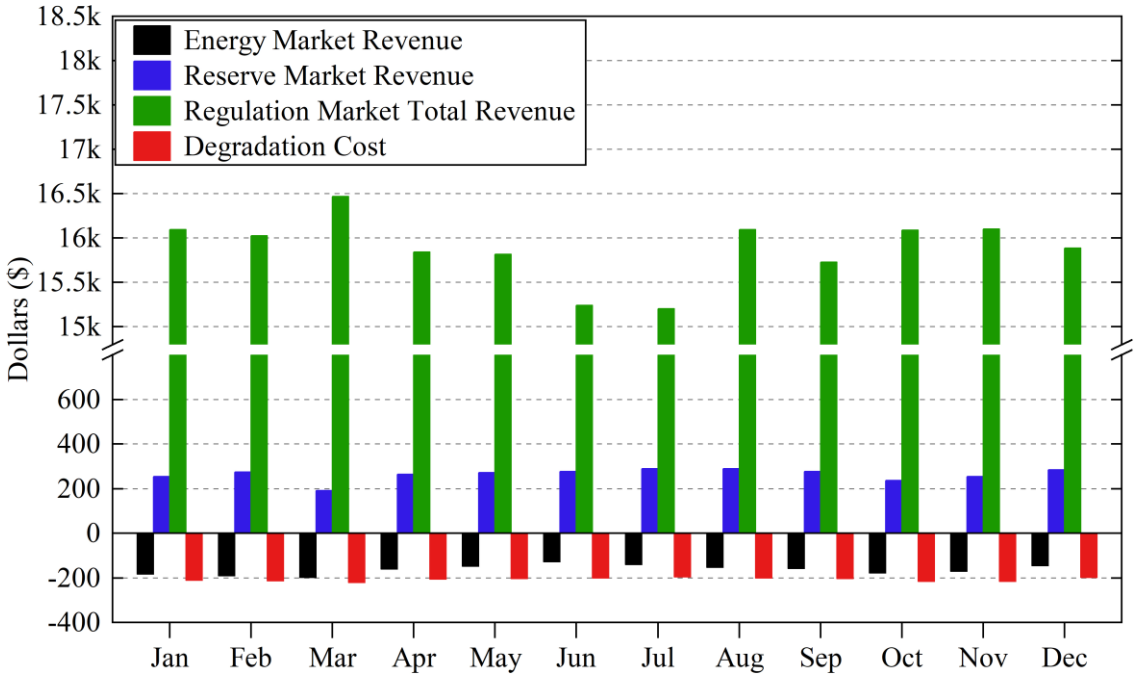

Figure 2.4 Degradation cost and revenue of BESS from each market in various simulations covering average monthly variations in load and reliability requirements of the system.

2.3.3 Analysis of the BESS's Capacity and Degradation Cost

A bi-parametric analysis is performed to study impacts of BESS capacity and replacement cost on BESS operations and market revenue. BESS capacity is changed from 100MWh to 2000MWh (step size = 100MWh). With a 4-hour operation duration, BESS charge/discharge limit changes from 25MW to 500MW (step size = 25MW). For each size level, we consider replacement costs of 200k$/MWh, 150k$/MWh, 100k$/MWh, 50k$/MWh, 25k$/MWh, and 1k$/MWh. Degradation costs vary with the replacement costs. To maintain degradation cost modeling accuracy, the number of degradation cost segments is varied based on BESS capacity variations. We perform 120 simulations to cover these variations. For each replacement cost, BESS total revenue and revenue from each market versus its capacity (and charge/discharge limit) are shown in Figure 2.5.

In Figure 2.5, regulation market revenue curves at various replacement costs increase as BESS capacity increases to 300MWh. Beyond 300MWh capacity, system regulation requirements are fully satisfied (i.e., saturated) by BESS. Hence, BESS regulation market revenue curves remain flat after 300MWh capacity. A knee-point happens on BESS total revenue curves when regulation market gets saturated. This indicates BESS total revenue increases slower when it cannot gain more profit from the regulation market. In existing systems, after expanding BESS capacity beyond a certain threshold, BESS total revenue growth rate may decrease significantly as the

BESSs saturate the regulation market and cannot gain significant revenue from the energy/reserve markets.

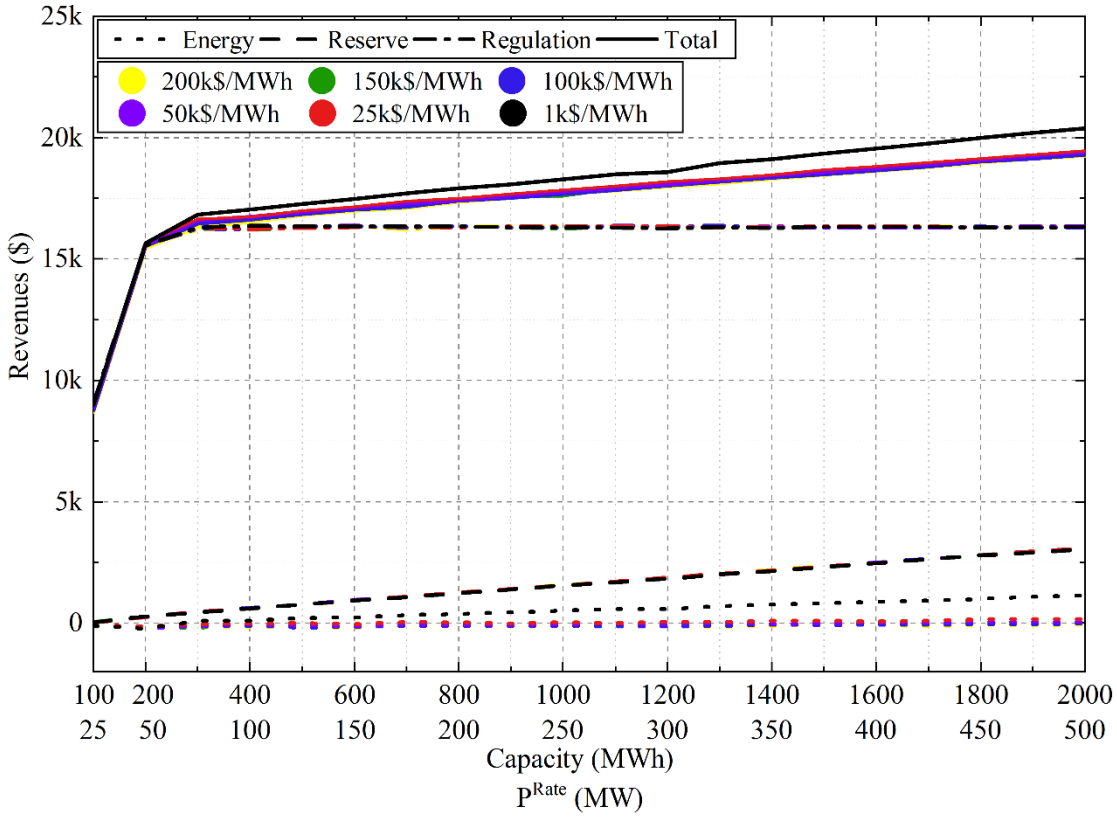

Figure 2.5 BESS's revenue versus its capacity and charge/discharge limit for different replacement costs. The BESS's total revenue and revenue from each market are represented using curves with specific patterns, and each curve is shown in different colors representing various battery replacement costs. E.g., the dotted black curve is the energy market revenue for a BESS with 1k$/MWh replacement cost. The horizontal axis is labeled with both BESS capacity (in MWh) and charge/discharge limit (in MW).

In Figure 2.5, except for total revenue curve and energy revenue curve at 1k$/MWh replacement cost, all other curves of the same pattern at different replacement costs overlap. This indicates 1) reducing the battery replacement cost does not affect the BESS's revenue from reserve and regulation markets; 2) BESS energy market participation is not profitable unless the replacement cost drops significantly (to 1k$/MWh). Once BESS energy market participation becomes profitable, after saturating the regulation market, BESS allocates its capacity in excess of ancillary services provision to the energy market.

In Figure 2.5, regardless of the replacement cost, BESS reserve revenue increases almost constantly as its capacity increases, since BESS reserve market participation is bounded by its capacity due to worst-case reserve deployment model. Its regulation revenue (before saturation) increases significantly faster than its energy/reserve revenue. This indicates BESS capacity and charge/discharge limit increment has more impact on its regulation revenue than on its energy/reserve revenue.

These results show: 1) compared to energy market, regulation/reserve markets are more profitable for BESSs, regardless of replacement costs; 2) BESS energy revenue could increase by reducing replacement cost significantly; 3) BESS regulation revenue depends more on charge/discharge limit; 4) BESS energy/reserve revenue increment depends on BESS capacity; 5) degradation cost modeling may not change BESS strategies in ancillary services markets, while it limits BESS energy market operation. This issue is further discussed in [41].

Studies in this section for degradation cost analysis are performed using 24-hour simulations for BESS's real-time market operations. The impact of degradation cost on the timeframe for BESS replacement is a long-term BESS planning problem (instead of the BESS real-time operation problem), which falls out of the scope of this section. This long-term planning problem could be investigated by optimization and simulation tools developed for long-term planning (instead of real-time operation) purpose. As these long-term planning problems typically involve much longer time horizon compared to the 24-hour real-time operation horizon adopted in this section, the models developed in this section (for real-time operation analysis) do not fit the purpose of long-term planning studies, as these models consider real-time BESS and market operation details which will lead to significant computational burden if directly applied to the simulation and optimization horizon for long-term planning problems. Therefore, model simplifications which fit the purpose of long-term planning studies will be needed for studying the impact of BESS degradation on the replacement timeframe of BESS.

2.4 Conclusion

This chapter proposes a bi-level framework for optimal strategies of price-maker BESSs in real-time energy, reserve, and regulation markets. To understand BESSs' excessive regulation market activities and the impact of degradation on BESS market strategies, an accurate degradation cost function is deployed in the BESS strategic bidding model, and an AGC signal dispatch model is proposed to model and simulate BESS AGC signal following activities. Case studies on a synthetic system with real-world data are performed to investigate BESS operating characteristics in the regulation market and energy/reserve markets, when BESS degradation, AGC signal following, and system annual load/ancillary service requirements variations are considered. Impacts of BESS capacity and replacement cost on its market revenue are also investigated.

Future research could focus on considering market uncertainties and renewable energy penetration for better evaluation of BESS's impact on energy and ancillary services markets.

3. Impact of Battery Degradation on Market Participation of Utility-scale Battery Energy Storage Systems (BESSs)

3.1 Introduction

The grid integration of battery energy storage systems (BESSs) is expanding rapidly, thanks to the BESS's desirable characteristics of being a fast, efficient, and flexible generating resource with the capability of multiple services provision [37]. BESSs are capable of providing a wide range of grid services including energy arbitrage, frequency regulation, reserve provision, resiliency enhancement, and renewable firming [42]. In recent years, the battery manufacturing cost has reduced, which encourages merchant BESSs to participate in the electricity markets. Since 2018, independent system operators (ISOs) in the US are required by the Federal Energy Regulatory Commission (FERC) Order 841 to remove barriers for BESS's participation in the various markets [17]. This order further motivates merchant BESSs to offer energy and ancillary services through the wholesale market. It also inspires the power industry and research community to thoroughly understand the BESS's operating patterns, revenue streams, and cost structures in the energy and ancillary services markets.

To study the market operation of merchant BESSs, existing literature models the merchant BESS as a price-maker in the market, since these utility-scale BESSs could impact market prices due to their capacity and technical characteristics [6–9, 11, 43]. Using the price-maker modeling approach, it is possible to study the optimal allocation of merchant BESS across various markets and analyze the impact of BESS's profit maximization activities on the ISO's market clearing outcomes.

In line with the works which focus on markets' design and structures [44], reference [6] compares three different market mechanisms for operation scheduling of a BESS in the energy market. This work is mainly focused on the market mechanism and does not deal with operational details of BESS and ancillary services markets. A comprehensive study on the operation of price-maker BESS in the energy market under various transmission congestion scenarios is performed in [7]. This work does not model ancillary services markets besides the energy market and also neglects the battery degradation cost. Studies on market operations of price-maker BESSs are enhanced in [8] by considering day-ahead energy and reserve markets and real-time balancing market. However, the frequency regulation market, which is one of the major revenue streams for BESSs in practical applications [42], is not considered in [8]. In [9], BESS is modeled as a price-taker in the energy market and price-maker in reserve and frequency regulation markets using a novel approach for price-maker modeling. Reference [9] models the most important markets for the operation of BESS and also considers parameter uncertainties in the model. However, this work neglects the battery degradation cost, which may lead to inaccurate results. In [27, 28], several accurate battery degradation cost models are developed and applied to studies considering BESS as a price-taker in the market. These price-taker models cannot capture the BESS's impact on market clearing outcomes and are insufficient for studying BESS's market operations.

To enable comprehensive analysis on the interactions between merchant BESSs and energy/ancillary services markets, we propose an optimization framework in Chapter 2 for the participation of price- maker BESS in real-time energy, reserve, and pay as performance frequency

regulation markets with an accurate degradation cost model. In Chapter 2, we also develop a market-based dispatch model for the automatic generation control (AGC) signals, in order to study the details of BESS operations in the regulation market.

Built upon our framework in Chapter 2, this chapter performs comparative case studies to investigate the impact of battery degradation on the operation scheduling and revenue/cost of a price-maker BESS in real-time energy, reserve, and pay as performance regulation markets. By including and removing the battery degradation cost model and detailed AGC signal dispatch model in the framework proposed in Chapter 2, we could determine the optimal scheduling of a price-maker BESS is real-time energy and ancillary services markets with and without considering the battery degradation cost in the decision-making process. Simulation results obtained using this framework with and without these two models (the degradation model and AGC signal dispatch model) on a synthetic test system are presented in four different cases, representing various market participation policies for the BESS. A comparative analysis of the case study results evaluated the impact of battery degradation on the BESS's market operation.

3.2 Frameworks Description

In Chapter 2, we propose an optimization framework to study the optimal participation of a price-maker BESS in real-time energy, reserve, and pay as performance frequency regulation markets. The framework contains comprehensive models for BESS operating limits, as well as details of ISO's joint market clearing procedure for real-time energy and ancillary services markets.

To study detailed interactions between BESS's profit maximization strategies and ISO's joint market clearing procedure across real-time energy, reserve, and regulation markets, the BESS is modeled as a price-maker using bi-level optimization framework with coupled upper and lower level problems. In the upper-level problem (ULP), BESS's owner maximizes its revenue across various markets within a certain time period, while the lower-level problem (LLP) simulates the ISO's joint market clearing procedure. BESS's quantity and price offers for each market at each market clearing interval serve as decision variables in the ULP and input parameters to the LLP, while market clearing prices (MCPs) and scheduled power of BESS serve as decision variables in the LLP and input parameters to the ULP.

Figure 3.1 shows the structure and main components of the framework in Chapter 2 considering battery degradation cost. The coupling between ULP and LLP is represented by terms in blue. To establish a framework without considering battery degradation, terms in red are removed from the framework in Chapter 2. Both frameworks (with and without battery degradation) share the same LLP but differ in the ULP. A general description of the ULPs and the common LLP for both frameworks is presented below. Detailed equations for the frameworks with and without modeling battery degradation cost can be found in Chapter 2.

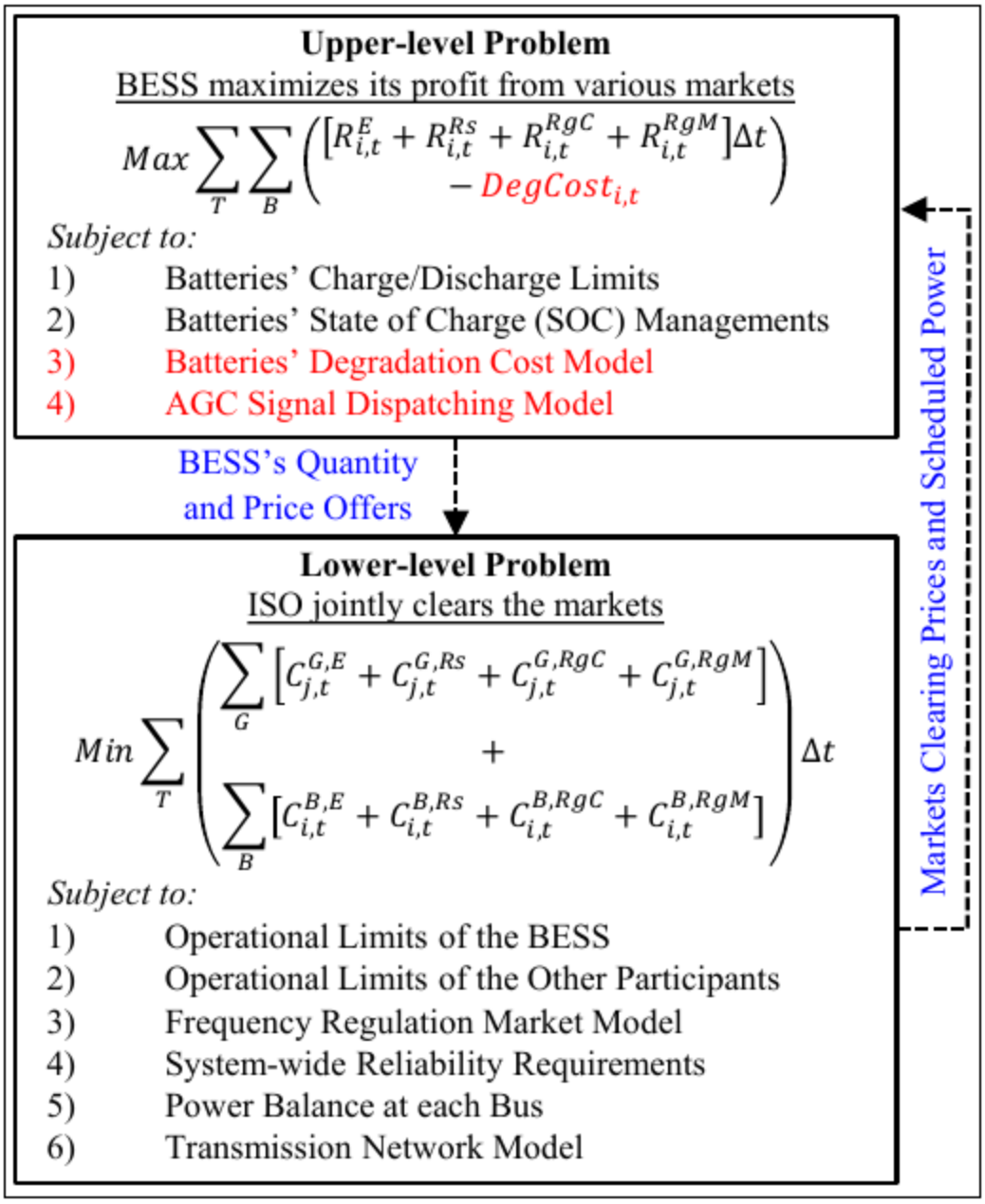

Figure 3.1 Structure of the optimization frameworks. T denotes the studied time period; B denotes the set of all battery units owned by a BESS owner; G denotes the set of all the other generating units in the market; Δt denotes the length of each market clearing interval; $R_{i,t}^{E}$, $R_{i,t}^{Rs}$, $R_{i,t}^{RgC}$, $R_{i,t}^{RgM}$ denote the BESS's revenue obtained using battery unit i from energy, reserve, regulation capacity and regulation mileage markets at market clearing interval t, respectively; $Deg_{i,t}^{Cost}$ denotes the degradation cost of battery unit i during market clearing interval t; $C_{i,t}^{B,E}$, $C_{i,t}^{B,Rs}$, $C_{i,t}^{B,RgC}$, $C_{i,t}^{B,RgM}$ denote the operating costs of battery unit i in the energy, reserve, regulation capacity and regulation mileage markets at market clearing interval t, respectively; $C_{j,t}^{G,E}$, $C_{j,t}^{G,Rs}$, $C_{j,t}^{G,RgC}$, $C_{j,t}^{G,RgM}$ denote the operating costs of generating unit j in the energy, reserve, regulation capacity and regulation mileage markets at market clearing interval t, respectively.

3.2.1 Upper-level Problem (ULP)

In the ULP, the BESS owner who has several battery storage units at different buses maximizes its revenue from the real-time energy, spinning reserve, and pay as performance frequency regulation markets while considering its operating limits, including or not including the battery degradation cost. The ULP of each framework is described below.

3.2.1.1 Framework without Degradation Cost Model

In this framework, components of the ULP are represented by terms in black in Figure 3.1. The objective function maximizes BESS's total revenue from energy, reserve, regulation capacity, and regulation mileage markets across a certain time period and across all the battery units at different buses. Each revenue term is calculated by multiplying the battery unit's dispatched power and corresponding MCP. Revenue from the energy market can be positive or negative in each market clearing interval as BESS may sell (i.e., discharge) or buy (i.e., charge) energy in each interval. Revenue from the reserve market is paid to each unit for reserving its output for contingency conditions. Revenue from the regulation market consists of regulation capacity payment, which is paid based on the unit's reserved capacity for regulation services provision; and regulation mileage payment, which is paid based on the unit's contribution toward following system-level AGC signals.

Reserve services deployment is modeled in neither of the frameworks as it is related to contingency analysis. In this framework (without degradation cost model), AGC signal deployment is modeled by assuming that AGC signals have zero-mean over each market clearing interval. These zero-mean AGC signals are provided by ISOs like PJM and ISO New England (ISO-NE) [45]. This assumption indicates following AGC signals 1) will not change the battery unit's state of charge (SOC) across each market clearing interval; 2) will not cause additional cost to BESS owners if battery degradation is neglected. Therefore, a dispatch model for AGC signals is not needed when battery degradation cost is not considered.

The constraints of the ULP in this framework include: 1) Batteries' charge/discharge limits: these constraints ensure the quantity offer of BESS for each market is within the battery units' charge/discharge limits. Also, the accumulated dispatched power for various services in each market clearing interval should not violate the charge/discharge limits of the batteries. 2) Batteries' SOC management: these constraints keep track of the changes in the battery unit's SOC in each market clearing interval, which are resulted from BESS's participation in various markets. These constraints also ensure the SOC lies within its upper/lower limits and force BESS to have the same SOC at the beginning and end of each day.

3.2.1.2 Framework with Degradation Cost Model

In Figure 3.1, terms in red represent components that are added to the ULP of the previous framework to build the framework considering battery degradation costs. By subtracting the degradation cost term from the objective function and adding a group of constraints for modeling degradation costs, the battery degradation costs are calculated based on a linear approximation of the rainflow algorithm [27]. Rainflow algorithm is an accurate method for battery degradation cost

modeling, which counts the number of charge/discharge cycles in the battery's operation period and assigns costs to them based on the depth of the cycles. It means that having charge/discharge cycles with lower depth results in less degradation cost.

To obtain degradation cost accurately during BESS's AGC signal following activities, each battery unit's contribution toward following system-level AGC signals needs to be properly modeled. This is handled by the AGC signal dispatching model in the constraints of the ULP, where a participation factor is defined to dispatch system-level AGC signals based on market outcomes.

3.2.2 Lower-level Problem (LLP)

As shown in Figure 3.1, the LLP models ISOs' joint market clearing process, and it is similar in both frameworks. The LLP objective function minimizes the total operating cost of real-time energy, reserve, regulation capacity, and regulation mileage markets across a certain time period, considering the operating costs of the BESS and other non-battery market participants. Each cost term is calculated by multiplying each unit's price offer to its scheduled power. The BESS's price offers are input parameters from the ULP. It is assumed that BESS can perfectly predict price offers of other participants.

The following six groups of constraints are considered for the LLP, as shown in Figure 3.1. 1) Operational limits of BESS: these constraints limit each battery unit's scheduled power for each market below its corresponding quantity offer. 2) Operational limits of other participants: minimum and maximum generation limits of other participants are maintained in these constraints along with ramping limits. 3) Frequency regulation market model: these constraints model the impact of each unit's historical performance in regulation services provision on its current dispatch in the regulation market. 4) System-wide reliability requirements: these constraints ensure that, during each market clearing interval, the system ancillary services requirements are satisfied by the scheduled power of BESS and other market participants. The corresponding dual variables are MCPs for reserve, regulation capacity, and regulation mileage provisions. 5) Power balance at each bus: these constraints enforce the Kirchhoff's current law at each bus. The corresponding dual variables are locational marginal prices (LMPs) at various buses. 6) Transmission network model: these constraints calculate transmission line power flow and enforce line thermal limits.

Using the conversion procedure in [30], both bi-level frameworks are converted to mixed integer linear programming (MILP) to be solved using available commercial solvers.

3.3 Case Studies and Comparative Analysis

The above two optimization frameworks enable us to evaluate the impact of battery degradation cost on BESS's operations in various markets. This section investigates such impact through four comparative case studies performed on the above optimization frameworks under different market participation scenarios of BESS. In Chapter 2, several case studies are performed to evaluate the performance of the framework with battery degradation. This section focuses on understanding how battery degradation cost could affect BESS's market participation and profit maximization activities, through comparing simulation results obtained using both frameworks (with and without considering battery degradation).

3.3.1 The Test System

To have a synthetic test system built upon real-world data, the IEEE reliability test system (RTS), updated by Grid Modernization Laboratory Consortium, i.e., RTS-GLMC, is adopted for the case studies [34]. The simulations are performed on the third area of the RTS-GMLC network. This test system consists of 25 buses, 39 transmission lines, 26 generators, and a battery unit on Bus 13. The simulation horizon is 24 hours with 15-minute market clearing intervals (i.e., 96 market clearing intervals in total). The AGC signals are dispatched every 20 seconds for the framework with the degradation cost model and AGC signal dispatch model.

System load, reserve, and regulation capacity requirements for the simulation horizon are determined by averaging the summer (June to August) load and ancillary services requirements of the third area in the RTS-GMLC. During the 24-hour simulation horizon, the system load varies between 1285 MW and 2345 MW. The system peak and valley loads happen in Hours 11-18 and Hours 1-6, respectively. Hence, it is expected that the energy market price reaches its highest and lowest values in respectively Hours 11-18 and Hours 1-6.

In each market clearing interval, the system's regulation mileage requirement is set to be 1.5 times the regulation capacity requirement. The sample AGC set points, provided by ISO-NE, are modified for AGC signal modeling [35]. The modified AGC signals have zero-mean over each 15-minute market clearing interval. In each market clearing interval, the total variation of the modified AGC signals is equal to the corresponding system regulation mileage requirement.

It is assumed, in each market clearing interval, each generator's price offer for the energy market is equal to the generation cost. Generator price offers for reserve, regulation capacity, and regulation mileage markets are 0.15, 0.4, and 0.07 times their energy price offers, respectively. The multipliers used for calculating ancillary services' price offers are derived from PJM historical data by averaging over the ratio of each ancillary service price to the energy price [36].

The BESS owner has a lithium-ion battery unit at Bus 13 with the operational parameters specified in Table 3.1. The useful life of the battery is 6000 full charge/discharge cycles with cycle depth of 80% [37], and the battery replacement cost is 200 k$/MWh price. This information is used for incorporating the battery degradation cost into the framework with the degradation cost model. Details on the degradation cost function can be found in [43].

Table 3.1 Operational information of the battery unit

(Dis)charge limit (MW)	Storage Capacity (MWh)	Min SOC (MWh)	Max SOC (MWh)	Initial SOC (MWh)	(Dis)charge Efficiency (%)
50	200	20	180	90	95

3.3.2 Case 1: Energy Market

This case compares the BESS's performance with and without modeling its degradation cost, when the BESS only participates in the energy market. Figures 3.2(A) and 3.2(B) show the BESS's

scheduled power (in MW) and SOC (in MWh) when the BESS participates in the energy market only, without and with the degradation model, respectively.

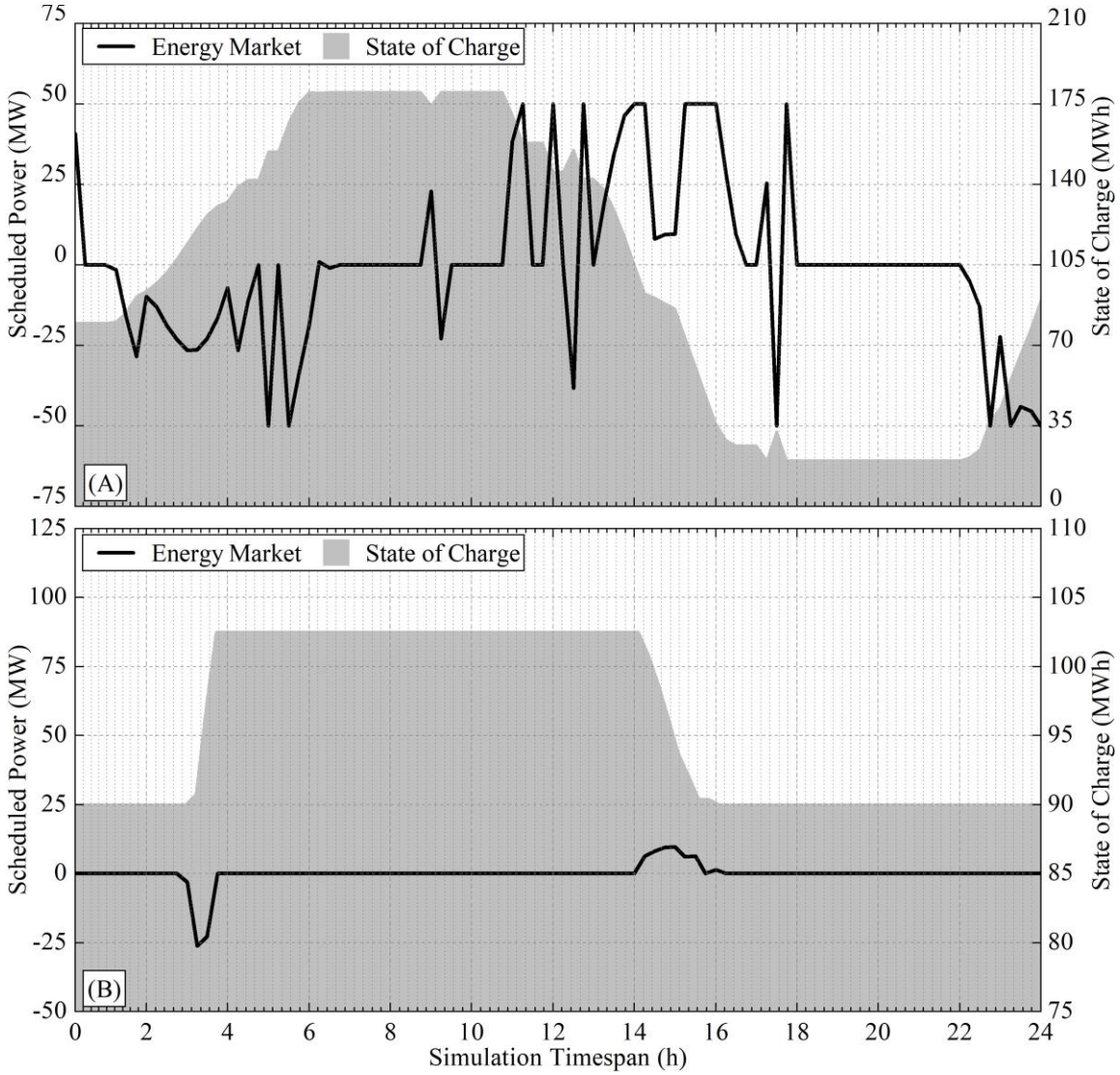

Figure 3.2 Scheduled power and SOC of BESS when it participates in energy market only, using (A) framework without degradation cost model; (B) framework with degradation cost model. The black curve denotes BESS's scheduled power in energy market; The grey area denotes the BESS's SOC.

Figure 3.2(A) shows when degradation costs are neglected, energy arbitrage between hours is a profitable bidding strategy for a BESS only participating in the energy market. Hence, the BESS buys energy (with negative scheduled power) and charges itself (with an increase in the SOC) during initial hours with lower energy prices (hours 1-6), in order to sell the stored energy during hours with higher energy prices (hours 11-18). As shown in Figure 3.2(A), BESS uses all its available capacity for this inter-temporal energy arbitrage. The BESS also experiences deep charge/discharge cycles for maximizing its revenue, which, in real-world practices, may result in considerable battery life loss and degradation cost.

Figure 3.2(B) shows when degradation costs are considered in the BESS's bidding strategies, the BESS's participation in the energy market is very limited. It only buys 12 MWh energy once during off-peak hours (hours 3-4) and sells this amount of energy once during peak hours (hours 14-16). In this case, when battery degradation is considered, participating in the energy market does not generate enough revenue to overcome the total degradation cost. Therefore, the BESS limits its participation in the energy market.

3.3.3 Case 2: Energy and Reserve Markets

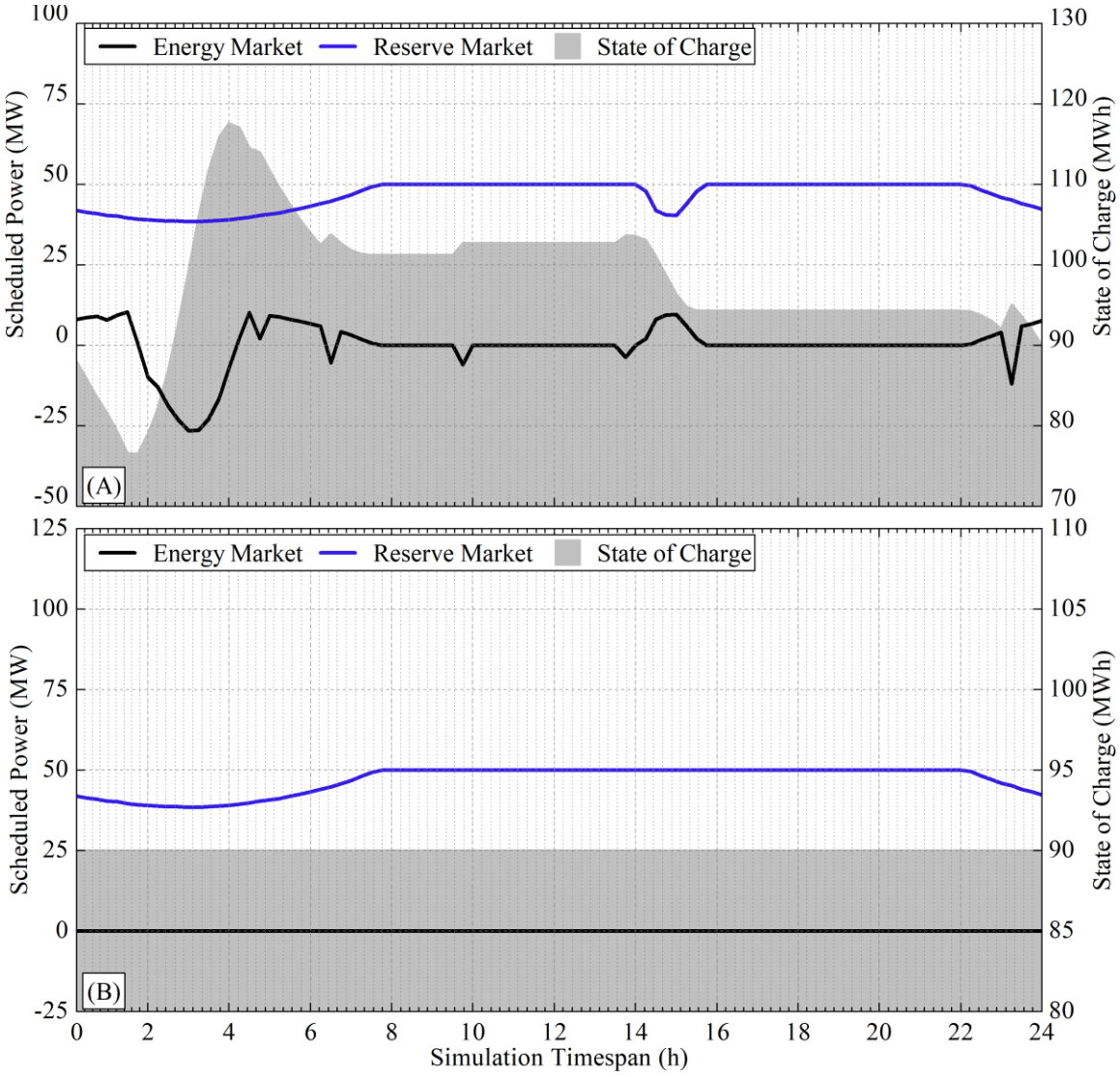

Figure 3.3 Scheduled power and SOC of BESS when it participates in energy and reserve markets, using (A) framework without degradation cost model; (B) framework with degradation cost model. The black and blue curves denote BESS's scheduled power in energy and reserve markets, respectively; The grey area denotes the BESS's SOC.

This case compares the BESS's performance with and without modeling its degradation cost, when the BESS participates in both energy and reserve markets. Figures 3.3(A) and 3.3(B) show the BESS's scheduled power (in MW) and SOC (in MWh) when the BESS participates in the energy and reserve markets, without and with the degradation model, respectively.

In Figure 3.3(A), the BESS prefers participating in the reserve market more than the energy market. In most hours, the BESS's scheduled power in the reserve market reaches its 50 MW charge/discharge limit. The BESS also performs inter-temporal energy arbitrage to gain revenue from the energy market, but the amount of energy arbitrage is limited as the BESS reaches its charge/discharge limit. BESSs with higher charge/discharge limits may participate more in the energy market.

As shown in Figure 3.3(B), when the degradation cost is modeled, the reserve market becomes the only source of revenue for BESS, and BESS does not participate in the energy market. In essence, as reserve deployment is not modeled in this work, participation in the reserve market does not incur any degradation cost for the BESS. Hence, BESS provides reserve services as much as it can and does not perform any energy arbitrage between hours as the revenue generated by this activity does not overcome the degradation cost in this test system. In this case, the battery degradation does not have a significant impact on the BESS's operation in the reserve market, but this degradation reduces the BESS's energy market participation significantly.

3.3.4 Case 3: Energy and Frequency Regulation Markets

This case compares the BESS's performance with and without the degradation cost model, when the BESS participates in both energy and regulation markets. Figures 3.4(A) and 3.4(B) show the BESS's scheduled power (in MW) and SOC (in MWh) when the BESS participates in the energy and regulation markets, without and with the degradation model, respectively.

In this case, the simulation results without (Figure 3.4(A)) and with (Figure 3.4(B)) the degradation cost model are more similar to each other than those in the previous cases. Under both frameworks, the BESS participates the most in the frequency regulation market. In Figure 3.4(A), when battery degradation is neglected, BESS also participates in the energy market and performs energy arbitrage when its scheduled power for regulation capacity provision does not reach its charge/discharge limit at the beginning and end of the day. A BESS with a higher charge/discharge limit may participate more in the energy market. In Figure 3.4(B), when battery degradation is considered, the BESS limits its energy market participation to only compensating for the energy discharged due to following AGC signals. Although the AGC signals have zero-mean over each market clearing interval, the battery's charge/discharge efficiency is not 100%. In the framework with models for the degradation cost and AGC signal dispatch, this fact leads to a SOC reduction when the BESS follows the AGC signals. Therefore, BESS needs to compensate for the energy discharged due to AGC signal following to maintain a similar SOC at the beginning and end of the day.

The SOC curve of Figure 3.4(B) has small fluctuations (on top of the overall shape) all over the simulation horizon. These fluctuations are low-depth charge/discharge cycles caused by following AGC signals. As these low-depth charge/discharge cycles will result in low degradation costs, the

BESS's regulation market participation will not cause significant degradation costs. Hence, degradation cost modeling in these simulations does not affect the operation pattern of BESS in the regulation market a lot, and this pattern is similar in 3.4(A) and 3.4(B).

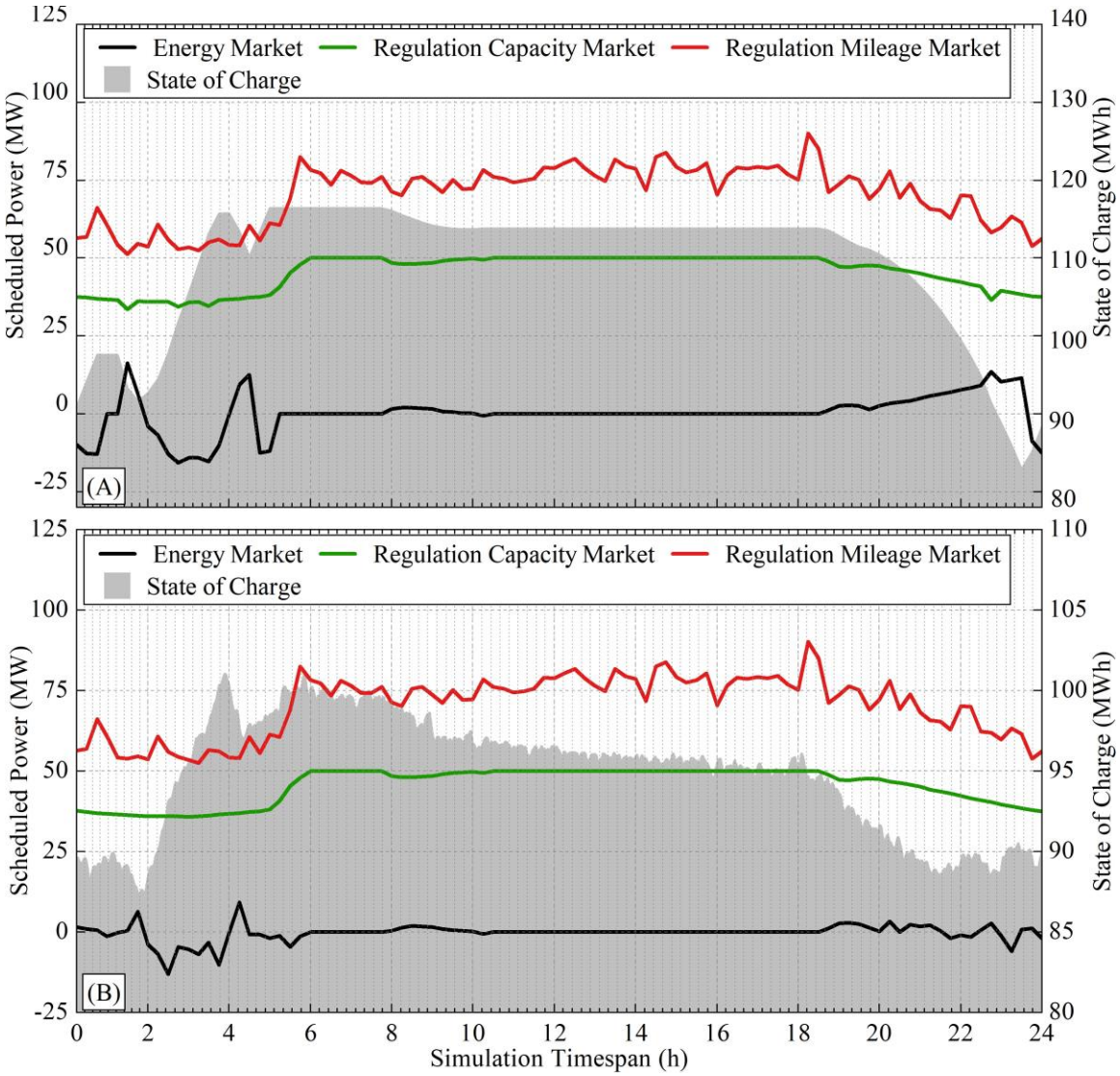

Figure 3.4 Scheduled power and SOC of BESS when it participates in energy and regulation markets, using (A) framework without degradation cost model; (B) framework with degradation cost model. The black, green, and red curves denote BESS's scheduled power in energy, regulation capacity, and regulation mileage markets, respectively; The grey area denotes the BESS's SOC.

3.3.5 Case 4: Energy, Reserve and Frequency Regulation Markets

This case compares the BESS's performance with and without modeling its degradation cost, when the BESS participates in all the energy, reserve, and regulation markets. Figures 3.3(A) and 3.3(B) show the BESS's scheduled power (in MW) and SOC (in MWh) when the BESS participates in these markets, without and with the degradation model, respectively.

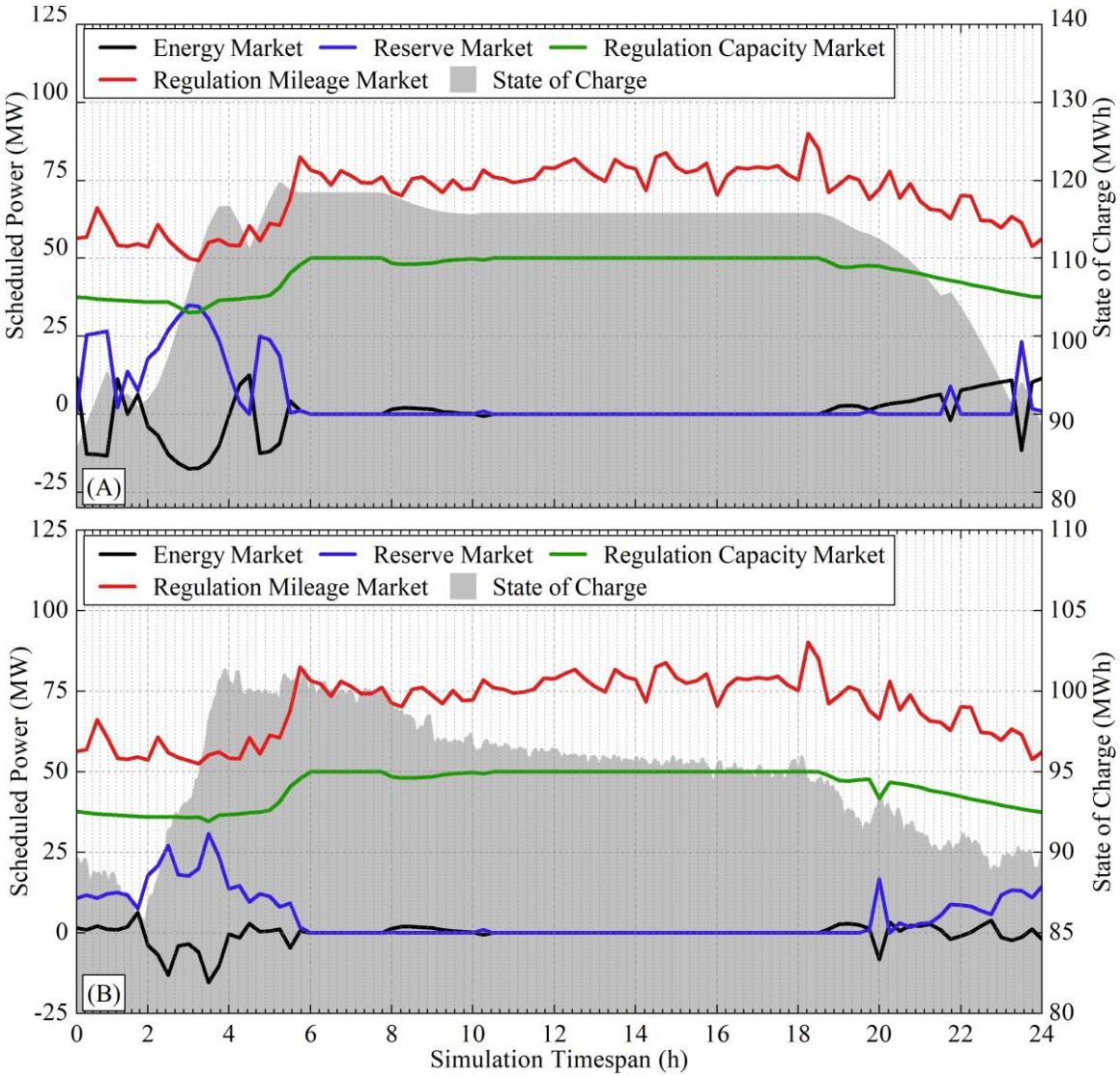

Figure 3.5 Scheduled power and SOC of BESS when it participates in energy, reserve, and regulation markets, using (A) framework without degradation cost model; (B) framework with degradation cost model. The black, blue, green, and red curves denote BESS's scheduled power in energy, reserve, regulation capacity, and regulation mileage markets, respectively; The grey area denotes the BESS's SOC.

Comparison of Figure 3.5(A) with Figure 3.5(B) shows that similar to the previous cases, the operation of BESS in ancillary services markets does not change a lot by considering degradation costs in this test system. This happens since 1) the reserve deployment is not modeled; and 2) providing regulation services does not cause high degradation costs. However, the BESS's energy market participation is reduced after considering degradation costs, since doing energy arbitrage in the energy market is less profitable for BESSs with degradation costs.

3.3.6 Comparative Analysis for BESS's Revenue and Cost

Figure 3.6 shows the BESS's total revenue from each market and its degradation cost in Cases 1-4, using frameworks with and without the degradation cost model.

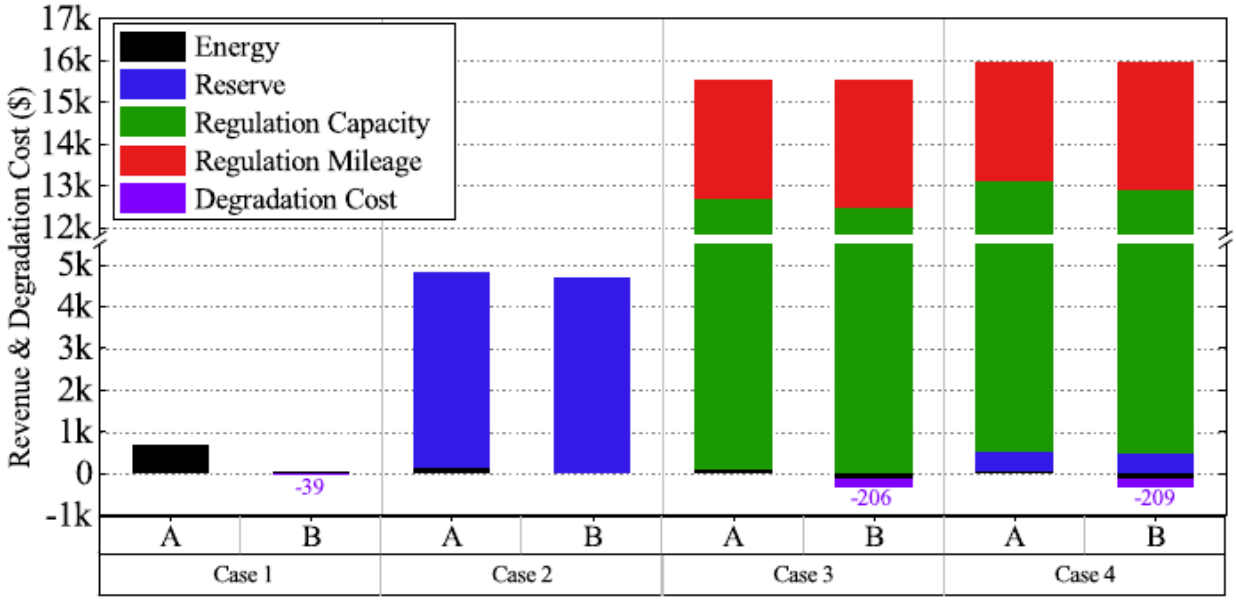

Figure 3.6 BESS's total revenue from each market and its degradation cost in Cases 1-4, using (A) framework without degradation cost model; (B) framework with degradation cost model.

Comparison of Bar A with Bar B for each case in Figure 3.6 validates our previous observations for this synthetic test case system build upon real-world data. First, considering batteries' degradation cost in BESS operation scheduling significantly reduces BESS's participation and revenue in the energy market. Second, BESS's participation and revenue in reserve and regulation markets do not change significantly by modeling degradation costs. However, modeling reserve deployment in the studies may affect the results for the reserve market.

Figure 3.4(B) and Figure 3.5(B) show the degradation costs in Cases 3-4 are mostly associated with the BESS's regulation market participation and AGC signal following. Figure 3.6 shows the total degradation costs in Cases 3-4 are around 1% of the BESS's revenue from the regulation market, which is negligible in comparison to the revenue. Therefore, neglecting the degradation costs caused by AGC signal following should not have a considerable impact on the results. This neglection could significantly reduce the optimization complexity and computation time. It could be adopted in future work when other BESS/market operational details need to be considered.

3.4 Conclusion

Based on our proposed frameworks for the participation of a price-maker BESS in real-time energy, reserve, and pay as performance frequency regulation markets with and without battery degradation cost model, this chapter conducts comparative case studies to investigate the impact of battery degradation on BESS's revenue, cost, and operations in energy and ancillary services

markets. Simulation results using synthetic test system build upon real-world data shows that 1) considering degradation cost may significantly reduce BESS's energy market participation; 2) the BESS's participation pattern in the reserve and regulation markets is not significantly impacted by the battery degradation cost.

Future work can be focused on considering parameter uncertainties, studying other ancillary services markets, and modeling renewable resources in the frameworks.

4. Integrating BESSs the Electricity Market: Conceptual Framework and Case Study

Nomenclature

Indices and Sets

t	Index for time periods, running from 1 to T.
ω	Index for scenarios, running from 1 to Ω.

Constants and Parameters

π_ω	Probability of scenario ω.
M	Large auxiliary constant.
P_t^{Vmax}	Maximum virtual bidding capacity at time t.
α	Per-unit confidence level.
β	Risk-aversion degree ranging from 0 to 1.
γ_t	Conversion efficiency of the battery energy storage system (BESS) at time t.
E^{min}	Minimum state of charge of the BESS.
E^{max}	Maximum state of charge of the BESS.
$P_{t,\omega}^{\overline{ST+}}$	Maximum charging active power for the BESS at time t and scenario ω.
$P_{t,\omega}^{\overline{ST-}}$	Maximum discharging active power for the BESS at time t and scenario ω.

Decision Variables

$E_{t,\omega}$	State of charge of the BESS at time t and scenario ω.
$P_{t,\omega}^{DA}$	Total power purchased in the day-ahead market at time t and scenario ω.
$P_{t,\omega}^{RT}$	Total power purchased in the real-time market at time t and scenario ω.
$P_{t,\omega}^{VI}$	Power sold in the day-ahead market though incremental virtual bidding.
$P_{t,\omega}^{VD}$	Power bought in the day-ahead market through decremental virtual bidding.
$P_{t,\omega}^{ST+}$	Charging active power for the BESS at time t and scenario ω.
$P_{t,\omega}^{ST-}$	Discharging active power for the BESS at time t and scenario ω.
ζ, η	Auxiliary variables used to compute the CVaR.
z_t	Binary variable used to determine the virtual bidding strategy at time t.
$u_{t,\omega}^{ST}$	Binary variable used to determine the status of BESS.

Random Variables

$\lambda_{t,\omega}^{DA}$	Day-ahead electricity price at time t and scenario ω.
$\lambda_{t,\omega}^{RT}$	Real-time electricity price at time t and scenario ω.
$P_{t,\omega}^{N}$	Net power demand from retail's customers at time t and scenario ω.
$P_{t,\omega}^{RE}$	Actual renewable energy production at time t and scenario ω.

4.1 Introduction

Assessing the impact of stacked BESS on the electricity is in recent years becoming of great concern to both individuals, corporations, and governments around the world. This movement towards the large-scale adoption of renewable energy resources can be seen around the globe as different continents race towards reducing the carbon footprint. In recent years, energy storage has proven to be very helpful in maintaining grid reliability and also in helping increase capacity of power producers participating in day-ahead and real-time energy markets. It also helps to increase the power capacity of individuals that generate electricity using large- or small-scale resources. The benefits of market integration of BESSs include cost savings, increased reliability and resilience, and reduced environmental impacts.

This chapter presents a conceptual framework for the integration of BESSs in the wholesale and retail electricity markets. The proposed market framework illustrates how BESS owners are integrated into the grid and also how they are able to interconnect with other BESS owners locally and share resources such as peer-to-peer energy trading. Then, a stochastic decision-making model for an electricity retailer with BESS and virtual bidding is proposed and validated through case studies. The proposed model minimizes the retailer's expected procurement cost and determines the optimal bidding curves to be submitted in the wholesale electricity market.

4.2 Conceptual Framework

The conceptual electricity market framework in this chapter is divided into two parts: retail and wholesale markets which are presented separately in Section 4.2.1 and 4.2.2, respectively, and integrated in Section 4.2.3.

4.2.1 Retail Electricity Market

The retail market framework shown in Figure 4.1 illustrates how BESS are integrated into the power grid and also how they are able to interconnect with other BESS locally and share resources using technologies such as peer-to-peer energy. Stage 1 represents the distributed generation such as PV panels that can be installed on the rooftops of homeowners. In stage 2, the hybrid inverter charger is installed, the current generated by the distributed generation is used to recharge the batteries and subsequently used in homes or being sent to the grid. Stage 3 represents energy storage. The stored energy can be utilized later when generation has gone down especially in the night and can also be sent to the grid at peak periods when demand exceeds supply. In stage 4, the generated/stored energy is used in the home and there is also a backup energy from the power grid

through the smart meter to the home. This is necessary to provide electricity to the home in case the solar panel and energy storage fails. It is also used to make sure that all the electricity users in an area can be under an umbrella so that if there is an emergency on the grid that requires shutting down power for certain areas, that there will not be homes that will have power so as to protect the technicians that will be working on the grid when these breakdowns occur. In stage 5, the electricity smart meter is used to keep record of the amount of electricity generated, used, and transacted. It records the amount of excess generated or stored electricity sent to the grid, aggregators and to other prosumers participating in the local peer-to-peer energy trading. It also records the amount of energy received from the electricity grid to power the home when the generated/stored electricity is not sufficient to satisfy the demand. Stage 6 shows the electricity grid and its bi-directional transaction between the smart meter. Stage 7 shows the aggregators receiving energy through the bi-directional meter which keeps the record of the transactions. In stage 8, there is bi-directional transaction between other prosumers and other homeowners through the smart meter. This means that, if there is insufficient energy generated or stored for the home, energy can be purchased from other prosumers in the peer-to-peer energy market instead of going to the power grid.

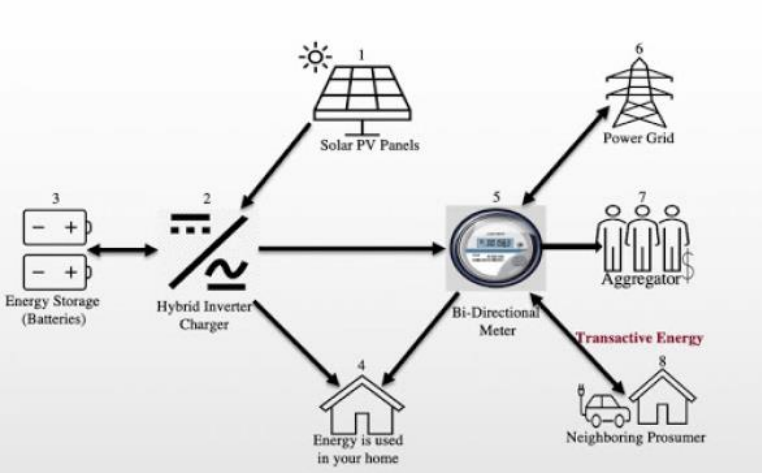

Figure 4.1 Conceptual retail market framework for BESSs.

4.2.2 Wholesale Electricity Market

The wholesale electricity market is a marketplace where electricity produced by large generators and consumed by large consumers of entities that resell that power to meet end-user demand. Most of these resellers are the utility companies and retailers. However, some utility companies also generate and sell directly to end-users. The clearing price for electricity in these wholesale markets is determined by an auction in which generation resources offer a price at which they can supply a specific number of megawatt-hours of power. Figure 4.2 shows the wholesale electricity market framework. Energy generated from renewable and nonrenewable sources can be traded in the wholesale market or be stored in utility-scale storage units to be utilized during the periods of low generation or high demand. Utility-scale BESSs are extremely important to ensure the reliability and resilience of power grids around the world. They can participate in energy markets and different ancillary services markets such as energy imbalance, reserve, and frequency response markets.

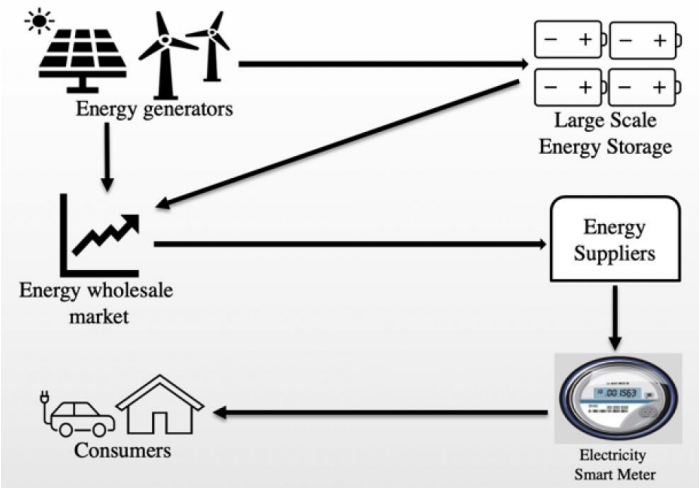

Figure 4.2 Conceptual wholesale market framework for BESSs.

4.2.3 Integrating Retail and Wholesale Electricity Markets

Figure 4.3 illustrates an integrated framework for retail and wholesale electricity markets. In this framework, two types of BESSs are considered. Utility-scale BESSs participate directly in the wholesale market whereas small-scale BESSs can participate in the local retail market or be aggregated to the wholesale market. The aggregation of small-scale BESSs is particularly important to reduce the dependency on large-scale resources and promote greater flexibility and decentralization. However, it increases the complexity of the market operations as several aggregators need to coordinate multiple transactions from thousands or millions of widespread distributed energy resources in the power grid.

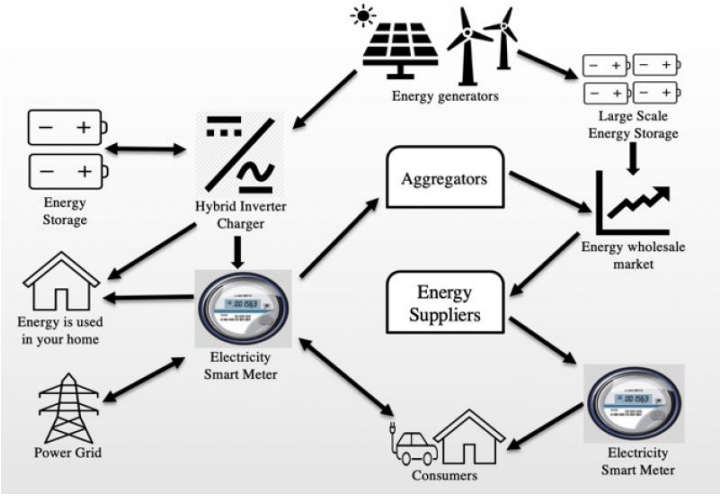

Figure 4.3 Conceptual wholesale market framework for BESSs.

4.3 Case Study: A Decision Model for an Electricity Retailer with BESS and Virtual Biding

4.3.1 Background

Many countries around the world have partially or fully deregulated their electricity markets in order to promote greater liberalization, competition, and innovation and better quality of services [113]. In deregulated retail electricity markets, end-user consumers are able to choose from different suppliers, energy sources and services, and still be served by the existing poles, distribution lines, and substations, which are maintained by one local utility company. In Europe, nearly 30 countries have adopted deregulated retail electricity markets [113]. In the United States, more than 20 states have implemented full or partial retail competition, also known as retail choice, which allow customers in the distribution grid to choose their electricity supplier [114]. According to a study conducted by the Federal Reserve Bank of Dallas [115], the adoption of competitive retail electricity markets in the United States contributed to lower electricity rates to end customers in states with high customer participation. Furthermore, the retail electricity market liberalization helped increase market efficiency and promoted diversification of products and services, thus enabling retail customers in many jurisdictions to have different contract options, participate in demand response (DR) mechanisms, and purchase energy from different sources.

Electricity retailers are essential agents in deregulated electricity markets since they operate as intermediaries between large power producers and end consumers without the need of operating and maintaining physical assets in transmission and distribution grids [116]. Retailers procure electricity mainly from bilateral contracts, self-production, and the wholesale electricity market, which generally incorporates uncertainties on day-ahead and real-time prices and incur in additional risks in their decision-making models for electricity procurement [117]. Several decision-making models for electricity retailers have been recently proposed in the literature to determine short-, medium-, and long-term strategies and decisions. An overview of the state of the art in decision-making models for electricity retailers was provided in [118] and [119]. Most of the existing works focused on the integration of price-based, incentive-based, combined, and contract-based DR mechanisms.

A two-stage stochastic optimization model is proposed in this chapter to determine the short-term decisions of an electricity retailer with self-production of renewable energy, BESS, and virtual bidding. The proposed model minimizes the retailer's expected procurement cost and determines the optimal bidding curves to be submitted in the wholesale electricity market [120].

4.3.2 Assumptions and Decision-Making Framework

The proposed decision-making framework for an electricity retailer is illustrated in Figure 4.4. Initially, historical data from day-ahead and real-time market prices, renewable energy production, and customers' load is collected. Then, scenarios are generated to be used in the stochastic programming model. The scenario generation and reduction process is described in Section 4.3.3. The first-stage decisions, also known as here-and-now decisions, comprise the retailer's involvement in the day-ahead market by submitting a non-increasing bidding curve to purchase energy and participate in virtual bidding with uncertainty on market prices, self-production of

renewable energy, and customers' load. The retailer is assumed to be a price-taker agent in the electricity market. Virtual bidding, also known as convergence bidding [121]-[122], is a pure financial instrument used to explore arbitrage opportunities in multi-settlement electricity markets. Electricity markets can participate in virtual bidding without necessarily having physical generation or load assets. By submitting a decremental virtual bidding curve in the day-ahead market, an electricity retailer can purchase energy from the day-ahead market and sell it in the real-time market at a higher price. On the other hand, if the forecasted day-ahead price is higher than the forecasted real-time price at specific hour, the retailer can purchase energy from the real-time market and sell it in the day-ahead market at a higher price. The second-stage decisions, also known as wait-and-see decisions, comprise the retailer's involvement in the real-time market and the optimal BESS charging and discharging decisions for each scenario. The retailer's objective is to minimize its expected procurement cost, and the outputs of the proposed model are the optimal power and virtual bidding curves, as illustrated in Figure. 4.4.

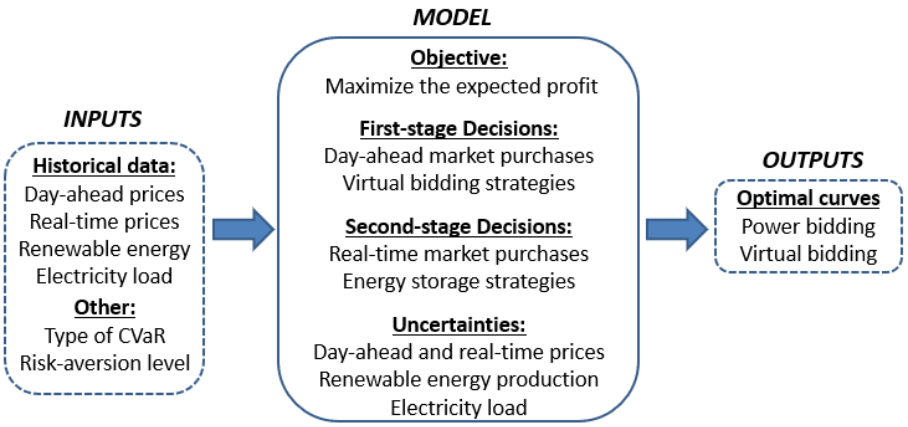

Figure 4.4 The proposed problem framework.

4.3.3 Scenario Generation and Reduction

Initially, a large number of scenarios are generated for day-ahead and real-time prices, electricity demand, and renewable energy production using a seasonal autoregressive integrated moving average (SARIMA) time series model, where a stochastic process Y is expressed using the following mathematical expression [123]:

$$\left(1-\sum_{g=1}^{p}\boldsymbol{\phi}_g\boldsymbol{B}^{g}\right)\left(1-\sum_{i=1}^{P}\Phi_i\boldsymbol{B}^{iS}\right)(1-\boldsymbol{B})^{d}(1-\boldsymbol{B}^{s})^{D}\boldsymbol{y}_t = \left(1-\sum_{h=1}^{q}\boldsymbol{\theta}_h\boldsymbol{B}^{h}\right)\left(1-\sum_{j=1}^{Q}\boldsymbol{\theta}_i\boldsymbol{B}^{jS}\right)\boldsymbol{\varepsilon}_t \quad (4.1)$$

In (4.1), $\boldsymbol{\phi}_g$ are the autoregressive parameters; $\boldsymbol{\theta}_h$ are the moving-average parameters; Φ_i are the seasonal autoregressive parameters; $\boldsymbol{\theta}_i$ are the seasonal moving-average parameters; $\boldsymbol{\varepsilon}_t$ is the term that represents the error which is assumed to be a normally distributed stochastic process; and B

is the backward shift operator. After the scenarios are generated by the SARIMA model, a fast-forward scenario reduction algorithm [124] is employed to reduce the number of scenarios of each stochastic variable to ensure that the model is tractable and still preserves sufficient stochastic information in the scenario set.

4.3.4 Mathematical Formulation

The proposed short-term decision-making model for an electricity retailer is presented as follows:

$$\text{Minimize} \sum_{\omega=1}^{\Omega}\sum_{t=1}^{T}\pi_{\omega}\left[P_{t,\omega}^{DA}\lambda_{t,\omega}^{DA} - P_{t,\omega}^{RT}\lambda_{t,\omega}^{RT} - \left(\lambda_{t,\omega}^{DA} - \lambda_{t,\omega}^{RT}\right)P_{t,\omega}^{VI} - \left(\lambda_{t,\omega}^{RT} - \lambda_{t,\omega}^{DA}\right)P_{t,\omega}^{VD}\right] + \beta\left(\zeta - \frac{1}{1-\alpha}\sum_{\omega=1}^{\Omega}\pi_{\omega}\eta_{\omega}\right) \quad (4.2)$$

Subject to:

$$P_{t,\omega}^{DA} - P_{t,\omega}^{RT} + P_{t,\omega}^{RE} + P_{t,\omega}^{ST-} - P_{t,\omega}^{ST+} = P_{t,\omega}^{N} \quad (4.3)$$

$$0 \le P_{t,\omega}^{VI} \le P^{V_{max}}; \qquad \forall t,\omega \quad (4.4)$$

$$0 \le P_{t,\omega}^{VD} \le P^{V_{max}}; \qquad \forall t,\omega \quad (4.5)$$

$$P_{t,\omega}^{DA} = P_{t,\omega'}^{DA}; \quad \forall t,\omega,\omega' : \lambda_{t,\omega}^{DA} = \lambda_{t,\omega'}^{DA} \quad (4.6)$$

$$P_{t,\omega}^{VI} = P_{t,\omega'}^{VI}; \quad \forall t,\omega,\omega' : \lambda_{t,\omega}^{DA} = \lambda_{t,\omega'}^{DA} \quad (4.7)$$

$$P_{t,\omega}^{VD} = P_{t,\omega'}^{VD}; \quad \forall t,\omega,\omega' : \lambda_{t,\omega}^{DA} = \lambda_{t,\omega'}^{DA} \quad (4.8)$$

$$\left(\lambda_{t,\omega}^{DA} - \lambda_{t,\omega'}^{DA}\right)\left(P_{t,\omega}^{DA} - P_{t,\omega'}^{DA}\right) \le 0; \quad \forall t,\omega \quad (4.9)$$

$$\left(\lambda_{t,\omega}^{DA} - \lambda_{t,\omega'}^{DA}\right)\left(P_{t,\omega}^{VD} - P_{t,\omega'}^{VD}\right) \le 0; \quad \forall t,\omega \quad (4.10)$$

$$\left(\lambda_{t,\omega}^{DA} - \lambda_{t,\omega'}^{DA}\right)\left(P_{t,\omega}^{VI} - P_{t,\omega'}^{VI}\right) \ge 0; \quad \forall t,\omega \quad (4.11)$$

$$\sum_{\omega=1}^{\Omega} P_{t,\omega}^{VI} \le M_t z_t; \qquad \forall t \quad (4.12)$$

$$\sum_{\omega=1}^{\Omega} P_{t,\omega}^{VD} \le M_t(1-z_t); \qquad \forall t \quad (4.13)$$

$$z_t \in \{0,1\}; \qquad \forall t \quad (4.14)$$

$$E_{t,\omega} = E_{t-1,\omega} + \gamma_t P_{t,\omega}^{ST+} - \left(\frac{1}{\gamma_t}P_{t,\omega}^{ST-}\right); \forall t,\omega \quad (4.15)$$

$$E^{min} \le E_{t,\omega} \le E^{max} \qquad \forall t,\omega \quad (4.16)$$

$$E_{1,\omega} = E_{24,\omega} \quad \forall \omega \tag{4.17}$$

$$0 \le P_{t,\omega}^{ST+} \le \overline{P_{t,\omega}^{ST+}} u_{t,\omega}^{ST} \quad \forall t, \omega \tag{4.18}$$

$$0 \le P_{t,\omega}^{ST-} \le \overline{P_{t,\omega}^{ST-}} \left(1 - u_{t,\omega}^{ST}\right) \quad \forall t, \omega \tag{4.19}$$

$$P_{t,\omega}^{DA}, \eta_{\omega} \ge 0 \quad \forall t, \omega \tag{4.20}$$

$$\zeta - \sum_{t=1}^{T} [P_{t,\omega}^{N} \lambda_t^{R} + P_{t,\omega}^{RT} \lambda_{t,\omega}^{RT} - P_{t,\omega}^{DA} \lambda_{t,\omega}^{DA} + \left(\lambda_{t,\omega}^{DA} - \lambda_{t,\omega}^{RT}\right) P_{t,\omega}^{VI} + \left(\lambda_{t,\omega}^{RT} - \lambda_{t,\omega}^{DA}\right) P_{t,\omega}^{VD}] \le \eta_{\omega}; \quad \forall \omega \tag{4.21}$$

The objective function (4.2) to be minimized is comprised of two terms: 1) the expected retailer's procurement cost (i.e., the costs from purchasing power in the day-ahead and real-time markets minus the revenues obtained in the real-time market from positive energy deviations, and the revenues from virtual bidding participation); and 2) the retailer's CVaR multiplied by its risk-aversion level β. All renewable energy units are assumed to operate with zero marginal cost. Constraint (4.3) represents the retailer's energy balance. It ensures that the total available energy (i.e., the net energy purchased in the wholesale market along with the self-production of renewable energy and available stored energy) is equal to the demand of retail customers at each time and scenario. Constraints (4.4) and (4.5) limit the incremental and decremental virtual bidding capacities, respectively. Constraints (4.6)-(4.8) ensure the same power and virtual bidding capacities in the scenarios with the same DA prices. Constraints (4.9) and (4.10) enforce a decreasing bidding curve for power and decremental virtual bidding trading in the DA market, respectively. Constraint (4.11) enforce an increasing curve for incremental virtual bidding. In the electricity market considered, the retailer is allowed to submit either an incremental or decremental virtual bidding curve for each hour of the operating day as ensured by Constraints (4.12)-(4.14). Note that M_t is a sufficiently large constant and z_t is an auxiliary binary variable. The BESS constraints are formulated in (4.15)-(4.19). More specifically, Constraint (4.15) determines the state-of-charge of the BESS which is limited by its minimum and maximum values in (4.16). Constraint (4.17) ensures that the final state of charge (SOC) at the end of the operation day is equal to the SOC at the beginning of the operating day for the next-day use. Constraints (4.18) and (4.19) represent the charging and discharging power limits of the BESS, respectively. Note that the binary variable $u_{t,\omega}^{ST}$ is introduced to enforce that the BESS is not charged and discharged at the same time. Constraint (4.20) constitutes non-negative variable declarations. Finally, Constraint (4.21) is used to compute the CVaR.

4.3.5 Case Studies

The effectiveness of the proposed model is illustrated through case studies with real-world data. An electricity retailer with self-production of solar energy and BESS in the PJM market is considered. The solar power capacity is assumed to be 50 MW and a 2MW/10MWh BESS with a conversion efficiency of 0.94 is considered. The scenarios related to day- ahead and real-time prices and customers' load are generated based on PJM historical data [125]. The scenarios related

to the solar power production are generated based on historical data from the National Renewable Energy Laboratory (NREL) website [126]. Initially, 500 scenarios were generated for each stochastic variable using a SARIMA model in the MATLAB econometrics toolbox [127]. Then, the original scenarios of day-ahead prices, real-time prices, solar power production, and customers' load were reduced to 5, 5, 5, and 3, respectively, resulting in a total of (5)3(3) = 375 scenarios. Figure 4.5 illustrates the scenario arrangement considered in the case studies. Each period t corresponds to one hour such that the total planning horizon T comprises an entire day (i.e., 24 hours). The expected values of all uncertain variables at each hour of the planning horizon are shown in Figure 4.6. The proposed optimization model is modeled using Yalmip [128] and solved with Gurorbi 9.0 in MATLAB.

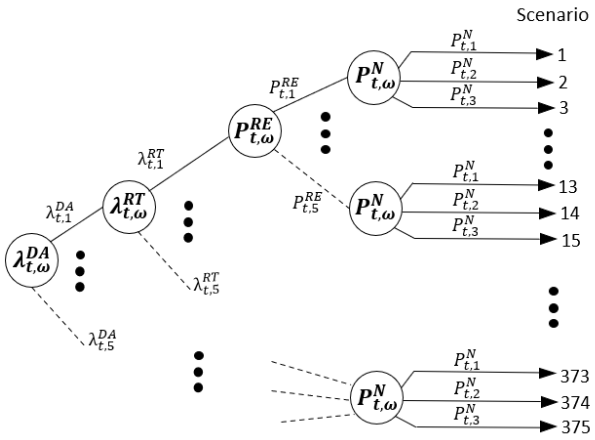

Figure 4.5 Scenario arrangement considered.

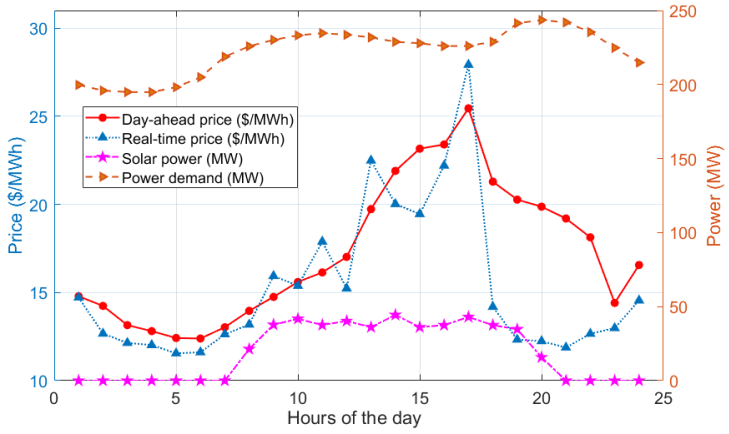

Figure 4.6 Expected values of the uncertain variables at each hour of the planning horizon.

Initially, the virtual bidding capacity is set to 30 MW and the confidence level is α = 0.95. Figure 4.7 shows the retailer's expected cost versus the CVaR for different risk-aversion levels β from 0.1 to 0.9. It turns out that, as the risk aversion increases, the expected cost also increases and the CVaR decreases. From $\beta = 0.1$ to $\beta = 0.9$, the expected cost increased nearly 10% and the CVaR

increased about 8%. In order to study the impact of considering BESS and different virtual bidding capacities on the proposed model, the retailer's reduced costs and CVaRs for different risk-aversion levels are shown in Figure 4.8 and Figure 4.9, respectively. It turns out that, the retailer's reduced costs and CVaRs are higher for larger virtual bidding capacities and are both very sensitive to the risk-aversion level. As β increases, the reduced costs decrease and the reduced CVaRs increase significantly. For a virtual bidding capacity of 60 MW, for example, the cost reduction varied from \$6,000 to approximately \$4,000 (i.e., 33%) and the CVaR reduction varied from approximately \$480 to \$4000 (i.e., 733%). It turns out that the integration of BESS also contributed to the reduction of the retailer's cost and CVaR, but with a lower sensitivity to the risk-aversion level.

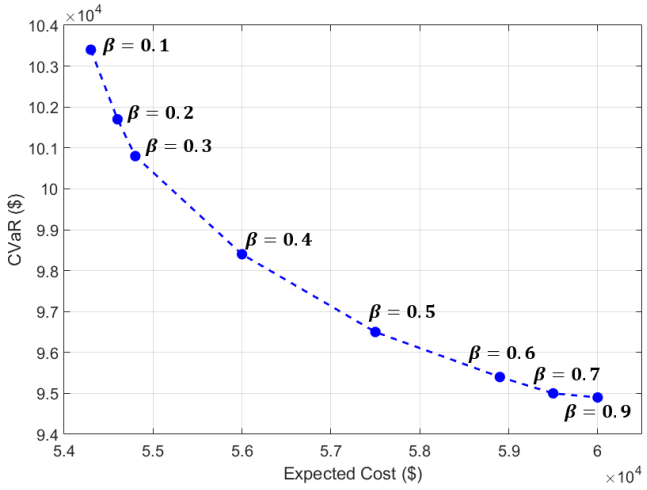

Figure 4.7 Expected cost versus CVaR.

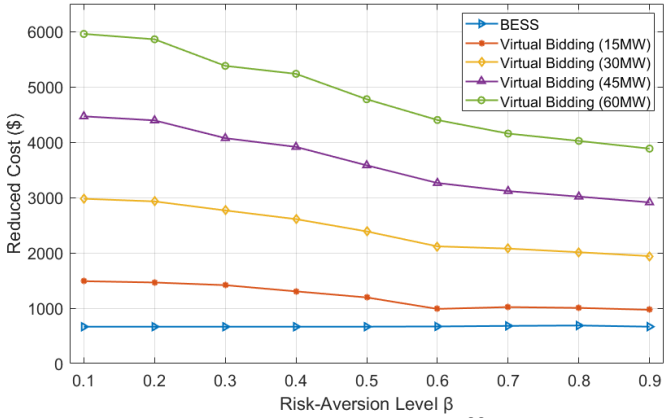

Figure 4.8 Reduced costs considering BESS and different virtual bidding capacities.

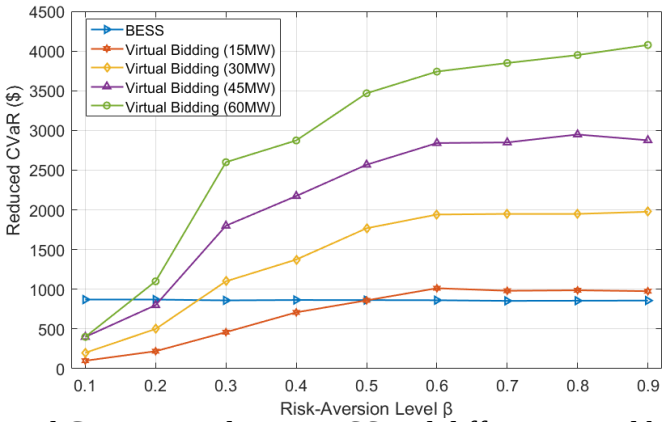

Figure 4.9 Reduced CVaR considering BESS and different virtual bidding capacities.

The hourly bidding curves are studied for hours 13 and 23 whose price scenarios are shown in Table 4.1. The virtual bidding capacity is kept at 30 MW. Initially, the hour 13 is selected and analyzed. In this hour, the expected day-ahead market price is $19.73/MWh, and the expected real-time market price is $22.50/MWh. The retailer's power bidding and virtual bidding curves generated with the proposed model for a risk-neutral and a risk-averse retailer are shown in Figure 4.10. In this hour, a decremental virtual bidding curve is submitted to the wholesale market since the expected day-ahead market price is lower than the expected real-time market price. Therefore, the retailer purchases power in the day-ahead market to resell it at a higher price in the real-time market. For β=0.3, the retailer is willing to purchase power in the day-ahead market for all price scenarios, except for the highest price scenario (i.e., $27.98/MWh). For β=0.9, the model generates a vertical power bidding curve and a vertical virtual bidding curve.

Table 4.1 Day-ahead and real-time price scenarios

	Hour	**1**	**2**	**3**	**4**	**5**
DA price scenarios	13	7.72	20.47	21.56	23.17	27.98
RT price scenarios	13	15.49	18.41	23.90	25.63	30.21
DA price scenarios	23	2.17	15.17	16.28	17.92	22.82
RT price probability	23	5.97	8.90	14.39	16.13	20.71

DA: Day-ahead; RT: Real-time.

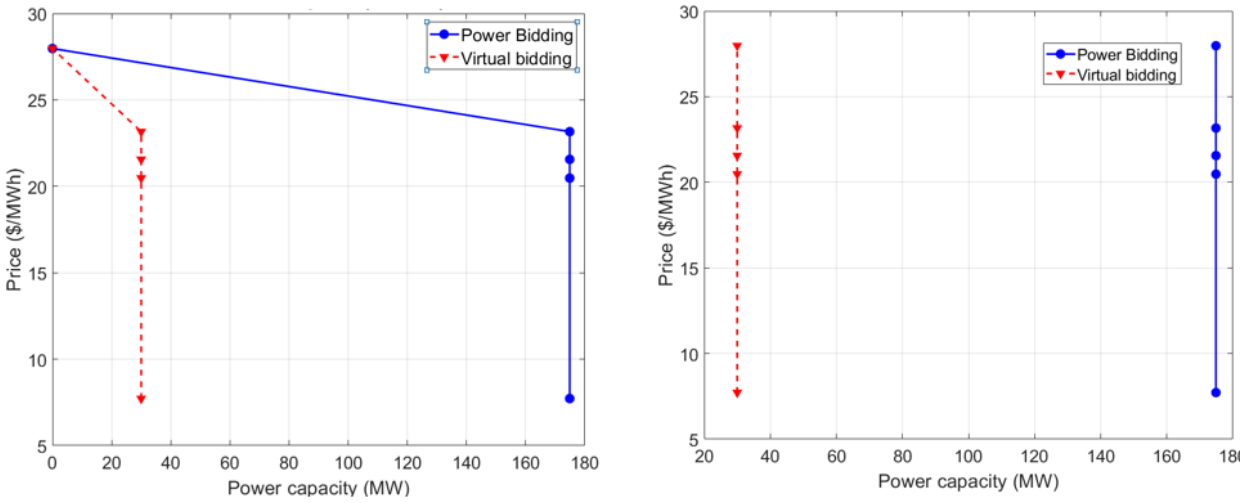

(a) β=0.3 (b) β=0.9

Figure 4.10 Power and virtual bidding curves at hour 13 for β=0.3 and β=0.9.

In the hour 23, the expected day-ahead market price is \$14.41/MWh, and the expected real-time market price is \$12.99/MWh. The retailer's power bidding and virtual bidding curves generated with the proposed model are shown in Figure 4.11. In this hour, an incremental virtual bidding curve is submitted to the wholesale market since the expected day-ahead market price is higher than the expected real-time market price. Therefore, the retailer purchases power in the real-time market to resell it at a higher price in the day-ahead market. For β=0.3, the retailer is less willing to purchase power in the day-ahead market for most price scenarios. A risk-averse retailer with β=0.9 purchases power in the day-ahead market at lower prices and sells power in the day-ahead market through incremental virtual bidding only at the highest price scenario.

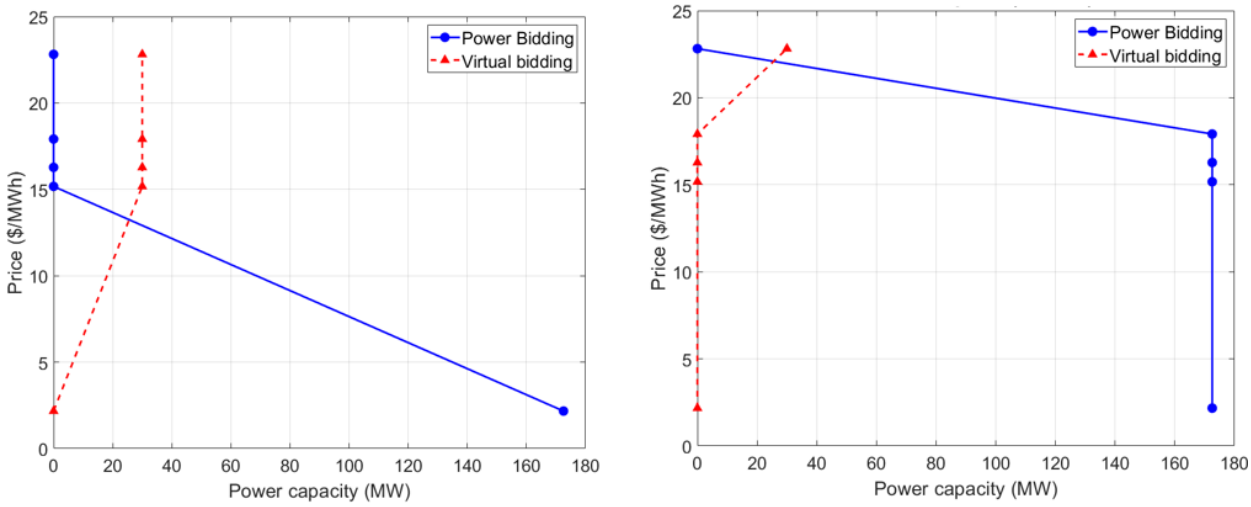

(a) β=0.3 (b) β=0.9

Figure 4.11 Power and virtual bidding curves at hour 23 for β=0.3 and β=0.9.

4.4 Conclusions and Future Work

In this chapter, a conceptual framework to integrate BESSs in both retail and wholesale markets was presented and discussed. Then, a short-term decision model for an electricity retailer with BESS and virtual bidding was proposed and studied. Case studies have shown that the integration of BESS in the retailer's decision model results in lower expected costs and CVaR values for different risk-aversion levels. Further research will be conducted to investigate the risk-management of the retailer's cost and the virtual bidding profits as separate risk portfolios.

5. Predicting Real-Time Locational Marginal Prices: A GAN- Based Approach

5.1 Introduction

Locational marginal price (LMP) prediction is critical for energy market participants to develop optimal bidding strategies and maximize their profits. However, the increasing integration of renewable resources leads to high uncertainties in both electricity supply and demand, which then increases price volatility in electricity markets and makes LMP prediction difficult for market participants.

To mitigate price volatility, LMPs in US electricity markets are settled twice in the day-ahead (DA) and real-time (RT) markets. As a spot market, the RT market experiences higher price volatility compared to the DA market (which is a forward market) [46]. Therefore, real-time LMPs (RTLMPs) are less predictable compared to day-ahead LMPs (DALMPs).

For a fixed real-time electricity market, the RTLMP uncertainties are caused both by the demand uncertainties and supply uncertainties. In the following subsections we demonstrate these uncertainties by outlining the basic concepts of LMPs with the DC optimal power flow (DCOPF) formulation.

5.1.1 Spatio-temporal Correlations and Uncertainties of LMPs

LMPs are dual variables derived from solving the optimal power flow problem. In general, a DCOPF [47, 48] is widely used by system operators to calculate LMPs, which can be formulated as the following optimization problem:

$$\min_{\mathbf{P}} \sum_{i=1}^{N} a_i P_i^2 + b_i P_i + c_i \tag{5.1a}$$

$$s.t. \quad \sum_{i=1}^{N} P_i - \sum_{i=1}^{N} L_i = 0 : \lambda \tag{5.1b}$$

$$\boldsymbol{P}^- \leq \boldsymbol{P} \leq \boldsymbol{P}^+ : \boldsymbol{\sigma}^-, \boldsymbol{\sigma}^+ \tag{5.1c}$$

$$\boldsymbol{F}^- \leq \boldsymbol{T}(\boldsymbol{P} - \boldsymbol{L}) \leq \boldsymbol{F}^+ : \boldsymbol{\mu}^-, \boldsymbol{\mu}^+ \tag{5.1d}$$

where **P, L** are the vectors of active power generations and loads at N buses, respectively. P_i, L_i are i^{th} elements in **P** and **L**, respectively. $\mathbf{P}^-$, $\mathbf{P}^+$, $\mathbf{F}^-$ and $\mathbf{F}^+$ are the vectors of upper and lower limits for power generations P and transmission line flows $\mathbf{F} = \mathbf{T}(\mathbf{P} - \mathbf{L})$, respectively. **T** is the power transfer distribution factor (PTDF) matrix. λ, $\boldsymbol{\sigma}^-$, $\boldsymbol{\sigma}^+$, $\boldsymbol{\mu}^-$ and $\boldsymbol{\mu}^+$ are the Lagrange multipliers of the corresponding constraints. For each generation cost function $C_i = a_i P_i^2 + b_i P_i + c_i$, a_i, b_i and $c_i \in \mathbb{R}$ are the generation bidding variables submitted by the generator owner at bus i. These generation bidding variables may vary frequently, instead of being constant.

In (5.1d), with the PTDF matrix **T** commonly used in commercial DCOPF software, the active power flows over transmission lines are represented as a linear combination of nodal power injections. The PTDF matrix **T** describes this linear mapping, and can be written as [47]:

$$\mathbf{T} = \left[\mathbf{0DAB^{-1}}\right] \tag{5.2}$$

where matrices **D, A, B** describe power grid topological and physical properties [47]. Given this DCOPF formulation, the vector of nodal LMPs, **LMP**, can be represented as [47]:

$$\mathbf{LMP} = \frac{\partial \mathcal{L}}{\partial \mathbf{L}} = \lambda \mathbf{1} + \mathbf{T}^{T}(\boldsymbol{\mu}^{-} - \boldsymbol{\mu}^{+}) \tag{5.3}$$

where $\frac{\partial \mathcal{L}}{\partial \mathbf{L}}$ is the partial derivative of the DCOPF's Lagrangian function $\mathcal{L}$. Assuming constant grid topology and physical properties in T, LMPs are the linear combination of Lagrange multipliers λ, $\boldsymbol{\mu}^{-}$ and $\boldsymbol{\mu}^{+}$. λ is associated with the supply-demand equality constraint in (5.1b). $\boldsymbol{\mu}^{+}$ and $\boldsymbol{\mu}^{-}$ are associated with line flow limit constraints in (5.1d). It is clear that λ is determined by the total load $\sum_{i=1}^{n} L$ and the bidding variables submitted by generators spatially dispersed across the grid. Given total load $\sum_{i=1}^{n} L$, $\boldsymbol{\mu}^{+}$ and $\boldsymbol{\mu}^{-}$ are determined by geographical distributions of loads across the grid. Therefore, LMPs across the grid are spatially correlated through the PTDF matrix, and temporally correlated through hourly load/generation variations. The spatio-temporal uncertainties in both demands and supplies will lead to LMP uncertainties.

Intuitively, accurate LMP predictions should capture these spatio-temporal uncertainties of supplies and demands, and should represent the spatial-temporal correlations among LMPs at different nodes. Thus, given a set of spatio-temporal correlated historical market data, the key point of LMP prediction is to study the conditional probability of future LMPs. The objective of the LMP predictor is to generate forecasted LMPs, which can maximize this conditional probability.

5.1.2 Related Literature and Main Contributions

Existing works predict LMPs either from system operators' perspective (assuming the predictor having system physical models) or from market participants' perspective (assuming the predictor having only public historical market data).

In [49–51], simulation-based methods, multiparametric programming approaches and neural network models are proposed to predict LMPs from system operators' perspective. These methods assume perfect knowledge of system models, such as system topology and physical properties described in PTDF matrix T, which is not shared with market participants. Without the confidential system models, predicting RTLMPs from market participants' perspective is much more challenging. In this chapter, we focus on RTLMP prediction from market participants' perspective.

Without access to any physical knowledge of energy market modeling, statistical and data-driven methods are common and practical for market participants to predict LMPs. In [14, 15, 52], data-driven LMP prediction algorithms are developed based on the concept of system pattern regions (SPRs) [14]. These algorithms do not require detailed information on system operating conditions

and network models. In [15], a support vector machine (SVM) is trained using historical market data to learn the SRPs which represent the relationship between LMPs and system loading conditions. However, this method only predicts future LMP ranges instead of exact LMP values. Moreover, one significant weakness of SPR-based methods is that the SRPs are derived by assuming fixed generation costs. The SPRs do not hold once generation bidding variables are changed. Actually, when a_i, b_i and c_i change in (5.1a), the marginal energy price λ in (5.3) may be different for the same set of nodal loads. Therefore, previous SPRs do not hold anymore. Indeed, this method is tested in simulated markets without any generation offer variations.

From the market participants' perspective, some LMP predictors focus on recovering grid models using historical market data [47]. These methods estimate parameters of the DCOPF models and try to capture the underlying market structure described by the DCOPF problem. Reference [1] developed a holistic approach to forecast wholesale energy market prices using only public market data. The approach proposed in [1] also utilizes theoretical concept of SPR [48] and learns the relationship between generation mix and zonal demand on one hand and RTLMPs on the other hand, based on the identified grid operating regimes. Both SPRs and the identification of grid operating regimes assume no variation of generation bids in DCOPF. However, grid operating regimes are not fixed in real-world systems. The DCOPF-related methods are computationally expensive. Moreover, their LMP prediction accuracy is highly dependent on the accuracy of the estimated DCOPF model parameters under fixed operating conditions, which could not be guaranteed for real-world systems with a large number of time-varying model parameters under changing operating conditions.

Another group of methods predict LMPs by learning the linear or nonlinear relationship between historical LMPs and uncertain demands. In [53, 54], time-series statistical methods, such as ARMAX model [53] and ARIMA model [54], are developed to learn such linear relationship. In [55–57], data-driven machine learning approaches, such as neural network methods [55], tree-based regression models [57] and LASSO method [56], are applied to learn such nonlinear relationship. In [58], a feature selection technique is proposed to improve the accuracy of short term price forecasting for neural network-based prediction models. In [57, 59, 60], multi neural network-based models are implemented in price forecasting. The combinatorial neural network [59] is trained by a stochastic search method and a sliding window is used to incorporate previous predicted values for multi-period forecast. References [57, 60] focus on forecasting components of LMPs. The final LMP prediction includes individual predicted energy price, congestion price and loss price. These methods mainly capture the temporal correlations between LMPs and demands, without considering the spatial correlations among system-wide LMPs. In [61], a new electricity market- clearing mechanism is proposed based on the uncertainty contained LMP (U-LMP). Besides regular components, U-LMP includes two new spatial uncertainty components.

Multivariate modeling is a popular spatio-temporal correlation analysis method. In [62], a multi-variate LASSO model is deployed to study the electricity prices of eleven European datasets. This method focuses only on the statistical relationship among prices, ignoring the actual uncertainties of loads and supply bids. In our previous work [63], a data-driven method is proposed to forecast RTLMPs using only historical RTLMP data. A generative adversarial network [64] (GAN) is applied to learn spatio-temporal correlations among historical RTLMPs. However, the underlying correlations caused by supply and demand uncertainties are ignored in this work.

5.1.2.1 Challenges and Contributions

Several challenges remain unexplored in existing works for data-driven LMP forecasts from market participants' perspective. 1) Spatio-temporal uncertainties of both demands and supplies (including generator bidding uncertainties) have strong correlations with the LMP uncertainties and should be captured to improve LMP prediction accuracy. These uncertainties and correlations are not fully utilized in developing LMP predictors. Existing works either ignore spatial correlations among the uncertainties of demands, supplies, and LMPs [53, 55, 56], or assume no variation/uncertainty for the generator bids in their LMP predictors [14, 15, 52]. 2) The ignorance of certain correlations and uncertainties in these market data leads to frequent prediction model updates in some existing works [55, 57], in order to maintain high LMP prediction accuracy. Accurate LMP predictors without the need of frequent model updates are more desirable in practical applications for reduced computational burden. 3) Existing approaches only focus on special types of price forecasting problems (such as day-ahead forecasts of DALMPs [55, 62] or RTLMPs [1], hour-ahead forecasts of RTLMPs [15, 52], etc.). A general LMP predictor which performs well across different types of price forecasting problems is more widely applicable than these specialized predictors, as it could be adopted by various market participants with different price forecasting needs.

To overcome the above challenges, we propose a purely data-driven approach for predicting system- wide RTLMPs and DALMPs by learning spatio-temporal correlations among heterogeneous public market data, without requiring any confidential information on system topology, model parameters, or market operating details. In this chapter, we make the following contributions:

- We introduce a general data structure which enables efficient storage and organization of spatio-temporally correlated system-wide heterogeneous market data streams (i.e., LMPs, loads, generation offers, generation mix data, etc.) into the format of 3-dimensional (3D) tensors. This general data structure can be integrated into various LMP predictors to better capture spatio-temporal correlations among system-wide demands, supplies, and LMPs.
- We formulate the RTLMP prediction problem as a 2-dimensional (2D) array prediction prob- lem. A conditional generative adversarial network (GAN) based prediction model is trained with multiple loss functions to learn the spatio-temporal correlations among historical mar- ket data. The discriminator model and adversarial training procedure are taken to eliminate blurry predictions. This model is applied to predict hourly system-wide RTLMPs, using only public market data. To our best knowledge, this is the first attempt toward applying conditional GANs for power system spatio-temporal data forecasts, rather than simply for synthetic power system data generations [12, 13].
- An auto-regressive moving average (ARMA) based online calibration method is proposed to solve the prediction deviations caused by generation bidding uncertainties without frequent updates to the GAN-based prediction model. To our best knowledge, this is the first study incorporating generation bidding uncertainties to the prediction and analysis of energy market data.
- The proposed LMP prediction approach is generalizable toward various types of price forecasting problems. Case studies on real-world market data verify the prediction

accuracy of this approach for RTLMP and DALMP forecasts in both day-ahead and hour-ahead manner, when only annual GAN model update is required.

Although the proposed approach is applied to system-wide LMP prediction, the prediction method and the 3D tensor data structure can be generalized to system-wide load and renewable generation prediction problems. The LMP prediction problem is more challenging than the other two problems, as uncertainties from both loads and generations could reduce prediction accuracy [14, 15]. The system-wide LMP predictor (which is a general predictor for LMPs at multiple locations) can also be easily adjusted to predict LMPs at several nodes over certain sub-areas in a system. This enhances the LMP prediction for generator owners and load serving entities who buy/sell energy at these nodes/sub-areas, as well as market participants in the purely financial instruments of electricity market (such as financial transmission rights) who cares about the spatial LMP differences among different nodes.

5.2 Problem Formulation

This section introduces a general data structure to organize system-wide spatio-temporal correlated market data into a 3D tensor. The historical market data tensor stores spatio-temporal correlations among system-wide RTLMPs. The next time step RTLMP prediction problem is then formulated as a problem of generating a future 2D array, given a historical 3D tensor.

In this work, the spatial correlation among market data is defined as a combination of 1) the spatial gradient of the market data (i.e., rate of change of the data with respect to the position coordinates in the market data 2D array) and 2) the difference between the positive/negative changing directions over time for the prices collected at different locations (price nodes). The spatial correlation and temporal correlation (temporal coherency between predicted LMPs and historical ground-truth LMPs) are quantified by the corresponding loss/distance functions introduced in this section. To evaluate the learning of spatial correlations defined above, three spatial correlation metrics are adopted/defined in case studies.

5.2.1 The Public Market Data

The publicly available market data depends on specific markets. Most energy markets publish nodal, zonal and system-level hourly RTLMPs and DALMPs. Other public market data commonly includes demand data and generation mix data. As shown in (5.3), system-wide RTLMPs are spatially correlated based on PTDF matrix $\boldsymbol{T}$. Even though the explicit $\boldsymbol{T}$ is confidential and unknown to market participants, the implicit spatial correlations can be learned from DALMPs. Because DALMPs are published just one day before the operating day, changes in system topology and properties after publishing DALMPs would be limited. Therefore, to predict RTLMPs, the pre-published DALMPs should be taken as input data.

In (5.3), the marginal energy price λ is determined by the total system supply-demand balance. The historical total demand is also an available input parameter in the model. The geographical distribution of loads is a key factor for determining congestion prices μ. Therefore, the nodal orzonal demand data should be included as inputs depending on their availability.

In most electricity markets, system-wide generation offer details are published with significant delays, and therefore cannot be fully utilized by market participants in their price prediction. The generation percentages of certain generation types over total system generation (i.e., the generation mix data) are highly correlated with RTLMPs. We adopt historical hourly generation mix data that is publicly available in some markets (such as SPP [65]) in training our GAN model.

5.2.2 Historical Market Data Tensor

Consider a set of publicly available historical hourly market data collected from $N = h \times w$ different price nodes (locations) for T consecutive hours. There are M types of historical market data for each price location (i.e., the RTLMPs, the DALMPs, the local demand, the distributed energy resources outputs, etc.). All these locational market data can be organized into a 3D tensor as shown in Figure 5.1.

Definition 1. *Let $x_{i,j}^{t}$ represent a historical market data point collected from k^{th} price node at time t, where $k = h \times (i-1) + j$, $k \in [1, N]$. This market data point includes M channels. For example, when $M = 3$, $x_{i,j}^{t} = \{x_{i,j}^{t-rtlmp}, x_{i,j}^{t-dalmp}, x_{i,j}^{t-demand}\}$ with the RTLMP, DALMP, and demand data channels, respectively.*

Definition 2. *At each time t, N historical market data points collected over the market are arranged into a 2D array $X^t \in \mathbb{R}^{h \times w}$. The positions of each market data point in the 2D array are fixed and determined according to their geographical location in the electricity market footprint.*

Definition 3. *Let a 3D tensor $\mathcal{X} \in \mathbb{R}^{h \times w \times T}$ represent the set of publicly available historical hourly market data. This tensor $\mathcal{X}$ is comprised of T 2D arrays X^t, where $t \in [1, T]$.*

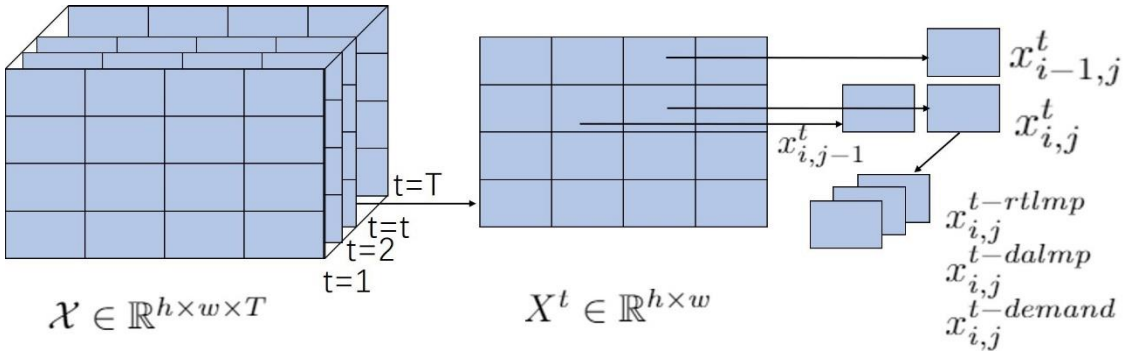

Figure 5.1 Historical market data structure.

As shown from right to left in Figure 5.1, different types of market data collected from the same location at one time step are organized into one historical market data point with different data channels. Then, the historical market data points of all locations at the same time step are organized into one 2D array. Finally, a series of time-stamped 2D arrays are organized into a 3D tensor. The above definitions introduce a general market data structure to conveniently store the spatio-temporal correlations among historical market data in the inter-dependencies along multiple

dimensions of the 3D tensor. For example, the correlations among different positions in one 2D array X^t, such as $x_{i-1,j}^t$, $x_{i,j}^t$ and $x_{i,j-1}^t$, represent spatial correlations among historical market data collected from different price nodes (locations) at time t; the correlations among the same positions obtained at different times, such as $x_{i,j}^{t-1}$, $x_{i,j}^t$, $x_{i,j}^{t+1}$, represent temporal correlations among historical market data collected from the same price node (location) at different hours.

In **Definition 2**, each 2D array consists of market data collected at one time (hour). Therefore, the third dimension of the tensor in **Definition 3** represents hours. It can also be modified to represent days. Consider the same set of publicly available historical hourly market data collected from $N = h \times w$ price nodes (locations) for D days. Within each day, we have 24 consecutive 2D arrays (X^1 to X^{24}) as defined in **Definition** 2. They can be reorganized into an enlarged 2D array $X_{Day}^d \in \mathbb{R}^{4h\times 6w}$, where $d \in [1, D]$. In this way, the hourly tensor $\mathcal{X}$ is reshaped to a daily tensor $\mathcal{X}_{Day} \in \mathbb{R}^{4h\times 6w\times D}$, as shown in Figure 5.2. In this daily tensor, the spatio-temporal correlations among hourly market data within the same day are stored in each day's 2D array X_{Day}^d. The daily market pattern is represented by the correlations among different daily 2D arrays in one daily 3D tensor.

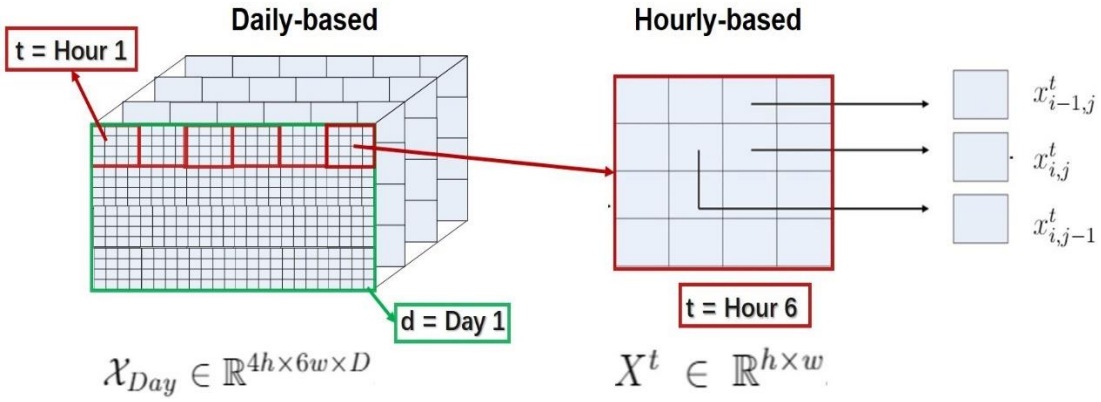

Figure 5.2: The daily tensor structure reshaped from hourly tensor.

The daily and hourly tensor structures can be adopted to perform day-ahead and hour-ahead predictions of system-wide LMPs, respectively. In the rest of this chapter, due to space limitations, the hourly tensor structure in **Definition 3** is mainly used to present the prediction approach. In our case studies, both hourly and daily tensor structures are utilized in developing the hour-ahead and day-ahead LMP predictors.

5.2.3 Normalization of Historical Market Data

Because each data point in tensor $\mathcal{X}$ contains M channels. The units and scales of these M channels are different. Even for the same channel, the statistics of historical market data may differ year by year. Therefore, all historical data are preprocessed to the range of -1 and 1 by normalization.

After organizing historical locational market data into tensor $\mathcal{X}$, each value $x_{i,j}^{t-ch}$ of the channel ch is normalized as:

$$x_{i,j}^{t-ch^{norm}} = \frac{ln\left(x_{i,j}^{t-ch^{+}}\right) - ln\left(max\left(\mathcal{X}^{ch^{+}}\right)\right)/2}{ln\left(max\left(\mathcal{X}^{ch^{+}}\right)\right)/2} \tag{5.4}$$

where

$$x_{i,j}^{t-ch^{+}} = x_{i,j}^{t-ch} - min(\mathcal{X}^{ch}) + 1 \tag{5.5}$$

$$\mathcal{X}^{ch^{+}} = \{X^{1-ch^{+}}, \cdots, X^{t-ch^{+}} \cdots, X^{T-ch^{+}}\} \tag{5.6}$$

where $x_{i,j}^{t-ch^{norm}}$ is the normalized value of $x_{i,j}^{t-ch}$ in channel ch; $x_{i,j}^{t-ch^{+}}$ denotes $(i,j)^{th}$ element of $X^{t-ch^{+}}$; $X^{t-ch^{+}}$ is t^{th} 2D array in tensor $\mathcal{X}^{ch^{+}}$; $\mathcal{X}^{ch}$ is the channel ch of tensor $\mathcal{X}$; $max\left(\mathcal{X}^{ch^{+}}\right)$ is the largest element in $\mathcal{X}^{ch+}$; $min(\mathcal{X}^{ch})$ is the smallest element of channel ch in tensor $\mathcal{X}$. After normalization, values in the normalized tensor $\mathcal{X}^{norm}$, such as normalized prices and demands, lie within -1 and 1.

5.2.4 Formulation of The RTLMP Prediction Problem

The normalized historical market data across the system for T hours are organized into a normalized historical market data tensor $\mathcal{X}^{norm} = \{X^{1-norm}, \cdots, X^{t-norm}, \cdots, X^{T-norm}\}$. The spatio-temporal correlations among values in the RTLMP channel are determined by the unknown PTDF matrix T and uncertainties of other market data channels. Thus, a predictor should be employed to learn the implicit relationships stored in this historical market data tensor $\mathcal{X}^{norm}$ and estimate a reasonable 2D array $\hat{X}^{(T+1)-norm}$ for next time $T+1$.

The RTLMP prediction problem is formulated as a 2D array prediction problem. Given a historical market data tensor as input, the objective of a desired predictor is to generate a future 2D array $\hat{X}^{(T+1)-norm}$, such that the predicted $\hat{X}^{(T+1)-norm}$ is close to the ground truth $X^{(T+1)-norm}$. Meanwhile, spatio-temporal correlations in $\hat{\mathcal{X}}^{norm} = \{X^{1-norm}, \cdots, X^{t-norm}, \cdots, X^{T-norm}, \hat{X}^{(T+1)-norm}\}$ is similar to those in the ground truth $\mathcal{X}^{norm} = \{X^{1-norm}, \cdots, X^{t-norm}, \cdots, X^{T-norm}, X^{(T+1)-norm}\}$. This is achieved by maximizing the conditional probability $p\left(\hat{X}^{(T+1)-norm} | \mathcal{X}^{norm}\right)$ using the proposed predictor. The next section presents the necessity of learning spatio-temporal correlations in the LMP prediction problem.

5.3 GAN-Based RTLMP Prediction

Built upon the above 2D array prediction formulation, a generative convolutional neural network (CNN) [66] is adopted as the predictor to generate forecasted RTLMPs. Another discriminative CNN is employed to assist the adversarial training of the CNN-based RTLMP predictor. The generative and discriminative CNNs, denoted by G and D respectively, form the GAN-based RTLMP prediction approach. It is inspired by the GAN-based video prediction approaches in [67-69]. Both the video prediction and the RTLMP prediction problems can be formulated as the spatio-temporal sequence data prediction problem with similar 3D tensor data structure.

In the training process, the weights in G are optimized by minimizing certain distance between generated RTLMP forecasts and the ground truth RTLMPs. However, several drawbacks arise from simply minimizing only one distance. Therefore, multiple loss terms (distance functions) are adopted.

In the following sections, $\mathcal{X} = \{X^1, \cdots, X^n\}$ denotes the input historical market data tensor with normalized values obtained from different price nodes over n consecutive time instants, $\mathcal{X} \subset \mathcal{X}^{norm}$; Y denotes the ground truth of the 2D array with normalized values at time $n+1$ (i.e., the prediction target), $Y = X^{n+1} \in \mathcal{X}^{norm}$.

5.3.1 The Generative Model G

Let $\hat{Y}$ be the generation of G for a given historical market data tensor $\mathcal{X}$, i.e., $\hat{Y} = G(\mathcal{X})$. $\hat{Y}$ is the prediction of Y. G is a generative CNN, and is trained by taking a batch of historical market data tensors as input and minimizing the distance between the output $\hat{Y}$ and ground truth Y. In the normal generative CNN approaches, the distance between the output and the ground truth is usually quantified by the p-norm distance:

$$\mathcal{L}_p(\mathcal{X}, Y) = \ell_p(G(\mathcal{X}), Y) = \|G(\mathcal{X}) - Y\|_p^p \tag{5.7}$$

where $\|\cdot\|_p$ denotes the entry-wise p-norm of a particular matrix, with $p = 1$ or $p = 2$. Euclidean distance or Manhattan distance between $\hat{Y}$ and Y is calculated when $p = 2$ or $p = 1$, respectively. During the training process, this loss function forces the generator G to generate the next-hour market data 2D array $\hat{Y}$ that is close to the corresponding ground-truth Y by minimizing the p-norm distance between Y and $\hat{Y}$.

However, predicting RTLMPs only with such normal CNN-based G has two drawbacks:

1. Using p-norm loss may lead to loss of spatial correlations. In actual energy markets, congestion only happens in limited lines. Because the PTDF matrix T in (5.3) is very sparse, most price nodes have pretty similar LMPs which are close to the marginal energy price λ. In the training process, minimizing p-norm loss over historical dataset may result in constant RTLMPs for all price nodes and loss of spatial correlations.
2. Using p-norm loss may lead to blurry predictions [68]. From (5.3) we know, even for the same PTDF matrix T and same supply-demand scenarios, LMPs will be different based on the bidding variables submitted by the generator owners. In this case, the probability distributions of LMPs are determined by the probability distributions of bidding strategies. Suppose generator owners have two equally likely strategies s_1 and s_2, with probability $p(s_1) = p(s_2)$, the corresponding LMP at one price node has two values x_{s_1} and x_{s_2} with same probabilities $p(x_{s_1}) = p(x_{s_2})$ over the data. During training process, minimizing p-norm loss over the dataset will lead to the blurry prediction $x_{avg} = (x_{s_1} + x_{s_2})/2$, even if the probability $p(x_{avg})$ is very low in historical dataset.

The problem of loss of spatial correlations can be solved by adding an additional loss term when training G. The following gradient difference loss function $\mathcal{L}_{gdl}(\mathcal{X}, Y)$ [68] is adopted to capture the spatial correlations among historical market data:

$$\mathcal{L}_{gdl}(\mathcal{X}, Y) = \mathcal{L}_{gdl}(\hat{Y}, Y) = \sum_{i,j} || \, Y_{i,j} - Y_{i-1,j}| - |\hat{Y}_{i,j} - \hat{Y}_{i-1,j}||^{\alpha} + ||Y_{i,j-1} - Y_{i,j}| - |\hat{Y}_{i,j-1} - \hat{Y}_{i,j}||^{\alpha} \tag{5.8}$$

where $\alpha \geq 1, \alpha \in \mathbb{Z}$; $Y_{i,j}$ and $\hat{Y}_{i,j}$ denote $(i,j)^{th}$ data point in the ground-truth market data 2D array Y and the generated $\hat{Y} = G(\mathcal{X})$, respectively. During the training process, this loss function forces the generator G to generate the next-hour market data $\hat{Y}$ which has similar locational gradient difference information compared to the ground-truth Y. Since the locational gradient difference information captures the spatial variations of historical market data arrays, this minimization ensures the generated market data array fully captures the spatial correlations among system-wide historical market data.

Another loss function to eliminate the loss of spatial correlation is the direction changing loss function $\mathcal{L}_{dcl}(\mathcal{X}, Y)$ [70]:

$$\mathcal{L}_{dcl}(\mathcal{X}, Y) = \sum_{i,j} | \, sgn\big(\hat{Y}_{i,j} - X^{t}_{i,j}\big) - sgn\big(Y_{i,j} - X^{t}_{i,j}\big)| \tag{5.9}$$

where $sgn(\cdot)$ is the sign function:

$$sgn(z) \quad = \begin{cases} -1 & if \; z \leq 0 \\ 0 & if \; z = 0 \\ 1 & if \; z \geq 0 \end{cases} \tag{5.10}$$

Because of the supply-demand changes and congestion changes, not all RTLMPs at different price nodes increase or decrease simultaneously. During the training process, this loss function forces the generated market data $\hat{Y}$ to correctly follow the price changing directions of the ground-truth Y by penalizing incorrect market data trend predictions over time.

5.3.2 The Discriminative Model D

The discriminator D is also a CNN model, which is incorporated in the adversarial training process to avoid blurry predictions by learning the spatio-temporal correlations among historical market data. $\{\mathcal{X}, Y\}$ is a constructed tensor including $\mathcal{X}$ and Y, representing the ground truth tensor; $\{\mathcal{X}, \hat{Y}\}$ is a constructed tensor including $\mathcal{X}$ and $\hat{Y}$, representing the generated tensor (with the generated 2D array $\hat{Y}$ concatenated after the ground-truth historical tensor $\mathcal{X}$). D takes $\{\mathcal{X}, Y\}$ or $\{\mathcal{X}, \hat{Y}\}$ as input, and outputs a scalar $D(\{\mathcal{X}, \cdot\}) \in [0,1]$ to indicate the probability of the input $\{\mathcal{X}, \cdot\}$ being the ground-truth. During training, the target of $D(\{\mathcal{X}, Y\})$ is class 1; the target of $D\big(\{\mathcal{X}, \hat{Y}\}\big)$ is class

0. D is trained by minimizing the following loss function to classify the input $\{\mathcal{X}, Y\}$ into class 1 and the input $\{\mathcal{X}, \hat{Y}\} = \{\mathcal{X}, G(\mathcal{X})\}$ into class 0 [68]:

$$\mathcal{L}_{adv}^{D}(\mathcal{X}, Y) = \mathcal{L}_{bce}(D(\{\mathcal{X}, Y\}), 1) + \mathcal{L}_{bce}\left(D\left(\{\mathcal{X}, \hat{Y}\}\right), 0\right) \tag{5.11}$$

where $\mathcal{L}_{bce}$ is the binary cross-entropy loss:

$$\mathcal{L}_{bce}(k, s) = -[slog(k) + (1 - s)log(1 - k)] \tag{5.12}$$

where $k \in [0,1]$ and $s \in \{0,1\}$. In this chapter, $s \in \{0,1\}$ represents the label for ground-truth or generated data (1 or 0), $k \in [0,1]$ represents the scalar generated from D. In the batch training process, $\mathcal{L}_{bce}(k, s)$ measures the distance between the discriminator outputs $K = D(\{\mathcal{X}, \cdot\})$ and the labels S ($S_i = 1$ and $S_i = 0$ for ground truth and generated market data, respectively). By implementing D, the blurry prediction x_{avg} should be easily classified as unrealistic prediction by D. Because in the historical dataset, $p\left(\{\mathcal{X}, \hat{Y}_{avg}\}\right)$ is very low compared to $p\left(\{\mathcal{X}, Y_{s_1}\}\right)$ and $p\left(\{\mathcal{X}, Y_{s_2}\}\right)$, where $\hat{Y}_{avg}$, Y_{s_1} and Y_{s_2} are generated market data array containing x_{avg}, and ground truth market data arrays containing x_{s_1} and x_{s_2}, respectively.

For any $D\left(\{\mathcal{X}, \hat{Y}\}\right)$ close to 0, G is penalized by the adversarial loss function $\mathcal{L}_{adv}^{G}(\mathcal{X}, Y)$ [67-69]:

$$\mathcal{L}_{adv}^{G}(\mathcal{X}, Y) \quad = \mathcal{L}_{bce}(D(\{\mathcal{X}, G(\mathcal{X})\}), 1) \tag{5.13}$$

During the training process, minimizing this adversarial loss function forces G to generate $\hat{Y}$ which is temporally coherent with the input historical market data $\mathcal{X}$ and as real as ground truth Y with high probability in historical dataset.

5.3.3 The GAN-Based RTLMP Prediction Model

The proposed GAN model consists of a generative model G and a discriminative model D as described in previous sections. Figure 5.3 shows the training procedure of the GAN model.

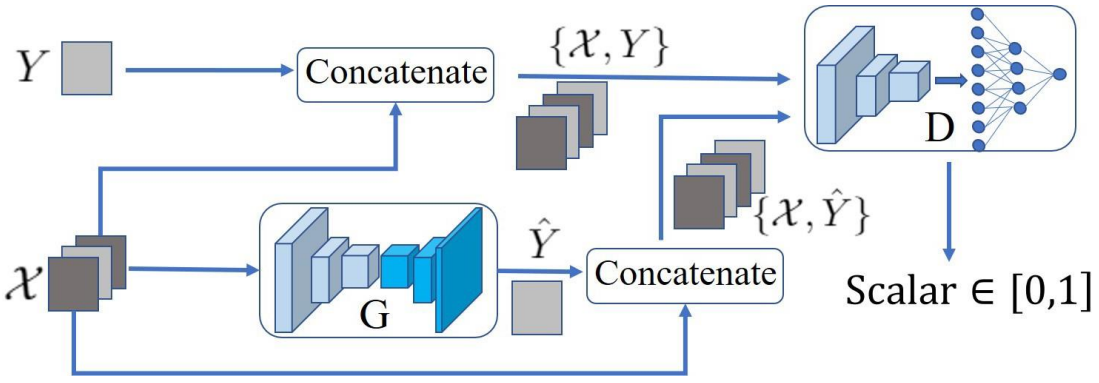

Figure 5.3 The training procedure of the GAN-based RTLMP prediction model.

During training process, D is optimized by minimizing the loss function in (5.11); G is optimized by minimizing the following multi-loss function:

$$\mathcal{L}^G(\mathcal{X},Y) = \lambda_{adv}\mathcal{L}^G_{adv}(\mathcal{X},Y) + \lambda_{\ell_p}\mathcal{L}_p(\mathcal{X},Y) + \lambda_{gdl}\mathcal{L}_{gdl}(\mathcal{X},Y) + \lambda_{dcl}\mathcal{L}_{dcl}(\mathcal{X},Y) \qquad (5.14)$$

where $\mathcal{L}^G(\mathcal{X},Y)$ denotes the weighted loss function for training G; λ_{adv}, λ_{ℓ_p}, λ_{gdl}, and λ_{dcl} denote the hyperparameters for adjusting the tradeoffs among various loss terms.

Upon training convergence, the distance between the generated market data $\hat{Y}$ and the ground-truth Y is small enough given input historical tensor $\mathcal{X}$, such that the conditional probability $p(\hat{Y}|\mathcal{X})$ is maximized by G. The discriminator D cannot differentiate between $\{\mathcal{X},Y\}$ and $\{\mathcal{X},\hat{Y}\}$ anymore.

In the above discussions, only the utilization of locational historical data in the proposed model is elaborated. However, other non-locational historical data, such as system total load, generation mix data, total distributed resources output, can also be incorporated as supplementary conditions of the proposed predictor. For example, if system operator provide accurate demand prediction, it can be incorporated to improve RTLMPs prediction accuracy. In this case, $G(\mathcal{X},\beta)$ is trained to maximize the joint conditional probability $p(\hat{Y}|\mathcal{X},\beta)$, where β encodes all available supplementary data. In the case studies, the proposed model is verified when both locational and non-locational data are utilized as inputs.

5.3.4 Adversarial Training

Algorithm 1 summarizes the adversarial training algorithm. G and D are trained simultaneously, with the weights in their neural network models, organized as weight matrices W_G and W_D, updated iteratively. The stochastic gradient descent (SGD) minimization is adopted to obtain optimal model weights. In each training iteration, a new batch of m training data samples (i.e., m historical market data tensor) are obtained for updating W_G and W_D. Upon convergence, the generator G is trained to generate $\hat{Y}$ as realistic as possible.

During training, the appropriate values of 4 hyperparameters λ_{adv}, λ_{ℓ_p}, λ_{gdl}, and λ_{dcl} are selected by the following 2-step tuning procedure:

1. *Rough selection*: The hyperparameters λ_{adv} and λ_{ℓ_p} are first determined in the rough selection step. These two hyperparameters are associated with the basic loss functions of classic GANs. Therefore, without appropriate selection of λ_{adv} and λ_{ℓ_p}, the GAN training may encounter convergence issues. In this step, λ_{ℓ_p} is set at 1; λ_{gdl}, and λ_{dcl} are set at 0; the range of λ_{adv} is set between 0 and 0.5 with a step size of 0.05. The learning rates are set as $\{0.00005, 0.0005, 0.005, 0.05, 0.5\}$. The hyperparameter λ_{adv} is selected by grid search [71].
2. *Fine-tuning*: After the rough selection step, λ_{adv}, λ_{ℓ_p} and the learning rates are fixed. Then, λ_{gdl}, and λ_{dcl} are determined by fine tuning.

The initial guess of these parameters is from [68]. The final hyperparameters are determined through the above tuning procedure to obtain the best performance.

Algorithm 1 Training generative adversarial networks for RTLMP prediction

Require: set the learning rates ρ_D and ρ_G, loss hyperparameters λ_{adv}, λ_{ℓ_p}, λ_{gdl}, λ_{dcl}, and minibatch size m

Require: initial random discriminative model weights W_D and generative model weights W_G

while not converged **do**

Update the discriminator D:

Get a batch of m data samples from the training dataset, $(\mathcal{X}, Y) = \left(\mathcal{X}^{(1)}, Y^{(1)}\right), \cdots, \left(\mathcal{X}^{(m)}, Y^{(m)}\right)$

Do one SGD update step

$$W_D = W_D - \rho_D \sum_{i=1}^{m} \frac{\partial \mathcal{L}_{adv}^{D}\left(\mathcal{X}^{(i)}, Y^{(i)}\right)}{\partial W_D}$$

Update the generator G:

Get a *new* batch of m data samples from the training dataset, $(\mathcal{X}, Y) = \left(\mathcal{X}^{(1)}, Y^{(1)}\right), \cdots, \left(\mathcal{X}^{(m)}, Y^{(m)}\right)$

Do one SGD update step

$$W_G = W_G - \rho_G \sum_{i=1}^{m} \left(\lambda_{adv} \frac{\partial \mathcal{L}_{adv}^{G}\left(\mathcal{X}^{(i)}, Y^{(i)}\right)}{\partial W_G} + \lambda_{\ell_p} \frac{\partial \mathcal{L}_{\ell_p}\left(\mathcal{X}^{(i)}, Y^{(i)}\right)}{\partial W_G} + \lambda_{gdl} \frac{\partial \mathcal{L}_{gdl}\left(\mathcal{X}^{(i)}, Y^{(i)}\right)}{\partial W_G} + \lambda_{dcl} \frac{\partial \mathcal{L}_{dcl}\left(\mathcal{X}^{(i)}, Y^{(i)}\right)}{\partial W_G} \right)$$

end while

5.4 Autoregressive Moving Average Calibration

The above GAN model is trained using year-long historical market data, and applied to predict RTLMPs hour by hour for the following year. Due to fuel price fluctuation, load growth and market participants' strategic behaviours, the market data statistics vary over years. This would cause deviations between ground-truth and predicted RTLMPs, as the generator G is trained using market data of previous years. For better prediction accuracy, the RTLMPs generated by GAN are calibrated through estimating their deviations from the ground truth:

$$\tilde{y}(i+1) = \hat{y}(i+1) + \Delta\hat{y}(i+1) \tag{5.15}$$

where

$$\Delta\hat{y}(i+1) = y(i+1) - \hat{y}(i+1) + e(i+1) \tag{5.16}$$

where $y(i+1)$, $\hat{y}(i+1)$, and $\tilde{y}(i+1)$ denote the ground-truth RTLMP, the RTLMP generated by G, and the RTLMP after calibration at time $i+1$ for a particular price node, respectively; $\Delta\hat{y}(i+1)$ denotes the estimated difference between $y(i+1)$ and $\hat{y}(i+1)$; $e(i+1)$ denotes the estimation error.

The ARMA model below is applied to estimate $\Delta\hat{y}(i+1)$:

$$\Delta\hat{y}(i+1) = \mu + \sum_{k=1}^{p} \phi_k \, \Delta\hat{y}(i-k+1) + \sum_{k=1}^{q} \theta_k \, \varepsilon(i-k+1) + \varepsilon(i+1) \tag{5.17}$$

where μ denotes the expectation of $\Delta\hat{y}(i+1)$, ϕ_k and θ_k are the autoregressive (AR) and moving average (MA) parameters of the ARMA model, respectively; $\varepsilon(i)$ represents the white noise error terms at time i; p and q denote the orders of the AR and MA terms of the ARMA model, respectively. Appropriate values of p, q, μ, ϕ_k, θ_k, and the variance of the white noise series $\varepsilon(i)$ are identified using historical data [72,73].

The overall framework of the proposed design for RTLMP prediction is shown in Figure 5.4. The proposed RTLMP prediction framework includes the following steps:

1. Data normalization and organization. Historical public data streams are organized into a time-series of 2D arrays (i.e., the 3D tensor).
2. RTLMP predictions are generated from the GAN-based predictor G for the next hour and several past hours.
3. RTLMP predictions for the next hour are calibrated through an ARMA model using generated RTLMPs and the ground truth of historical data.

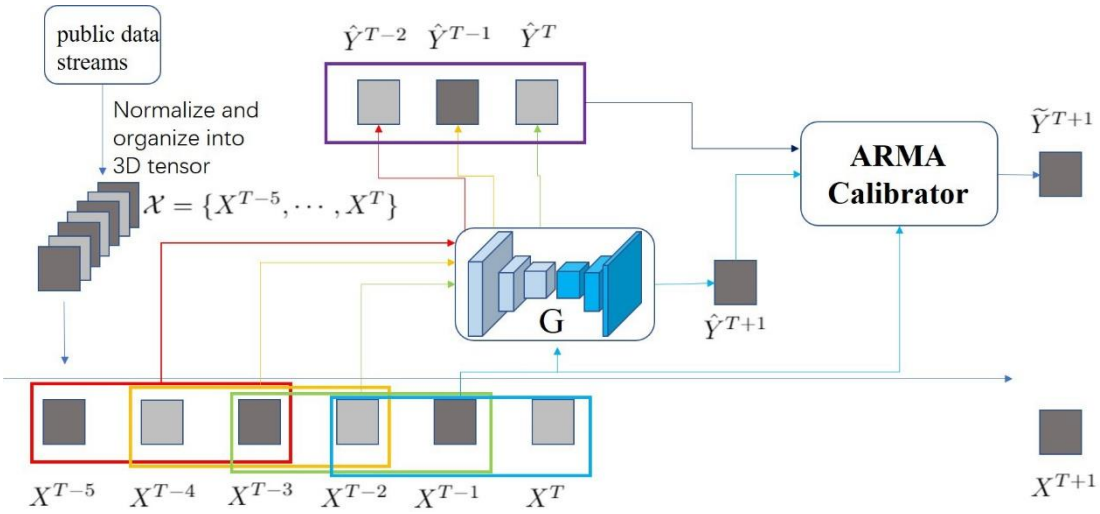

Figure 5.4 The framework of GAN-based approach with ARMA calibrator for LMP prediction.

5.5 Case Studies

The proposed RTLMP prediction method is tested using historical market data from MISO and SPP. The prediction models are implemented by TensorFlow 2.0 [74] and trained on Google Colaboratory using online GPU for acceleration. Implementation details of the GAN model are presented below.

5.5.1 Neural Network Architecture

Both the generative and discriminative models are deep convolutional neural networks with- out any pooling/subsampling layers. In the generative model, all the transpose convolutional (Conv2DTranspose) layers are followed by the batch normalization layers and ReLU units. The outputs of the generative models are normalized by a hyperbolic tangent (Tanh) function. In the discriminative models, except for the output layers, all the convolutional (Conv2D) layers and fully-connected (Dense) layers are followed by the batch normalization layers, Leaky-ReLU units, and dropout layers. Details of the neural network architecture are listed in Table 5.1.

Table 5.1 Neural network architecture details

	Generator G (Layer Type, Feature Map)	Discriminator D (Layer Type, Feature Map)
Input	$3 \times 3 \times 14$	$3 \times 3 \times 5$
Layer 1	Conv2DTranspose, 64	Conv2D, 64
Layer 2	Concatenate, 896	Concatenate, 320
Layer 3	Conv2DTranspose, 1024	Dense, 1024
Layer 4	Conv2DTranspose, 512	Dense, 512
Layer 5	Conv2DTranspose, 64	Dense, 256
Output	$3 \times 3 \times 1$	$scalar \in [0, 1]$

5.5.2 Configuration

All the convolutional (Conv2D) and transpose convolutional (Conv2DTranspose) layers in our basic model are with kernel size of 3×3 and stride size of 1×1. The transpose convolutional (Conv2DTranspose) layers in the generative models are padded, the convolutional (Conv2D) layers in discriminative models are not padded. In the discriminative models, the dropout rates are set to 0.3, the small gradients are set to 0.2 when Leaky-ReLU is not active. All the neural networks are trained using standard SGD optimizer with a minibatch size of 4, i.e., $m = 4$ in Algorithm 1. The learning rates ρ_G and ρ_D are set to 0.0005, without decay and momentum. The loss functions in (5.7)-(5.14) are implemented with the following parameters: $\lambda_{adv} = \lambda_{dcl} = 0.2$ (in (5.14)), $\lambda_{\ell_p} = \lambda_{gdl} = 1$ (in (5.14)), $p = 2$ (in (5.7)), and $\alpha = 1$ (in (5.8)).

5.5.3 Performance Evaluation Metrics

To evaluate the point-by-point LMP prediction accuracy, the mean absolute percentage error (MAPE) [55] is adopted. We also adopt the Pearson correlation coefficient (PCC) [75], which is a common metric for measuring the spatial correlations between time series collected from different locations, for evaluating the prediction accuracy of spatial correlations among LMPs. PCC ranges from -1 to 1. Higher absolute values of the PCC indicate stronger spatial correlations.

To further evaluate the effectiveness of the gradient difference loss function $\mathcal{L}_{gdl}(\cdot)$ and the direction changing loss function $\mathcal{L}_{dcl}(\cdot)$ for penalizing incorrect spatial correlation predictions, two additional metrics, the spatial prediction accuracy (SPA) and the spatial mean absolute percentage error (SMAPE), are defined below to quantify the spatial correlation prediction

accuracy/error at a price node n.

$$SPA(n) = 1 - \frac{\sum_{i=1}^{N} \left| sgn(Y_n - Y_i) - sgn\left(\widehat{Y_n} - \widehat{Y_i}\right) \right| / 2}{N - 1} \tag{5.18}$$

$$SMAPE(n) = \frac{\sum_{i=1}^{N} |(Y_n - Y_i) - (\widehat{Y_n} - \widehat{Y_i})|}{\sum_{i=1}^{N} |(Y_n - Y_i)|} \tag{5.19}$$

where N represents the total number of price nodes; Y_i represents the ground truth LMP at node i ($i \neq n$); $\widehat{Y_i}$ represents the predicted LMP at node i ($i \neq n$); $sgn(\cdot)$ is the sign function in (5.10). $SPA(n)$ measures the average prediction accuracy for the price increasing or decreasing directions between node n and all other nodes. $SMAPE(n)$ measures the average prediction error for the price differences between node n and all other nodes. In this chapter, higher SPA and lower SMAPE indicate better prediction accuracy of spatial correlations.

5.5.4 Test Case Description

The proposed approach is applied to predict zonal-level LMPs in MISO [76] and SPP [65]. For both markets, historical market data from nine price zones are organized into a series of 3×3 hourly market data 2D arrays (for hour-ahead prediction) or 12×18 daily market data 2D arrays (for day-ahead prediction). The LMP prediction accuracy is evaluated by MAPE, the accuracy of the LMP spatial correlation prediction is evaluated by PCC, SPA and SMAPE. To make a fair comparison, the autoencoder approach in [55] using the same MISO dataset and another state-of-the-art approach in [1] using the same SPP dataset are used as evaluation benchmarks. A recent componential and ensemble approach in [57] is used as additional benchmark in the case studies with MISO dataset. This forecasting approach predicts energy prices, congestion prices and loss prices by three individual extremely randomized tree (ET) regressors, respectively. A meta-regressor gives the final LMP forecasting based on the summation of predicted energy price, congestion price and loss price. The MAPEs obtained from the GAN model are also compared with classical data-driven approaches including standard neural network (NN), multivariate adaptive regression splines (MARS), pure ARMA model, SVM and LASSO. Two naive prediction approaches are also included in the comparison: (A) the predicted LMPs at a specific hour is set to be the LMPs at the same hour on the previous day; (B) the predicted LMPs at a specific hour is set to be the LMPs at the previous hour. The test case data is described as follows.

5.5.4.1 Case 1

The training data set [55] contains three types of hourly MISO market data (zonal DALMPs, demands and wind generation) from January 2012 to November 2014. The trained model is tested by predicting MISO DALMPs hour by hour on several representative days selected in [55].

5.5.4.2 Case 2

The training data set contains four types of hourly SPP market data (zonal RTLMPs, DALMPs, de- mands, and generation mix data) from 6/1/2016 to 7/30/2017. The model is tested by predicting SPP RTLMPs hour by hour in the following four periods: 7/31/2017-8/13/2017, 8/21/2017-9/3/2017, 9/18/2017-10/1/2017, and 10/2/2017-10/15/2017.

Although the case studies are preformed using zonal LMPs, the proposed method can be easily applied to predicting nodal LMPs if the model is trained using nodal-level market data.

5.5.5 Performance Analysis

5.5.5.1 Case 1

The proposed GAN-based model is tested to i) forecast hourly DALMPs at NPPD, Arkansas, Louisiana, and Texas hubs in the hour-ahead manner; and ii) forecast hourly DALMPs at Indiana hub in the day-ahead manner. To reproduce testing scenarios in [55], Monday, Sep. 1st, 2014 and Sunday, Oct. 12th, 2014 are selected as two representative days for comparing the hour-ahead forecasting results.

Table 5.2 lists the results of hyperparameter selection in Case 1. After this two-step hyperparameter tuning procedure, appropriate hyperparameters with the lowest MAPE are adopted in the GAN- based price prediction model. Table 5.2 also indicates the GAN-based predictor with multiple loss functions and adversarial training (with non-zero values for all the 4 hyperparameters) has much higher prediction accuracy (lower MAPE) compared to the CNN-based predictor without adversarial training (with $\lambda_{adv} = \lambda_{gdl} = \lambda_{dcl} = 0$) or with only a subset of the 4 loss functions (with zero values for certain hyperparameters).

Table 5.2 MAPEs (%) for different hyperparameter selections in Case 1

	λ_{p}	λ_{adv}	λ_{gdl}	λ_{dcl}	MAPE
Rough	1	0	0	0	6.51
Selection	1	0.2	0	0	5.14
Fine	1	0.2	1	0	4.73
Tuning	1	0.2	0	0.2	4.67
	1	0.2	1	0.2	4.38

The MAPEs of the representative days for Louisiana and Texas hubs are computed and compared with benchmarking models in Table 5.3, in which the SDA and RS-SDA prediction models are proposed by [55]; The ETs prediction model is proposed by [57]. In [55], SDA and RS-SDA are tested on the same case using the same data. The results of SDA and RS-SDA directly come from [55]. The ETs model includes three individual ET regressors for LMP components prediction and one meta-regressor for the final summation of LMPs. In Case 1, the regressors of the ETs model are trained using historical energy prices, congestion prices and loss prices. Only the final LMP prediction results of the ETs model are listed in Table 5.3.

Table 5.3 demonstrates the proposed GAN prediction model outperforms all the other benchmarking models for hour-ahead DALMP prediction in all the testing scenarios.

Table 5.3 MAPE (%) for hour-ahead forecasting in Case 1

Model	Naive(A)	Naive(B)	NN	MARS	SVM	LASSO
Texas	31.45	5.4	6.19	6.54	7.34	7.88
Louisiana	27.34	9.15	6.19	6.28	6.14	7.70
Model	ARMA	ETs	SDA	RS-SDA	GAN	
Texas	7.02	6.43	5.42	5.16	4.83	
Louisiana	6.84	6.09	4.66	4.51	4.13	

Figure 5.5 shows the testing results for hour-ahead DALMP prediction in Case 1 on one representative day. It is observed the GAN-based model successfully captures different daily price characteristics for different locations. Table 5.4 compares the SPA and SMAPE metrics for Texas hub in Case 1, which indicates the GAN-based model outperforms other models in forecasting spatial correlations among DALMPs for Texas hub.

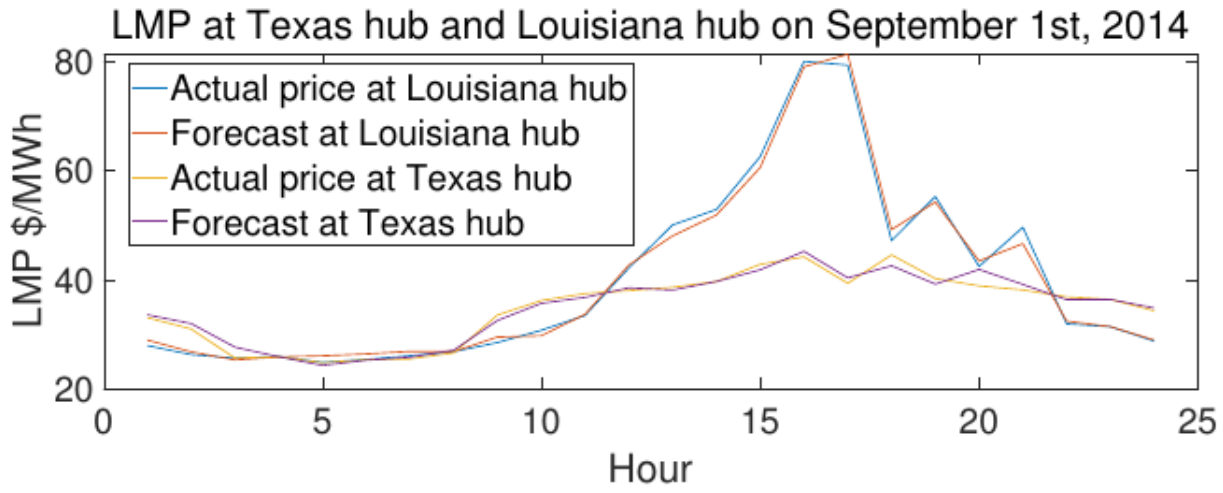

Figure 5.5 Ground-truth and forecasted DALMPs for hour-ahead forecasting in Case 1.

Table 5.4 Average SPA and SMAPE (%) for Texas hub in Case 1

Model	Naive (A)	NN	SVM	ARMA	GAN
SPA	0.53	0.67	0.59	0.69	0.78
SMAPE (%)	85	54	31	43	28

The effectiveness of the GAN-based model in day-ahead DALMP forecasting is evaluated by monthly MAPE ($MAPE_{month}$) [55]. January and July are selected (in [55]) to evaluate the forecasting results. The $MAPE_{month}$ of day-ahead DALMP forecasting obtained by different methods are listed in Table 5.5, which indicates the proposed GAN-based model outperforms all the other methods. Overall, The DALMP forecasting accuracy in January is low due to significant

price spikes frequently seen in January. Compared to the second-best-performed method RS-SDA in [55], our proposed GAN model reduces the monthly MAPE in January by 6.02%. Moreover, the RS-SDA model is updated daily with latest market data to maintain the effectiveness [55], while the proposed model does not require daily model update, resulting in much less computational burden compared to RS-SDA.

Table 5.5 $MAPE_{month}$ (%) for day-ahead forecasting in Case 1

Model	Naive	NN	MARS	SVM	LASSO	SDA	RS-SDA	GAN
January	75.65	40.47	46.35	49.64	37.46	31.80	29.78	23.76
July	53.01	12.00	20.79	23.20	11.91	10.04	8.97	8.13

5.5.5.2 Case 2

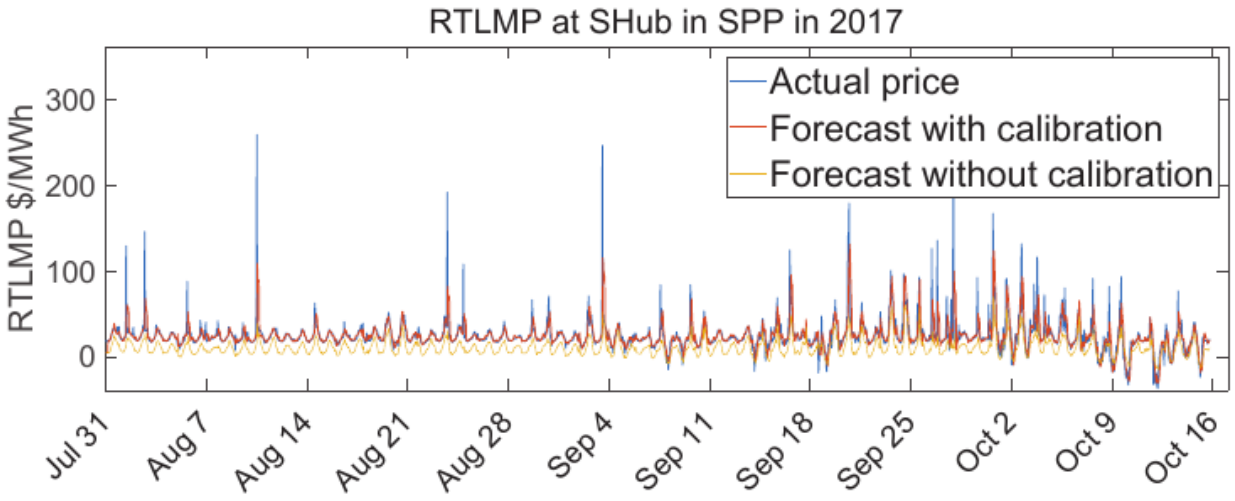

Figure 5.6 Ground-truth and forecasted RTLMPs (with and without calibration) at South Hub (SHub) price node in Case 2 (A).

The proposed GAN-based model is tested to forecast hourly RTLMPs (A): in the hour-ahead manner and (B): in the day-ahead manner. Figure 5.6 shows the ground-truth RTLMPs, the RTLMPs forecasted without ARMA calibration and the RTLMPs forecasted with ARMA calibration at South Hub (SHub) price node over the testing period in Case 2 (A). The forecasted results in Figure 5.6 indicate that the predictions of the proposed GAN model successfully capture the temporal correlations of ground-truth RTLMPs at SHub price node over the testing window. Before applying ARMA calibration, there exists an obvious deviation between the forecasted RTLMPs and the ground-truth. This is caused by the statistical discrepancies between the training and testing market data. These statistical discrepancies are commonly observed in historical market data during different years, especially when strategic market participants bid with frequently updated bidding strategies. Figure 5.6 demonstrates after applying ARMA calibration, the forecasted RTLMPs closely follow the overall trend of the ground-truth RTLMPs, which indicates the daily and weekly temporal characteristics of RTLMPs are learned by the GAN predictor. One major source of the prediction error of the proposed GAN model is the mis-prediction or under-estimation of several significant price spikes. Many significant price spikes are caused by system

contingencies and other abnormal operating conditions which are highly related to sudden changes in system modeling and topology. These modeling details are confidential to market participants. Therefore, it is difficult for purely data-driven approaches to predict price spikes from market participants' perspective.

Table 5.6 RTLMP prediction accuracy in Case 2 (B) and [1]

Approach	MAPE (%) for SHub Price Zone	MAPE (%) for NHub Price Zone
ALG+$\widehat{M}$[1]	25.4	36.9
Genscape[2]	21.7	28.2
Case 2 (B)	22.1	23.8
Case 2 (B) without DALMPs	23.5	25.4

[1] The proposed method with the best performance in [1]
[2] State-of-the-art baseline prediction from Genscape [1]

Table 5.6 shows the MAPEs obtained using the proposed approach in Case 2 (B) and two other state-of-the-art approaches in [1]. The ALG+$\widehat{M}$ method proposed in [1] does not utilize DALMP data in RTLMP forecasting. For a fair comparison, an additional GAN-based model is trained without DALMPs in Case 2. These approaches are tested using identical testing dataset from SPP's SHub and NHub (North Hub) zones. ALG+$\widehat{M}$ and GAN models are trained using only public market data. Genscape [1] is a commercial product for RTLMP forecasting, which incorporates richer and proprietary confidential market data. The proposed GAN model outperforms ALG+$\widehat{M}$ and has a comparable performance to the state-of-the-art industry benchmark Genscape, which uses confidential market data. For the NHub zone with higher price volatility, the MAPE of the proposed GAN model is less than that of Genscape by 4.4%. In Table 5.6, the proposed GAN model achieves consistent MAPEs between SHub and NHub zones. When applying the other two benchmark models, the MAPEs for the NHub zone are much higher than those for the SHub zone.

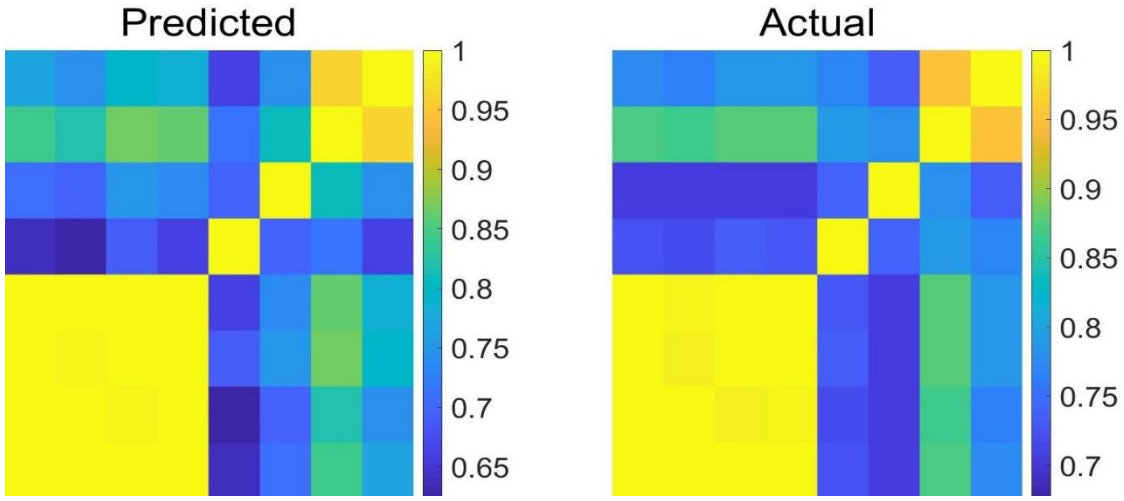

Figure 5.7 The spatial correlation coefficients matrix heatmap generated using predicted RTLMPs (left) and ground-truth RTLMPs (right) in Case 2 (A).

PCCs are calculated for each pair of price zones in SPP. Figure 5.7 compares the spatial correlations obtained using PCCs of predicted RTLMPs with those obtained using PCCs of ground-truth RTLMPs in Case 2 (A). Each 9×9 heatmap matrix in Figure 5.7 visualizes the spatial correlation coefficients (PCCs) among 9 price zones in SPP. It indicates the proposed GAN predictor successfully captures the spatial correlations across SPP market.

5.6 Conclusions and Future Work

In this chapter, a GAN-based approach is proposed to predict system-wide RTLMPs. The proposed approach performs well across different types of price forecasting problems for various market participants. Historical public market data are organized into a general 3D tensor data structure, which stores the spatio-temporal correlations of the market data. The RTLMP prediction problem is then formulated as a 2D array prediction problem and solved using the proposed deep convolutional GAN model with multiple loss functions. The prediction accuracy is improved by an ARMA calibration approach to mitigate deviations caused by variation/uncertainty of generator bids. Case studies using real-world historical market data from MISO and SPP verify the performance of the proposed approach for both point-by-point price prediction accuracy and accuracy of capturing spatial correlations among prices at different locations. Future work could focus on price spikes prediction by incorporating additional public contingency data and market participants' strategic behaviours. Another potential area of exploration includes predicting energy price component of LMP by learning total supply-demand balance. Congestion price component and loss price component may be predicted by other spatial learning methods. The final spatio-temporal correlated nodal LMPs can be assembled based on these three individual price components.

6. Locational Marginal Price Forecasting Using Convolutional Long Short-Term Memory-Based Generative Adversarial Network

6.1 Introduction

In wholesale electricity markets, accurate price forecasting is essential for market participants to trade strategically. Meanwhile, market participants' strategic behaviors also affect the electricity prices directly. The commonly accepted electricity pricing mechanism in US is the locational marginal price (LMP), which is the dual variable derived in solving the dc optimal power flow. During operations, LMPs are calculated by system operators based on the network topology, operation parameters, generation bids, and system demands. Given explicit knowledge of network topology and other system parameters, [47, 48] prove that LMPs are a linear mapping of demands based on fixed generation cost functions. Therefore, LMPs at different price nodes are spatially correlated based on the grid topology and system-wide demand distributions. However, in real-world markets, generation cost functions are not fixed. Both generation bids and demands vary over time. Uncertainties in the time-varying generation bids (with bid-in values for generation cost functions) and demands jointly determine the temporal correlations among LMPs.

However, neither physical network models nor generation bids are explicit to market participants. To forecast LMPs from the market participants' perspective, statistic approaches and data-driven approaches using only publicly available market data are the major candidate solutions.

Time-series based statistical models are widely accepted to learn linear relationships in historical LMPs. The ARMAX model [53], ARIMA model [54], and AGARCH model [77] are applied to forecast LMPs for individual price node. Spatial correlations among historical LMPs are completely ignored by these time-series based statistical models.

Many data-driven LMP forecasting methods are developed based on learning system pattern regions (SPR) [14]. In [15, 52], various SPR based approaches are applied to forecast LMPs using only publicly available historical market data. The LMP forecasting accuracy of these SPR based approaches highly depends upon the nodal load forecasting accuracy and the assumption of fixed bidding strategies for all the generators. However, these conditions do not hold in real-world markets.

Machine learning methods, such as neural networks [55, 78], LASSO [56], and long short-term memory (LSTM) [79, 80] are popular in LMP forecasting. In [79, 80], LSTM is shown to perform LMP forecasting effectively. However, this naive LSTM approach is only trained by learning temporal correlations. The forecasting accuracy can be further improved by considering advanced neural network structures.

This chapter proposes a convolutional LSTM (CLSTM) based generative adversarial network (GAN) to forecast system-wide LMPs from market participants' perspective, without power grid models and generator bidding details. The LMP forecasting problem is formulated as a sequence-to-sequence forecasting problem, and the LMP spatio-temporal correlations are learned by the CLSTM network during adversarial training. The proposed approach is trained to forecast most likely future LMP sequences, which maximize the conditional probability given by historical

LMPs. Although the proposed CLSTM based GAN model is applied to forecast system-wide LMPs, this model offers a general neural network structure which can be utilized for other spatio-temporal forecasting problems in power systems, such as system-wide demand and wind/solar generation forecasting. In general, the LMP forecasting problem is more challenging than other power system forecasting problems (such as demand forecasting), since LMPs are highly volatile with price spikes. When conventional forecasting techniques are applied to LMP and demand forecasting problems, the typical forecasting errors could reach beyond 20% for LMP forecasting but around 2% for demand forecasting [16].

6.2 Sequence-to-sequence LMP forecasting

This section follows the general data structure we proposed in Chapter 5 to organize the historical LMPs into a 3D tensor. With this data structure, the CLSTM predictor in [81] is adopted to solve this spatio-temporal sequence LMP forecasting problem.

6.2.1 Data Structure and Normalization

Suppose historical hourly LMPs are collected over a geographical region represented by $N = m \times n$ price nodes for T consecutive hours. Following the general spatio-temporal data structure and normalization defined in Chapter 5, we preprocess and organize these historical data into a 3D tensor $\mathcal{X} \in \mathbb{R}^{m \times n \times T}$. The values of all elements in $\mathcal{X}$ are normalized to fall between -1 and 1. $\mathcal{X}$ consists of a sequence of 2D arrays, $\mathcal{X} = \{X^1, X^2, \cdots, X^T\}$. Each 2D array, X^t, contains system-wide LMPs from $N = m \times n$ price nodes at hour t.

6.2.2 Formulation of Sequence-to-sequence Forecasting

The objective of LMP forecasting is to use historical LMP tensor to generate a forecasted tensor $\hat{\mathcal{Y}} \in \mathbb{R}^{m \times n \times K}$, which consists of a sequence of forecasted 2D arrays $\hat{\mathcal{Y}} = \{\hat{Y}^{T+1}, \hat{Y}^{T+2}, \cdots, \hat{Y}^{T+K}\}$. $\hat{\mathcal{Y}}$ contains the predicted LMPs at the same N price nodes for the following K hours. Let $\tilde{\mathcal{Y}} = \{X^{T+1}, X^{T+2}, \cdots, X^{T+K}\}$ denote the ground truth. A suitable predictor should generate/determine the most likely future LMP tensor given the historical LMP tensor $\mathcal{X}$, which can maximize the conditional probability below:

$$\hat{\mathcal{Y}} = \arg\max_{\tilde{\mathcal{Y}}} p(\tilde{\mathcal{Y}} | \mathcal{X}) \tag{6.1}$$

6.2.3 Convolutional Long Short-Term Memory Network

To obtain the LMP predictor satisfying (6.1), the CLSTM network in [81] is adopted to build the structure of the LMP predictor. This CLSTM network is a multi-layer neural network with many learnable parameters. During the training process using historical LMP data, these learnable parameters are optimally adjusted such that upon training convergence, the CLSTM network with the learned optimal parameters is able to generate the most likely future LMP tensors satisfying (6.1).

The CLSTM network is adopted for LMP forecasting since: 1) the CLSTM network is designed for general spatio-temporal sequence forecasting problems whose inputs and outputs are both spatio-temporal sequences/tensors, and the LMP forecasting problem (whose inputs and outputs are historical and future LMP tensors) falls within this general formulation; 2) the major advantage of the CLSTM network is that, compared to the conventional LSTM network [82] which is widely acknowledged to be effective in time series forecasting (by learning temporal characteristics from historical datasets), the CLSTM network replaces the fully connected structures within the conventional LSTM network by convolution operators (which are commonly used for learning spatial characteristics from historical datasets), enabling the CLSTM network for effectively capturing spatio-temporal correlations in historical LMPs. In [81], CLSTM network solves a similar spatio-temporal precipitation sequence prediction problem over a geographic region.

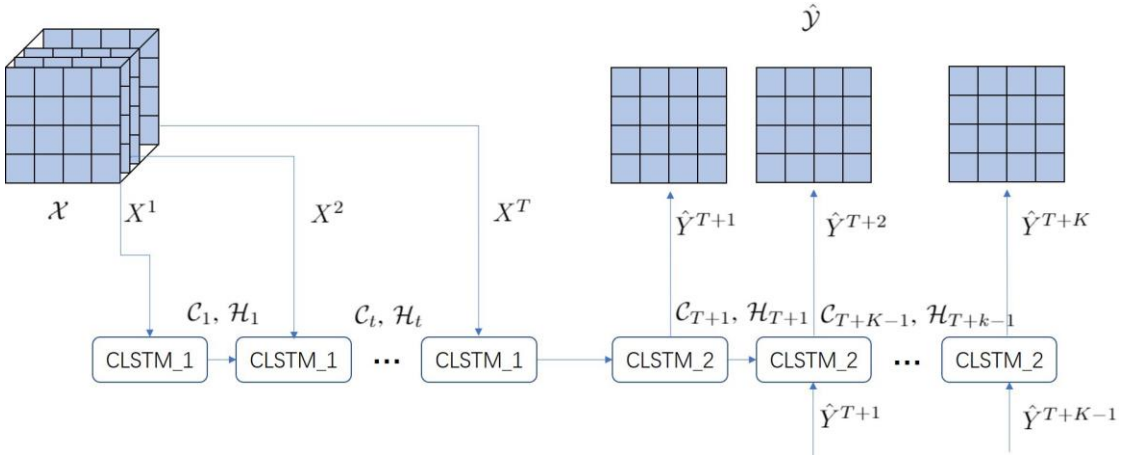

Figure 6.1 The structure of the CLSTM based LMP predictor.

Our predictor consists of two CLSTM networks, CLSTM_1 and CLSTM_2 with many learnable parameters, as shown in Figure 6.1. The CLSTM_1 network runs T times to read in the input sequences. It extracts the spatio-temporal features of historical LMPs by transitioning the 3D input historical LMP tensor $\mathcal{X} = \{X^1, X^2, \cdots, X^T\}$ to the 3D hidden state (intermediate) tensor $\{\mathcal{H}_1, \mathcal{H}_2, \cdots, \mathcal{H}_T\}$ and the corresponding 3D output tensor $\{\mathcal{C}_1, \mathcal{C}_2, \cdots, \mathcal{C}_T\}$. This output tensor contains the extracted spatio-temporal features of historical LMPs. In the $t^{th}(t \geq 2)$ step, CLSTM_1 netowrk takes two sets of inputs: 1) the 2D input historical LMP array X^t; 2) the 2D hidden state array $\mathcal{H}_{t-1}$ and the 2D output array $\mathcal{C}_{t-1}$ from the previous step. The CLSTM_2 network runs K times. It generates the forecasted LMP tensor $\hat{\mathcal{Y}} = \{\hat{Y}^{T+1}, \hat{Y}^{T+2}, \cdots, \hat{Y}^{T+K}\}$ following spatio-temporal features extracted by the CLSTM_1 network. In the $t^{th}(t \geq 2)$ step ,CLSTM_2 netowrk (for LMP prediction), takes two sets of inputs: 1) the 2D forecasted LMP array $\hat{Y}^{t-1}$; 2) the 2D hidden state array $\mathcal{H}_{t-1}$ and the 2D output array $\mathcal{C}_{t-1}$ from the previous step. In each running step, CLSTM cell performs following operations:

$$i_t = \sigma(W_{xi} * Z^t + W_{hi} * \mathcal{H}_{t-1} + W_{ci} \circ \mathcal{C}_{t-1} + b_i) \tag{6.2}$$

$$f_t = \sigma\big(W_{xf} * Z^t + W_{hf} * \mathcal{H}_{t-1} + W_{cf} \circ \mathcal{C}_{t-1} + b_f\big) \tag{6.3}$$

$$o_t = \sigma(W_{xo} * Z^t + W_{ho} * \mathcal{H}_{t-1} + W_{co} \circ \mathcal{C}_{t-1} + b_o) \tag{6.4}$$

$$\mathcal{C}_t = f_t \circ \mathcal{C}_{t-1} + i_t \circ tanh(W_{xc} * Z^t + W_{hc} * \mathcal{H}_{t-1} + b_c) \tag{6.5}$$

$$\mathcal{H}_t = o_t \circ tanh(\mathcal{C}_t) \tag{6.6}$$

where $Z^t = X^t$ and $Z^t = \hat{Y}^{t-1}$ for CLSTM_1 and CLSTM_2 networks, respectively; $*$, $\circ$, $\sigma(\cdot)$ are the convolution operator, Hadamard product, and sigmoid activation function, respectively; i_t, f_t, o_t are internal structures for each CLSTM network (the input, forget, and output gates, respectively); the weight matrices W_{xj} and biases b_j (with $j \in \{i, f, c, o\}$) are learnable parameters of the two CLSTM netowrks. In (6.5)-(6.6), for t^{th} step, the historical LMP array $Z^t = X^t$ in the CLSTM_1 netowrk and the forecasted LMP array $Z^t = \hat{Y}^{t-1}$ (generated from $(t-1)^{th}$ step) in the CLSTM_2 network are transitioned to the hidden state array $\mathcal{H}_t$ and output array $\mathcal{C}_t$, through nonlinear operations in (6.2)-(6.6).

In the above CLSTM networks, consecutive 2D arrays are read in one by one, and the temporal correlations are learned by this iterative process. Meanwhile, the spatial correlations in each iteration is captured by the inner convolution operations. Details on the internal structures of the CLSTM cell are in [81].

As Figure 6.1 shows, consecutive 2D arrays in the forecasted LMP tensor $\hat{\mathcal{Y}}$ are generated one by one, conditioned on the forecased LMP arrays from the previous steps. Therefore, the conditional probability in (6.1) can be rewritten as the product of a series of conditional probabilities:

$$p(\tilde{\mathcal{Y}}|\mathcal{X}) = p(\tilde{Y}^{T+1}|\mathcal{X}) \prod_{i=T+2}^{T+K} p\left(\tilde{Y}^i|\mathcal{X}, \tilde{Y}^{T+1}, \cdots, \tilde{Y}^{i-1}\right) \tag{6.7}$$

During training process, all learnable parameters of the two CLSTM networks, including the weight matrices W_{xj} and biases b_j (with $j \in \{i, f, c, o\}$) in (6.2)-(6.6), are optimized by minimizing the Euclidean distance between the forecasted and ground-truth 2D LMP arrays, $\hat{Y}^t$ and $\tilde{Y}^t$, using 2-norm loss:

$$\mathcal{L}_2(\hat{Y}, \tilde{Y}) = \ell_2(\hat{Y}, \tilde{Y}) = \|\hat{Y} - \tilde{Y}\|_2^2 \tag{6.8}$$

where $\|\cdot\|_2$ denotes the entry-wise 2-norm of a 2D array.

When training the CLSTM networks, simply minimizing the Euclidean distance (the 2-norm loss) over the dataset may lead to blurry prediction results which cannot maximize the conditional probability in (6.7), as discussed in [68]. Moreover, the 2-norm loss fails to consider the temporal correlations between consecutive forecasted 2D arrays $\hat{Y}^t$ and $\hat{Y}^{t+1}$, which could adversely affect the forecasting accuracy. To solve these two major drawbacks, the GAN model with multiple loss

functions in Chapter 5 is adopted to train the predictor.

6.3 GAN Model for Price Forecasting

In Chapter 5, an effective GAN model for price forecasting is proposed and evaluated. We take advantage of this GAN model, and replace the original generator and discriminator with the CLSTM networks introduced above. More details on this GAN model can be found in Chapter 5.

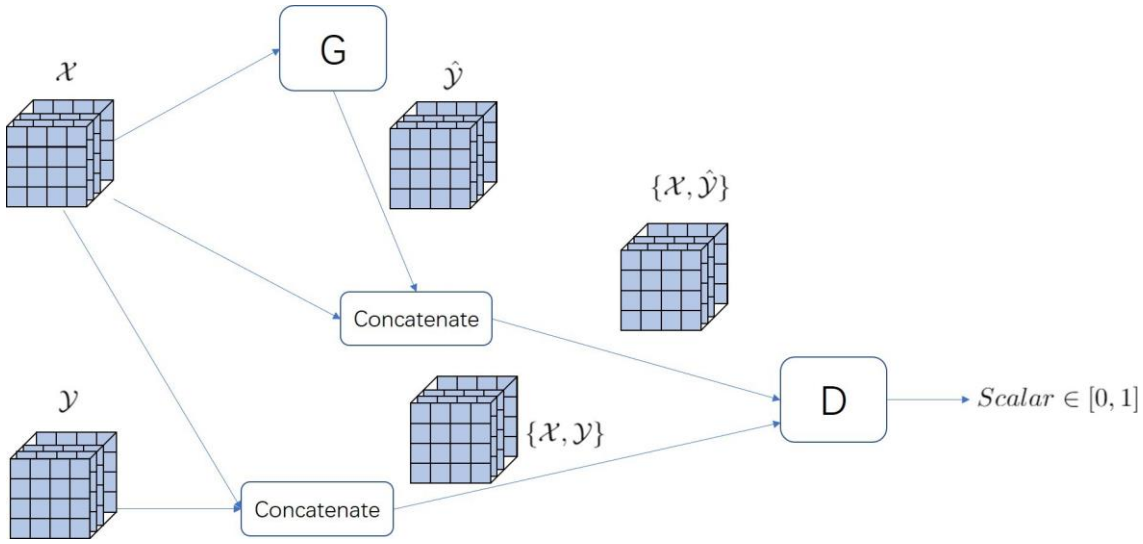

Figure 6.2: Architecture for training the CLSTM based GAN model.

6.3.1 Sequence-to-Sequence Forecasting Model with GAN

The architecture for training the sequence-to-sequence predictor through GAN model is shown in Figure 6.2. In this architecture, the CLSTM based predictor in Figure 6.1 is employed as generator G; another CLSTM based neural network is employed as discriminator D.

The generator G takes a sequence of 2D LMP arrays stored in tensor $\mathcal{X}$ as inputs, and generate a sequence of forecasted 2D LMP arrays as tensor $\hat{\mathcal{Y}}$. G is trained to maximize the conditional probability in (6.7), such that the forecasted tensor $\hat{\mathcal{Y}}$ is statistically similar to the ground-truth tensor $\tilde{\mathcal{Y}}$.

The discriminator D takes sequences $\{\mathcal{X}, \hat{\mathcal{Y}}\}$ or $\{\mathcal{X}, \tilde{\mathcal{Y}}\}$ as the input. D is trained to classify $\{\mathcal{X}, \hat{\mathcal{Y}}\}$ as fake and $\{\mathcal{X}, \tilde{\mathcal{Y}}\}$ as real. The output of D is a scalar between 0 and 1, indicating the probability of the input tensor being the ground truth.

The discriminator D and generator G are trained simultaneously; the weight matrices of D and G are updated iteratively, which follows the same training algorithm in Chapter 5. The changes we make to D and G are described below, the rest of details can be found in Chapter 5.

6.3.2 The Discriminator D

The discriminator D is a stacked CLSTM network followed by fully connected layers. The objective of D is to classify the input $\{\mathcal{X}, \tilde{\mathcal{Y}}\}$ sequence into class 1 (i.e., $\tilde{\mathcal{Y}}$ is classified as the ground-truth sequence) and the input $\{\mathcal{X}, \hat{\mathcal{Y}}\} = \{\mathcal{X}, G(\mathcal{X})\}$ sequence into class 0 (i.e., $\hat{\mathcal{Y}} = G(\mathcal{X})$ is classified as the generated fake sequence). The discriminator D is trained through minimizing the following distance function (loss function):

$$\mathcal{L}_{adv}^{D}(\mathcal{X}, \tilde{\mathcal{Y}}) = \mathcal{L}_{bce}\big(D(\{\mathcal{X}, \tilde{\mathcal{Y}}\}), 1\big) + \mathcal{L}_{bce}(D(\{\mathcal{X}, G(\mathcal{X})\}), 0) \tag{6.9}$$

where $\mathcal{L}_{bce}$ is the following binary cross-entropy:

$$\mathcal{L}_{bce}(k, s) = -[klog(s) + (1-k)log(1-s)] \tag{6.10}$$

where $k \in [0,1]$ and $s \in \{0,1\}$.

6.3.3 The Generator G

The generator G is a sequence-to-sequence predictor consisting of two CLSTMs as shown in (6.1). The input of G is a sequence of 2D LMP arrays for T hours; the output of G is a sequence of forecasted 2D LMP arrays for future K hours. During training process, the generator G is trained to minimize a certain distance between generated sequence $\hat{\mathcal{Y}}$ and the ground-truth sequence $\tilde{\mathcal{Y}}$ by the multi-loss function in (6.11), such that the conditional probability in (6.7) is maximized:

$$\mathcal{L}^{G}(\mathcal{X}, \tilde{\mathcal{Y}}) = \lambda_{adv}\mathcal{L}_{adv}^{G}(\mathcal{X}, \tilde{\mathcal{Y}}) + \lambda_{\ell_2}\mathcal{L}_2(\mathcal{X}, \tilde{\mathcal{Y}}) + \lambda_{gdl}\mathcal{L}_{gdl}(\mathcal{X}, \tilde{\mathcal{Y}}) + \lambda_{dcl}\mathcal{L}_{dcl}(\mathcal{X}, \tilde{\mathcal{Y}}) \tag{6.11}$$

where $\mathcal{L}^{G}(\mathcal{X}, \tilde{\mathcal{Y}})$ denotes the weighted multi-loss function for training G; $\mathcal{L}_{adv}^{G}(\mathcal{X}, \tilde{\mathcal{Y}})$, $\mathcal{L}_2(\mathcal{X}, \tilde{\mathcal{Y}})$, $\mathcal{L}_{gdl}(\mathcal{X}, \tilde{\mathcal{Y}})$ and $\mathcal{L}_{dcl}(\mathcal{X}, \tilde{\mathcal{Y}})$ denote four terms for this loss function (with the first and third terms explained separately in Chapter 5, the second term given in (6.8), and the last term explained in the following section); λ_{adv}, λ_{ℓ_2}, λ_{gdl}, λ_{gdl} denote hyperparameters for adjusting the weights of the four loss terms.

$\mathcal{L}_{dcl}(\mathcal{X}, \tilde{\mathcal{Y}})$ [70] is the direction changing loss function added to $\mathcal{L}^{G}(\mathcal{X}, \tilde{\mathcal{Y}})$ to solve temporal correlation mismatches:

$$\mathcal{L}_{dcl}(\mathcal{X}, \tilde{\mathcal{Y}}) = \sum_{t=T+1}^{T+K} \sum_{i,j} |\, sgn\big(\hat{Y}_{i,j}^{t} - X_{i,j}^{t-1}\big) - sgn\big(\tilde{Y}_{i,j}^{t} - X_{i,j}^{t-1}\big)| \tag{6.12}$$

where $sgn(\cdot)$ is the sign function:

$$sgn(z) \quad = \begin{cases} -1 & if\ z \le 0 \\ 0 & if\ z = 0 \\ 1 & if\ z \ge 0 \end{cases} \tag{6.13}$$

This direction changing loss function penalize incorrect temporal correlations in the forecasted sequences during the training process, such that the correct temporal correlations are learned by G. This direction changing loss function along with other loss terms can effectively resolve the blurry prediction issues caused by using only the 2-norm loss function in (6.8).

6.4 Case Studies

The proposed convolutional long short-term memory-based generative adversarial network (CLSTM- GAN) is tested using real-world LMP data from MISO [76] and ISO-NE [83]. The classic LSTM model in [79,80] and other data-driven models, such as stacked denoising autoencoders (SDA) [55], standard neural network (NN), support vector machine (SVM) and Lasso are implemented as benchmark LMP forecasting models. The model performance is evaluated by calculating the mean absolute percentage error (MAPE) of the LMP forecasts. Because our proposed approach is a sequence-to-sequence forecasting method, it can be applied to forecast LMPs for different horizons. In this section, we will show 2 cases including both on-line forecasting and day-ahead forecasting.

6.4.1 Case 1

The training dataset contains hourly ISO-NE real-time LMP data of 9 price nodes in 2016 and 2017. The testing data is hourly ISO-NE real-time LMP data of same price nodes in 2018. In Case 1(A), the proposed CLSTM-GAN model takes the tensor $\mathcal{X} \in \mathbb{R}^{3\times3\times6}$ for the past 6-hour LMPs to forecast next hour's LMPs as $\hat{\mathcal{Y}} \in \mathbb{R}^{3\times3\times1}$. In Case 1(B), the proposed CLSTM-GAN model inputs the tensor $\mathcal{X} \in \mathbb{R}^{3\times3\times24}$ for the past 24-hour LMPs to forecast next day's LMPs as $\hat{\mathcal{Y}} \in \mathbb{R}^{3\times3\times24}$.

6.4.2 Case 2

The training dataset contains hourly MISO day-ahead LMP data of 9 price nodes from January, 2012 to November, 2014. To compare with the benchmark models in [55], the testing dates used in [55] (1st, 10th, and 30th days in January, April, and August of 2014) are selected to demonstrate the forecasting accuracy. The proposed CLSTM-GAN model takes the tensor $\mathcal{X} \in \mathbb{R}^{3\times3\times24}$ for the past 24-hour LMPs as input to perform day-ahead forecasting.

6.4.3 Neural Network Architecture and Configurations

The proposed CLSTM-GAN model is implemented with Tensorflow [74] and trained on Google Colab using online GPU for acceleration. Table 6.1 lists the architecture details for G and D, where 'ConvLSTM2D' denotes the convolutional layer with CLSTM cells; 'Conv3DTranspose' denotes the convolutional transpose layer; and 'Dense' denotes the fully connected layer. In both cases, the generator G consists of 4 stacked 'ConvLSTM2D' layers (2 for CLSTM_1 and 2 for CLSTM_2); the discriminator D consists of 2 stacked 'ConvLSTM2D' layers and 3 'Dense' layers.

All the 'ConvLSTM2D' and 'Conv3DTranspose' layers in G are followed by batch normalization layers and ReLU units, while the 'ConvLSTM2D' and 'Dense' layers in D are followed by batch normalization layers, Leaky-ReLU units and dropout layers. In all the cells of the 'ConvLSTM2D' layers, the recurrent activation functions are set as sigmoid function.

In G, the kernel size of all CLSTM cells is 3×3, the stride size of all CLSTM cells is 1×1; the kernel size of all 'Conv3DTranspose' layers is $1 \times 3 \times 3$, the stride size of all 'Conv3DTranspose' layers is $1 \times 1 \times 1$; all the 'ConvLSTM2D' and 'Conv3DTranspose' layers are padded. In D, the kernel size and stride size are the same with those used in G, but all the 'ConvLSTM2D' layers are not padded; the dropout rates are set to 0.3, the small gradients are set to 0.2 when the Leaky-ReLU is not active. In all models, standard stochastic gradient descent (SGD) optimizer is utilized for adversarial training. In the training process, the minibatch size is set to 4 for all models. In Case 1(A), the learning rates for G and D are 0.005 and 0.001, respectively. In Case 1(B) and Case 2, learning rates for G and D are 0.0005 and 0.0001, respectively. For all CLSTM-GAN models, the hyperparameters in (5.14) are set to $\lambda_{adv} = \lambda_{dcl} = 0.2$, $\lambda_{\ell_p} = \lambda_{gdl} = 1$. More details on the model structures, the adversarial training algorithm, and the parameters not listed in this chapter are given in Chapter 5.

Table 6.1 Neural network architecture details

Case 1 (A)	Generator G (Layer Type, Feature Map)	Discriminator D (Layer Type, Feature Map)
Input	$3 \times 3 \times 6$	$3 \times 3 \times 7$
Layer 1	ConvLSTM2D, 64	ConvLSTM2D, 64
Layer 2	ConvLSTM2D, 256	ConvLSTM2D, 256
Layer 3	ConvLSTM2D, 128	Dense, 1024
Layer 4	ConvLSTM2D, 64	Dense, 512
Layer 5	Conv3DTranspose, 1	Dense, 256
Output	$3 \times 3 \times 1$	$scalar \in [0,1]$
Case 1 (B) Case 2	Generator G (Layer Type, Feature Map)	Discriminator D (Layer Type, Feature Map)
Input	$3 \times 3 \times 24$	$3 \times 3 \times 48$
Layer 1	ConvLSTM2D, 64	ConvLSTM2D, 64
Layer 2	ConvLSTM2D, 128	ConvLSTM2D, 256
Layer 3	ConvLSTM2D, 256	Dense, 1024
Layer 4	ConvLSTM2D, 64	Dense, 512
Layer 5	Conv3DTranspose, 1	Dense, 256
Output	$3 \times 3 \times 24$	$scalar \in [0,1]$

6.4.4 Case Study Results

In Case 1(A) and Case 1(B), the trained CLSTM-based generator G, the naive CLSTM model and the classic LSTM model are employed to perform online forecasting (Case 1(A)) and day-ahead forecasting (Case 1(B)), respectively, for ISO-NE's hourly LMPs in 2018. Figure 6.3 shows the

LMPs forecasted by G and the ground-truth LMPs at ISO-NE's VT price node in 2018 for Case 1(A).

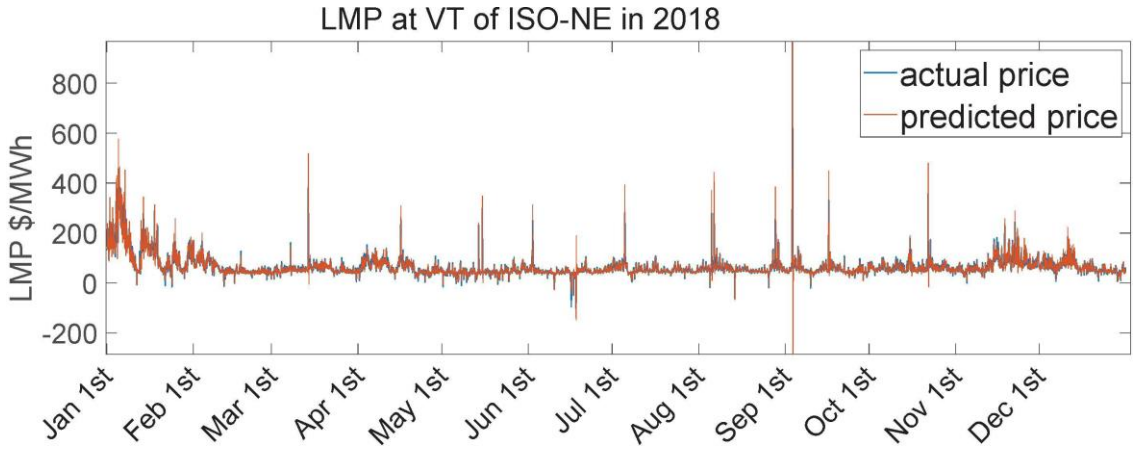

Figure 6.3: Ground-truth and forecasted LMPs at the VT price node in ISO-NE for Case 1(A).

Figure 6.3 demonstrates the forecasted LMPs successfully capture the temporal characteristics among LMPs of ISO-NE in 2018. The MAPEs of both online forecasting and day-ahead forecasting are computed and compared in Table 6.2. Table 6.2 demonstrates that the proposed CLSTM-GAN model generally has better forecasting performance compared to the classic LSTM model and the naive CLSTM model for both online forecasting and day-ahead forecasting. In the day-ahead forecasting, the LMPs in the forecasted tensor are jointly conditioned on the historical input LMP tensor and the previously forecasted LMP arrays. This will cause the forecasting errors to be accumulated during the day-ahead forecasting process, leading to much larger MAPEs in the day-ahead forecasting results compared to MAPEs in the online forecasting results, as shown in Table 6.2.

Table 6.2 LMP forecasting errors in Case 1

Case	GLSTM-GAN	GLSTM	LSTM
MAPE (%) in Case 1(A)	10.23	12.35	13.82
MAPE (%) in Case 1(B)	15.07	23.79	27.41

To further evaluate the proposed CLSTM-GAN model, the state-of-the-art SDA and RS-SDA [55] models and other popular data-driven approaches are included as benchmark models in Case 2. All models are trained using the same historical LMP data and evaluated with LMPs from the Indiana Hub in MISO. Table 6.3 shows day-ahead forecasting MAPEs obtained using different approaches on the same testing dataset.

In Table 6.3, the proposed CLSTM-GAN model (with a MAPE of 11.53%) outperforms the state-of- the-art RS-SDA forecasting model (with a MAPE of 12.18%) and all the other benchmark models. The RS-SDA model in [55] has the second best performance. However, this RS-SDA model needs to be updated/re-trained daily, causing significant computational/training burden. Besides, each well-trained RS-SDA model can only forecast LMPs for one price node. Therefore,

forecasting system-wide LMPs requires a large number of RS-SDA models. Compared to the RS-SDA model, our CLSTM-GAN model can forecast system-wide LMPs for a lone time period without daily updates, which is much more efficient.

Table 6.3 LMP forecasting errors in Case 2

Case	LSTM	NN	MARS	SVM	Lasso	SDA	RS-SDA	CLSTM-GAN
MAPE (%)	18.03	18.65	25.59	20.47	21.63	12.87	12.18	11.53

6.5 Conclusion and Future Work

This chapter proposes a CLSTM-GAN approach to forecast system-wide LMPs from market participants' perspective in online and day-ahead manners. Spatio-temporal correlations among historical LMPs are learned by the CLSTM network during adversarial training. In case studies using ISO-NE's and MISO's public data, the proposed method outperforms the state-of-the-art benchmarks and other data-driven approaches. Future work could focus on improving the LMP forecasting accuracy by considering other inputs closely related to the LMPs, such as system demand and generation information.

7. Retail Market Design and Operation for Distributed Energy Storage and Other Distributed Resources

Nomenclature

Indices and sets:

t/T	Index/set for the entire operating timespan.
k/K	Index/set for all DER aggregators (K=$\{K_1 \cup K_2 \cup K_3 \cup K_4 \cup K_5\}$).
k_1/K_1	Index/set for all DRAGs.
k_2/K_2	Index/set for all ESAGs.
k_3/K_3	Index/set for all EVCSs.
k_4/K_4	Index/set for all DDGAGs.
k_5/K_5	Index/set for all REAGs.
ϕ/Φ	Index/set for all phases.
j/J]	Index/set for all branches.
m, n/N	Index/set for all nodes.
$T' \subseteq T$	Set of hours when EVs are available.

Constants and parameters:

π_t^e	Wholesale energy price at time t (\$/MWh).
$\pi_t^{cap,up}/\pi_t^{cap,dn}$	Wholesale regulation capacity-up/down price at time t (\$/MWh).
$\pi_t^{mil,up}/\pi_t^{mil,dn}$	Wholesale regulation mileage-up/down price at time t (\$/MWh).
$\pi_{t,k}^e$	Energy offering price of DER aggregator k at time t (\$/MWh).
$\pi_{t,k}^{cap,up}/\pi_{t,k}^{cap,dn}$	Regulation capacity-up/down offering price of DER aggregator k at time t (\$/MWh).
$\pi_{t,k}^{mil,up}/\pi_{t,k}^{mil,dn}$	Regulation mileage-up/down offering price of DER aggregator k at time t (\$/MWh).
μ_t^{up}/μ_t^{dn}	Regulation mileage-up/down ratio at time t (the expected mileage for 1 MW provided regulation capacity).
S^{up}/S^{dn}	Historical scores for providing regulation mileage-up/down services.
$\overline{P}_{k_1,\phi}$	Maximum power consumption of DRAG k_1 at time t on phase ϕ (MW).
$\overline{r}_{k,\phi}^{up}/\overline{r}_{k,\phi}^{dn}$	Maximum regulation capacity-up/down for aggregator k on phase ϕ (MW).
$\eta_{k_2}^{ch}/\eta_{k_2}^{di}$	Charge/discharge efficiency of ESAG k_2.
$\overline{C}_{k_2,\phi}/\overline{D}_{k_2,\phi}$	Maximum charge/discharge rate of ESAG k_2 on phase ϕ (MW).
$\underline{E}_{k_2,\phi}$, $\overline{E}_{k_2,\phi}$	Minimum/Maximum charge level of ESAG k_2 on phase ϕ (MWh).
$\overline{R}_{k_3,\phi}^c$	Maximum charge rate of EVCS k_3 on phase ϕ (MW).
$\overline{CL}_{k_3,\phi}$	Maximum charge level of EVCS k_3 on phase ϕ (MWh).

$E_{k_3,\phi}^{int}$	Initial charge level of EVCS k_3 on phase ϕ (MWh).
$\gamma_{k_3}^{ch}$	Charge efficiency of EVCS k_3.
$\overline{P}_{k_4,\phi}/P_{k_4,\phi}$	Maximum/minimum power generation of DDGAG k_4 on phase ϕ (MW).
$H_{n,k}$	Mapping matrix of aggregator k to node n.
H_n^{sub}	Mapping matrix of substation to node n.
$P_{t,n,\phi}^D/Q_{t,n,\phi}^D$	Inelastic active/reactive power load at time t at node n on phase ϕ (MW).
$A_{j,n}$	Incidence matrix of branches and nodes.
δ	Phase angle.
$C_{m,n}$	Incidence matrix of nodes.
$Z_{j,\phi,\psi}$	Impedance between phases ϕ and ψ of branch j ().
$V/\overline{V}$	Lower/Upper voltage limit (kV).
$\overline{Pl_j}/\overline{Ql_j}$	Maximum active/reactive permissible flow of branch j (MW/MVar).

Variables:

$P_{t,\phi}^{sub}/Q_{t,\phi}^{sub}$	DSO's aggregated offer to the wholesale energy market at time t on phase ϕ (MW).
$r_{t,\phi}^{sub,up}/r_{t,\phi}^{sub,dn}$	DSO's aggregated offer to wholesale regulation capacity-up/down market at time t on phase ϕ (MW).
$P_{t,k,\phi}$	Energy offer made by aggregator k at time t on phase ϕ (MW).
$r_{t,k,\phi}^{up}/r_{t,k,\phi}^{dn}$	Regulation capacity-up/down offer of aggregator k at time t on phase ϕ (MW).
$E_{t,k_2,\phi}$	Charge level of ESAG k_2 at time t on phase ϕ (MWh).
$P_{t,k_2,\phi}^{di}/P_{t,k_2,\phi}^{ch}$	Discharge/charge power of ESAG k_2 at time t on phase ϕ (MW).
$r_{t,k_2,\phi}^{up,di}/r_{t,k_2,\phi}^{dn,di}$	Regulation capacity-up/down provided by ESAG k_2 at time t on phase ϕ in the discharge mode (MW).
$r_{t,k_2,\phi}^{dn,ch}/r_{t,k_2,\phi}^{up,ch}$	Regulation capacity-up/down provided by ESAG k_2 at time t on phase ϕ in the charge mode (MW).
$b_{t,k_2,\phi}$	Binary variable indicating charge or discharge ($b_{t,k_2,\phi} = 0$ or 1) mode of ESAG k_2 at time t on phase ϕ.
$b_{k_3,\phi}$	Binary variable for not allocating the minimum power to EVCS k_3 on phase ϕ when its offering price is low (when $b_{k_3} = 0$).
$Pl_{j,t,\phi}/Ql_{j,t,\phi}$	Active/reactive power flow of branch j at time t on phase ϕ in (MW/MVar).
$S_{j,\phi}$	Apparent power of branch j on phase ϕ (MVA).
$I_{j,\phi}$	Current of branch j on phase ϕ (A).
$V_{n,\phi}$	Voltage of node n on phase ϕ (kV).

7.1 Introduction

The Federal Energy Regulatory Commission (FERC) Order No. 2222 has required all the US independent system operators (ISOs) to completely open their wholesale markets for distributed energy resources (DERs) [84]. A huge number of DER aggregators are anticipated to enter the wholesale energy and ancillary services markets in the near future. This may cause significant challenges to transmission and distribution operations [85]: 1) These aggregators are modeled as small generators in the ISO's market system. Adopting a huge number of these small generators could cause a significant computational burden to the ISO's unit commitment and economic dispatch process. 2) To participate in the ISO's market, the aggregators need to control numerous DER outputs across the distribution system without any information on the operating constraints of the distribution grid, which could cause voltage and thermal violations in the distribution system. Therefore, there is a need for an entity to coordinate DER aggregators' market activities while assuring the secure and reliable operation of the distribution network and reducing the computational burden for the wholesale market clearing process [86].

Existing works on DER market participation fall into two categories. The first category considers DERs participating in the wholesale markets directly through aggregators [87–92]. As the number of DER aggregators explodes in the wholesale market, these works cannot effectively alleviate the ISO's market clearing computational burden, as they allow numerous aggregators to enter the wholesale market directly. Moreover, these works either completely ignore distribution system operating constraints and neglect the secure and reliable operation of the distribution system while coordinating the DER market participation [87–90], or consider distribution system operating constraints using DC power flow which is inappropriate due to high impedances in the distribution network [91, 92].

The second category of works defines the distribution system operator (DSO) to coordinate the DER market participation [93–101]. In [93], the day-ahead market framework operated by a DSO is presented. In [94], to meet DSO request, a local flexibility market is proposed for selling flexibility. In [93, 94], the distribution network and corresponding constraints are not modeled. In [95], the day-ahead energy and reserve markets are presented for a DSO. In [96], a local market operated by the distribution market operator (DMO) is presented. The proposed DMO gathers offers from microgrids and aggregates them to participate in the wholesale market. In [95, 96], DC power flow is adopted to model power balance constraints which is inappropriate for distribution networks with high network resistances. In [97], a bilateral electricity market in the distribution system is proposed. In [98], a day-ahead market model operated by a DSO is presented. The DSO considers DERs offers as well as interaction with the wholesale market in order to clear the day-ahead market in the distribution system. In [99], a re-dispatch optimal power flow (OPF) is modeled as a congestion management method implemented by a DSO. In [100], a comprehensive congestion management method for a DSO is presented using dynamic tariff, network reconfiguration, and flexibility provided by aggregators. In [97–100], wholesale market participation of DERs is not considered.

Several questions remain unexplored in existing literature. How to design a DSO to coordinate DER aggregators' wholesale market participation as well as operating the retail/local market? How does a DSO coordinate the DER aggregators' regulation market participation? What is the appropriate market settlement approach for the DSO in coordination with the wholesale market

clearing process? How does the DSO operate the unbalanced retail/local market while submitting three-phase balanced offers to the wholesale market?

This chapter extends our prior works in [102] and [103] to further integrate single-phase DER aggregators for wholesale and retail markets participation considering a market settlement procedure. This study addresses the above questions with the following major contributions:

- A DSO framework is proposed to optimally coordinate various DER aggregators, including the demand response aggregators (DRAGs), renewable energy aggregators (REAGs), energy storage aggregators (ESAGs), dispatchable distributed generation aggregators (DDGAGs), and electric vehicle charging stations (EVCSs), for the wholesale market participation while operating the retail market.
- A market settlement approach is proposed for the DSO, which coordinates with the wholesale market clearing process and ensures the DSO's non-profit characteristic.
- A linearized unbalanced power flow is presented to handle the single-phase market participants while assuring three-phase balanced offers to the wholesale market.
- The DSO's market outcomes and market settlement process are investigated through case studies on small and large distribution test systems.

The proposed DSO reduces the computational burden for wholesale market clearing by moving the DER-related market clearing computations to the DSO level, while satisfying distribution system operating constraints and being compatible with the current wholesale market structures.

7.2 The DSO Framework

In this chapter, the DSO is considered as the non-profit distribution system and market operator. The DSO, shown in Figure 7.1, serves as a mediator that trades with the wholesale market at the substation on one hand and interacts with DER aggregators and end-user customers on the other hand. The DER aggregators submit their energy and regulation offers to the DSO instead of to the wholesale market directly. The DSO collects the offers to operate the retail market and coordinate the retail offers to construct an aggregated bid for participating in the ISO's day-ahead wholesale energy and regulation markets. Once the day-ahead wholesale energy and regulation markets are cleared, the DSO's share in the wholesale market will be determined. The DSO will then distribute this awarded share to all the retail market participants.

The proposed DSO coordinates with the ISO to form a hierarchical wholesale/retail market mechanism. Compared to the existing mechanism which requires the modeling of a huge number of aggregators in the wholesale market clearing process, this hierarchical mechanism could significantly reduce the computational burden for wholesale market clearing while satisfying distribution system operating constraints.

On the wholesale market side, without loss of generality, this chapter adopts the market rules of California ISO (CAISO), whose pay-for-performance regulation market considers regulation capacity (capacity-up and capacity-down) and regulation mileage (mileage-up and mileage-down)

[104].

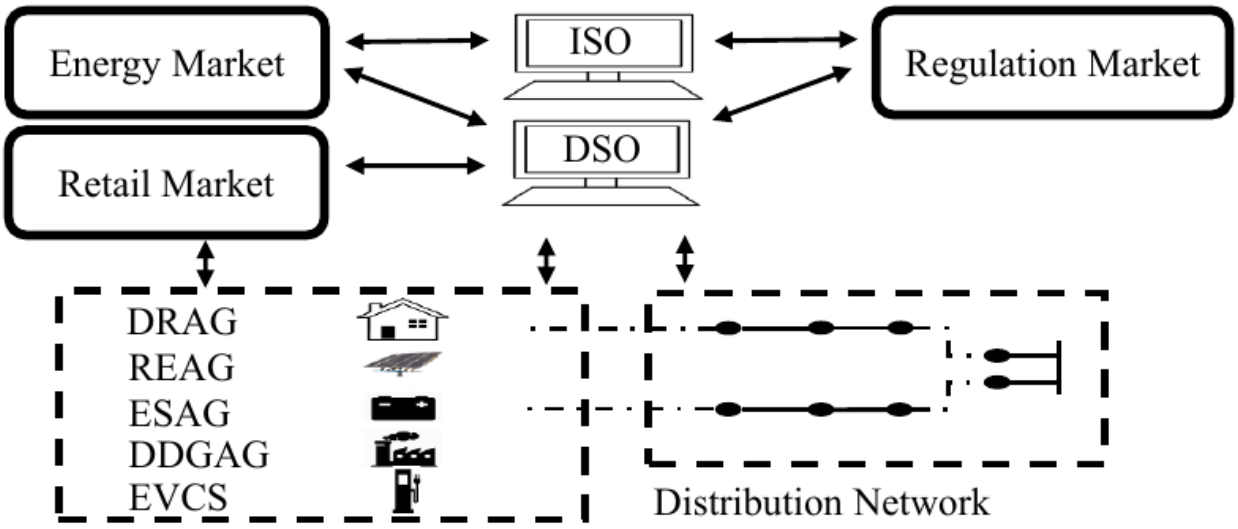

Figure 7.1 Framework of the DSO.

7.3 Mathematical Model of The DSO Market

In this section, the optimization problem is formulated for the DSO which operates the retail market and aggregates the offers from DER aggregators for participating in the wholesale energy and regulation markets.

7.3.1 The Objective Function

The DSO minimizes the total operational cost across the distribution network, considering 1) costs of buying/selling energy in the wholesale energy and regulation markets; 2) costs of paying various types of DER aggregators for providing energy and regulation in the retail market. The DSO is assumed to be a price-taker in the wholesale market. The objective function of the proposed model is as follows:

$$\begin{aligned} Min \quad & \sum_{\phi\in\Phi}\sum_{t\in T}[P_{t,\phi}^{sub}\,\pi_t^e - r_{t,\phi}^{sub,up}\pi_t^{cap,up} - r_{t,\phi}^{sub,dn}\pi_t^{cap,dn} \\ & -r_{t,\phi}^{sub,up}S^{up}\mu_t^{up}\pi_t^{mil,up} - r_{t,\phi}^{sub,dn}S^{dn}\mu_t^{dn}\pi_t^{mil,dn} \\ & + \sum_{k\in\{K_2\cup K_4\}} P_{t,k,\phi}\pi_{t,k}^e - \sum_{k\in\{K_1\cup K_3\}} P_{t,k,\phi}\pi_{t,k}^e \\ & + \sum_{k\in K}[r_{t,k,\phi}^{up}\,\pi_{t,k}^{cap,up} + r_{t,k,\phi}^{dn}\pi_{t,k}^{cap,dn} \\ & + r_{t,k,\phi}^{up}S^{up}\mu_t^{up}\pi_{t,k}^{mil,up} + r_{t,k,\phi}^{dn}S^{dn}\mu_t^{dn}\pi_{t,k}^{mil,dn}] \end{aligned} \tag{7.1}$$

In (7.1), the wholesale energy market is modeled as a producer for the DSO, while the wholesale

regulation market is modeled as a consumer for the DSO. Therefore, cost terms corresponding to the wholesale energy market are associated with positive signs, while cost terms corresponding to the wholesale regulation market are associated with negative signs. The EVCSs and DRAGs are also modeled as consumers in the DSO's retail energy market, whose cost terms are associated with negative signs.

7.3.2 Constraints for Demand Response Aggregators (DRAGs)

The DRAGs operating constraints are as follows:

$$P_{t,k_1,\phi} - r^{dn}_{t,k_1,\phi} \geq 0; \forall t \in T, \forall k_1 \in K_1, \forall \phi \in \Phi \tag{7.2a}$$

$$P_{t,k_1,\phi} + r^{up}_{t,k_1,\phi} \leq \overline{P}_{k_1,\phi}; \forall t \in T, \forall k_1 \in K_1, \forall \phi \in \Phi \tag{7.2b}$$

$$0 \leq r^{up}_{t,k_1,\phi} \leq \overline{r}^{up}_{k_1,\phi}; \forall t \in T, \forall k_1 \in K_1, \forall \phi \in \Phi \tag{7.2c}$$

$$0 \leq r^{dn}_{t,k_{1,\phi}} \leq \overline{r}^{dn}_{k_1,\phi}; \forall t \in T, \forall k_1 \in K_1, \forall \phi \in \Phi \tag{7.2d}$$

In (7.2a)-(7.2b), DRAG's offers to energy, regulation capacity-up, and capacity-down markets are limited with respect to minimum and maximum power consumption. In (7.2c)-(7.2d), regulation capacity-up and capacity-down are limited with respect to their permitted values.

7.3.3 Constraints for Energy Storage Aggregators (ESAGs)

The operating constraints for ESAGs are as follows, for $\forall t \in T, \forall k_2 \in K_2, \forall \phi \in \Phi$:

$$P_{t,k_2,\phi} = E_{t-1,k_2,\phi} - E_{t,k_2,\phi} + (1/\eta^{di}_{k_2}) r^{up}_{t,k_2,\phi} \mu^{up}_t - (\eta^{ch}_{k_2}) r^{dn}_{t,k_2,\phi} \mu^{dn}_t \tag{7.3a}$$

$$P_{t,k_2,\phi} = (1/\eta^{di}_{k_2}) P^{di}_{t,k_2,\phi} - (\eta^{ch}_{k_2}) P^{ch}_{t,k_2,\phi} \tag{7.3b}$$

$$r^{up}_{t,k_2,\phi} = r^{up,di}_{t,k_2,\phi} + r^{dn,ch}_{t,k_2,\phi} \tag{7.3c}$$

$$r^{dn}_{t,k_2,\phi} = r^{dn,di}_{t,k_2,\phi} + r^{up,ch}_{t,k_2,\phi} \tag{7.3d}$$

$$\underline{E}_{k_2,\phi} \leq E_{t,k_2,\phi} \leq \overline{E}_{k_2,\phi} \tag{7.3e}$$

$$0 \leq P^{di}_{t,k_2,\phi} \leq b_{t,k_2,\phi} \overline{D}_{k_2,\phi} \tag{7.3f}$$

$$0 \leq r^{up,di}_{t,k_2,\phi} \leq b_{t,k_2,\phi} \overline{r}^{up}_{k_2,\phi} \tag{7.3g}$$

$$0 \leq r^{dn,di}_{t,k_2,\phi} \leq b_{t,k_2,\phi} \overline{r}^{dn}_{k_2,\phi} \tag{7.3h}$$

$$0 \leq P^{ch}_{t,k_2,\phi} \leq (1 - b_{t,k_2,\phi}) \overline{C}_{k_2,\phi} \tag{7.3i}$$

$$0 \leq r^{up,ch}_{t,k_2,\phi} \leq (1 - b_{t,k_2,\phi}) \overline{r}^{dn}_{k_2,\phi} \tag{7.3j}$$

$$0 \le r_{t,k_2,\phi}^{dn,ch} \le (1 - b_{t,k_2,\phi})\overline{r}_{k_2,\phi}^{up} \tag{7.3k}$$

$$r_{t,k_2,\phi}^{dn,di} \le P_{t,k_2,\phi}^{di} \le \overline{D}_{k_2,\phi} - r_{t,k_2,\phi}^{up,di} \tag{7.3l}$$

$$r_{t,k_2,\phi}^{dn,ch} \le P_{t,k_2,\phi}^{ch} \le \overline{C}_{k_2,\phi} - r_{t,k_2,\phi}^{up,ch} \tag{7.3m}$$

Equation (7.3a) defines the injected power of ESAGs. Equations (7.3b)-(7.3d) decompose the energy, regulation capacity-up, and regulation capacity-down offers into their corresponding values in the charge and discharge modes. In (7.3e), charge levels are limited within the upper and lower limits. Equations (7.3f)-(7.3k) limit the injected power, regulation capacity-up offers, and capacity-down offers with respect to their maximum values in the charge/discharge modes. Equations (7.3l)-(7.3m) ensure the charged/discharged power is limited with respect to the maximum charge/discharge rate and the regulation capacity-up and capacity-down offers in the charge/discharge modes, respectively.

7.3.4 Constraints for EV Charging Stations (EVCSs)

EVCSs are modeled as EV charging aggregators and are assumed to have unidirectional power flow [105]. Constraints related to the operation of EVCSs are as follows:

$$0 \le P_{t,k_3,\phi} \le \overline{R}_{k_3,\phi}^{c} b_{k_3,\phi}; \forall t \in T', \forall k_3 \in K_3, \forall \phi \in \Phi \tag{7.4a}$$

$$0 \le r_{t,k_3,\phi}^{up} \le \overline{r}_{k_3,\phi}^{up} b_{k_3,\phi}; \forall t \in T', \forall k_3 \in K_3, \forall \phi \in \Phi \tag{7.4b}$$

$$0 \le r_{t,k_3,\phi}^{dn} \le \overline{r}_{k_3,\phi}^{dn} b_{k_3,\phi}; \forall t \in T', \forall k_3 \in K_3, \forall \phi \in \Phi \tag{7.4c}$$

$$P_{t,k_3,\phi} + r_{t,k_3,\phi}^{up} \le \overline{R}_{k_3,\phi}^{c}; \forall t \in T', \forall k_3 \in K_3, \forall \phi \in \Phi \tag{7.4d}$$

$$P_{t,k_3,\phi} - r_{t,k_3,\phi}^{dn} \ge 0; \forall t \in T', \forall k_3 \in K_3, \forall \phi \in \Phi \tag{7.4e}$$

$$\begin{aligned} 0.9\overline{CL}_{k_3,\phi} b_{k_3,\phi} \le E_{k_3,\phi}^{int} b_{k_3,\phi} + \sum_{t \in T'} [P_{t,k_3,\phi} + r_{t,k_3,\phi}^{up} \mu_t^{up} - r_{t,k_3,\phi}^{dn} \mu_t^{dn}] \gamma_{k_3}^{ch} \\ \le \overline{CL}_{k_3,\phi} b_{k_3,\phi}; \forall k_3 \in K_3, \forall \phi \in \Phi \end{aligned} \tag{7.4f}$$

Equations (7.4a)-(7.4c) limit EVCSs' energy, regulation capacity-up, and capacity-down offers within their maximum values. In (7.4d)-(7.4e), the energy offer is limited with respect to the maximum charge rate and the regulation capacity-up and capacity-down offers. Equation (7.4f) ensures the EVCSs are fully charged.

7.3.5 Constraints for Dispatchable DG Aggregators (DDGAGs)

The operating constraints for DDGAGs are as follows:

$$P_{t,k_4,\phi} + r_{t,k_4,\phi}^{up} \le \overline{P}_{k_4,\phi}; \forall t \in T, \forall k_4 \in K_4, \forall \phi \in \Phi \tag{7.5a}$$

$$P_{t,k_4,\phi} - r^{dn}_{t,k_4,\phi} \geq \underline{P}_{k_4,\phi}; \forall t \in T, \forall k_4 \in K_4, \forall \phi \in \Phi \quad (7.5b)$$

$$0 \leq r^{up}_{t,k_4,\phi} \leq \overline{r}^{up}_{k_4,\phi}; \forall t \in T, \forall k_4 \in K_4, \forall \phi \in \Phi \quad (7.5c)$$

$$0 \leq r^{dn}_{t,k_4,\phi} \leq \overline{r}^{dn}_{k_4,\phi}; \forall t \in T, \forall k_4 \in K_4, \forall \phi \in \Phi \quad (7.5d)$$

Equations (7.5a)-(7.5b) limit the energy, regulation capacity-up, and capacity-down offers with respect to the minimum and maximum power generations, respectively. Equations (7.5c)-(7.5d) limit the regulation capacity-up and capacity-down offers within their permitted values, respectively.

7.4 The Linearized Three-Phase Power Flow

The distribution system operation is unbalanced due to single-phase loads. The linearized three-phase power flow is considered to model the unbalanced operation [106,107]. Consider a branch $j \in J$ which connects node $n \in N$ to node $m \in N$. The voltage drop across a branch is defined as follows:

$$V_{m,\phi} = V_{n,\phi} - \sum_{\psi \in \Phi} Z_{j,\phi,\psi} I_{j,\psi} \quad (7.6)$$

Substituting $I_{j,\psi}$ by $I_{j,\psi} = S^*_{j,\psi}/V^*_{n,\phi}$, multiplying both sides of the resulting equation by their complex conjugates, and assuming 1) the branch losses are negligible (i.e., $\left|Z_{j,\phi,\psi}\right|^2 \left|S_{j,\psi}\right|^2 / \left|V_{n,\phi}\right|^2 \approx 0$), 2) the voltages are approximately balanced (i.e., $\frac{V_{n,a}}{V_{n,b}} \approx \frac{V_{n,b}}{V_{n,c}} \approx \frac{V_{n,c}}{V_{n,a}} \approx e^{j2\pi/3}$), the following equations are obtained:

$$U_{m,\phi} = U_{n,\phi} - \sum_{\psi \in \Phi} \alpha_{\phi,\psi} Z_{j,\phi,\psi} S^*_{j,\psi} - \sum_{\psi \in \Phi} \alpha^*_{\phi,\psi} Z^*_{j,\phi,\psi} S_{j,\psi} \quad (7.7)$$

$$U_{m,\phi} = |V_{m,\phi}|^2, U_{n,\phi} = |V_{n,\phi}|^2 \quad (7.8)$$

$$\alpha_{\phi,\psi} = \begin{bmatrix} 1 & e^{-\frac{i2\pi}{3}} & e^{\frac{i2\pi}{3}} \\ e^{\frac{i2\pi}{3}} & 1 & e^{-\frac{i2\pi}{3}} \\ e^{-\frac{i2\pi}{3}} & e^{\frac{i2\pi}{3}} & 1 \end{bmatrix} \quad (7.9)$$

In (7.7), substituting the complex variables by their real and imaginary parts (using $Z_{j,\phi,\psi} = r_{j,\phi,\psi} + ix_{j,\phi,\psi}$, $S_{j,\psi} = P_{j,\psi} + iQ_{j,\psi}$, $\alpha_{\phi,\psi} = \alpha^{re}_{\phi,\psi} + i\alpha^{im}_{\phi,\psi}$), the following equation is obtained as the DSO operating constraint:

$$U_{m,\phi} = U_{n,\phi} \quad - \sum_{\psi \in \Phi} (2\alpha^{re}_{\phi,\psi} r_{j,\phi,\psi} - 2\alpha^{im}_{\phi,\psi} x_{j,\phi,\psi}) P_{j,\psi} - \sum_{\psi \in \Phi} (2\alpha^{re}_{\phi,\psi} x_{j,\phi,\psi} + 2\alpha^{im}_{\phi,\psi} r_{j,\phi,\psi}) Q_{j,\psi} \tag{7.10}$$

Using the voltage drop equation in (7.10) and considering power balance at each node, the following three-phase power flow model is obtained:

$$-H^{sub}_n P^{sub}_{t,\phi} + P^D_{t,n,\phi} + \sum_{k \in \{K_1 \cup K_3\}} H_{n,k} P_{t,k,\phi} - \sum_{k \in \{K_2 \cup K_4 \cup K_5\}} H_{n,k} P_{t,k,\phi} + \sum_{j \in J} Pl_{j,t,\phi} A_{j,n} = 0; \quad \forall t \in T, \forall n \in N, \forall \phi \in \Phi \tag{7.11a}$$

$$-H^{sub}_n Q^{sub}_{t,\phi} + \sum_{k_1 \in K_1} H_{n,k_1} P_{t,k_1,\phi} tan\delta_{k_1} + Q^D_{t,n,\phi} - \sum_{k_4 \in K_4} H_{n,k_4} P_{t,k_4,\phi} tan\delta_{k_4} + \sum_{j \in J} Ql_{j,t,\phi} A_{j,n} = 0 \,; \forall t \in T, \forall n \in N, \forall \phi \in \Phi \tag{7.11b}$$

$$U_{m,t,\phi} = U_{n,t,\phi} - \sum_{\psi \in \Phi} (2\alpha^{r}_{\phi,\psi} r_{j,\phi,\psi} - 2\alpha^{x}_{\phi,\psi} x_{j,\phi,\psi}) Pl_{j,t,\psi} - \sum_{\psi \in \Phi} (2\alpha^{r}_{\phi,\psi} x_{j,\phi,\psi} + 2\alpha^{x} r_{j,\phi,\psi}) Ql_{j,t,\psi} \,; \forall t \in T, \quad \forall (m,n) \in C_{mn}, \forall (n,j) \in A_{j,n}, \forall \phi \in \Phi \tag{7.11c}$$

$$\underline{V}^2 \leq U_{n,t,\phi} \leq \overline{V}^2; \forall t \in T, \forall n \in N, \forall \phi \in \Phi \tag{7.11d}$$

$$-\overline{Pl}_j \leq Pl_{j,t,\phi} \leq \overline{Pl}_j; \forall t \in T, \forall j \in J, \forall \phi \in \Phi \tag{7.11e}$$

$$-\overline{Ql}_j \leq Ql_{j,t,\phi} \leq \overline{Ql}_j; \forall t \in T, \forall j \in J, \forall \phi \in \Phi \tag{7.11f}$$

$$r^{sub,up}_{t,\phi} = \sum_{k_2 \in K_2} r^{up}_{t,k_2,\phi} + \sum_{k_4 \in K_4} r^{up}_{t,k_4,\phi} + \sum_{k_1 \in K_1} r^{dn}_{t,k_1,\phi} + \sum_{k_3 \in K_3} r^{dn}_{t,k_3,\phi} \,; \forall t \in T, \forall \phi \in \Phi \tag{7.11g}$$

$$r_{t,\phi}^{sub,dn} = \sum_{k_2 \in K_2} r_{t,k_2,\phi}^{dn} + \sum_{k_4 \in K_4} r_{t,k_4,\phi}^{dn} + \sum_{k_1 \in K_1} r_{t,k_1,\phi}^{up} + \sum_{k_3 \in K_3} r_{t,k_3,\phi}^{up}; \forall t \in T, \forall \phi \in \Phi \quad (7.11h)$$

$$P_{t,A}^{sub} = P_{t,B}^{sub} = P_{t,C}^{sub}; \forall t \in T \quad (7.11i)$$

$$r_{t,A}^{sub,up} = r_{t,B}^{sub,up} = r_{t,C}^{sub,up}; \forall\, t \in T \quad (7.11j)$$

$$r_{t,A}^{sub,dn} = r_{t,B}^{sub,dn} = r_{t,C}^{sub,dn}; \forall t \in T \quad (7.11k)$$

Equations (7.11a)-(7.11b) ensure the summation of active/reactive power at each node is zero. The voltage drop at each branch is defined by (7.11c). Equation (7.11d) ensures the voltage at each node remains within its upper/lower limits. In (7.11e)-(7.11f), the active/reactive power flow of each branch is limited within its maximum value in both directions. Equations (7.11g)-(7.11h) balance the regulation capacity-up/capacity-down offers from the aggregators and to the wholesale market. Equations (7.11i)-(7.11k) ensure the aggregated offers submitted by the DSO to the wholesale market are three-phase balanced.

7.5 The Market Settlement

The DSO trades with the wholesale market on one hand and coordinates the DER aggregators within the retail market on the other hand. Therefore, the market settlements for the DSO and ISO need to be coordinated. The ISO and DSO can be viewed as the market participant in each other's market. When the DSO market is cleared, the DSO determines distribution locational marginal prices, D-LMPs, at each phase across its territory. However, the DSO cannot determine the price for the ISO (which is assumed as a participant in the DSO market) at the DSO-ISO coupling point, since the price at this location is determined by the ISO's wholesale market clearing process.

Lemma 1. *At the wholesale-DSO coupling substation, the total payment received/compensated by the DSO under the wholesale price is identical to that under three single-phase D-LMPs for each phase at the substation.*

Proof. Assume continuous relaxation of the problem in Section 7.3. Let x^{dr}, x^{es}, x^{ev}, x^{ddg}, and x^{pf} be the sets with all decision variables related to DRAGs, ESAGs, EVCSs, DDGAGs, and power flow equations, with corresponding constraints $\mathrm{g}(\mathrm{x}^{dr})$, $\mathrm{g}(\mathrm{x}^{es})$, $\mathrm{g}(\mathrm{x}^{ev})$, $\mathrm{g}(\mathrm{x}^{ddg})$, $\mathrm{g}(\mathrm{x}^{pf})$, and corresponding dual variables $\boldsymbol{\lambda}^{dr}$, $\boldsymbol{\lambda}^{es}$, $\boldsymbol{\lambda}^{ev}$, $\boldsymbol{\lambda}^{ddg}$, and $\boldsymbol{\lambda}^{pf}$, respectively. The Lagrangian function can be set up as:

$$\begin{aligned} \mathbf{L} = \; & f(\mathrm{x}^{dr}, \mathrm{x}^{es}, \mathrm{x}^{ev}, \mathrm{x}^{ddg}) + (\boldsymbol{\lambda}^{dr})^{\mathrm{T}} \mathrm{g}(\mathrm{x}^{dr}) \\ & + (\boldsymbol{\lambda}^{es})^{\mathrm{T}} \mathrm{g}(\mathrm{x}^{es}) + (\boldsymbol{\lambda}^{ev})^{\mathrm{T}} \mathrm{g}(\mathrm{x}^{ev}) \\ & + (\boldsymbol{\lambda}^{ddg})^{\mathrm{T}} \mathrm{g}(\mathrm{x}^{ddg}) + (\boldsymbol{\lambda}^{pf})^{\mathrm{T}} \mathrm{g}(\mathrm{x}^{pf}) \end{aligned} \quad (7.12)$$

Based on the KKT conditions, partial derivative of the Lagrangian function with respect to $P_{t,\phi}^{sub}$

must be zero at the optimum point, as shown in (13). $P_{t,\phi}^{sub}$ only exists in terms $f(\mathrm{x}^{dr}, \mathrm{x}^{es}, \mathrm{x}^{ev}, \mathrm{x}^{ddg})$ and $(\boldsymbol{\lambda}^{pf})^{\mathsf{T}}\mathrm{g}(\mathrm{x}^{pf})$. Hence, the partial derivative of the other terms in the Lagrangian function with respect to $P_{t,\phi}^{sub}$ would be null.

$$\frac{\partial \mathbf{L}}{\partial P_{t,\phi}^{sub}} = \frac{\partial f(\mathrm{x}^{dr}, \mathrm{x}^{es}, \mathrm{x}^{ev}, \mathrm{x}^{ddg})}{\partial P_{t,\phi}^{sub}} + \frac{\partial((\boldsymbol{\lambda}^{pf})^{\mathsf{T}}\mathrm{g}(\mathrm{x}^{pf}))}{\partial P_{t,\phi}^{sub}} = 0 \tag{7.13}$$

Let $\lambda_{t,n,\phi}^{(11a)}$ be the dual variable of (7.11a) and $\lambda_t^{(11i)_1}$, $\lambda_t^{(11i)_2}$, $\lambda_t^{(11i)_3}$ be corresponding dual variables of three sets of equations in (7.11i), where $\boldsymbol{\lambda}^{pf}=\left(\lambda_{n,t,A}^{(11a)}, \ldots, \lambda_t^{(11k)}\right)^{\mathsf{T}}$. Substituting $\phi=\{A, B, C\}$ in (7.13) results in (7.14)-(7.16):

$$\frac{\partial \mathbf{L}}{\partial P_{t,A}^{sub}} = \pi_t^e - \lambda_{1,t,A}^{(11a)} - \lambda_t^{(11i)_1} - \lambda_t^{(11i)_2} = 0 \tag{7.14}$$

$$\frac{\partial \mathbf{L}}{\partial P_{t,B}^{sub}} = \pi_t^e - \lambda_{1,t,B}^{(11a)} + \lambda_t^{(11i)_1} - \lambda_t^{(11i)_3} = 0 \tag{7.15}$$

$$\frac{\partial \mathbf{L}}{\partial P_{t,C}^{sub}} = \pi_t^e - \lambda_{1,t,C}^{(11a)} + \lambda_t^{(11i)_2} + \lambda_t^{(11i)_3} = 0 \tag{7.16}$$

By summating both sides of (7.14)-(7.16) and then dividing by 3, the following equation is obtained:

$$\pi_t^e = \frac{\lambda_{1,t,A}^{(11a)} + \lambda_{1,t,B}^{(11a)} + \lambda_{1,t,C}^{(11a)}}{3} = \frac{LMP_{1,t,A} + LMP_{1,t,B} + LMP_{1,t,C}}{3} \tag{7.17}$$

The ISO's payment, C^{WM}, is calculated as follows:

$$C^{WM} = \left(P_{t,A}^{sub} + P_{t,B}^{sub} + P_{t,C}^{sub}\right)\pi_t^e \tag{7.18}$$

By using (7.11i) and (7.17):

$$C^{WM} = 3P_{t,A}^{sub}\frac{LMP_{1,t,A} + LMP_{1,t,B} + LMP_{1,t,C}}{3} \tag{7.19}$$

$$= P_{t,A}^{sub}LMP_{1,t,A} + P_{t,B}^{sub}LMP_{1,t,B} + P_{t,C}^{sub}LMP_{1,t,C} \tag{7.20}$$

Hence, ISO's payment using the wholesale market price is the same as using D-LMP for each phase at the substation. Following similar approaches, the ISO's capacity-up/down payment using wholesale prices are also proven to be the same as using DSO's single-phase retail market prices.

Lemma 1 is extendable to every balanced DSO market participant. When there is no congestion or

voltage violation in the distribution system, a balanced three-phase aggregator will be paid at three single-phase D-LMPs. The average of these three D-LMPs is the same as the wholesale LMP at the ISO-DSO coupling substation. Therefore, when participating in the DSO market or in the existing ISO market directly, this three-phase aggregator will receive the same payment. When congestions and voltage violations happen in the DSO, D-LMPs across the distribution system will be different, and the DSO will receive a surplus. This surplus is conceptually similar to the ISO's congestion revenue rights (CRRs) [104, 108] and can be returned to the distribution utilities who are responsible for operating and upgrading the distribution circuits, reactive power compensations, and meters.

7.6 Case Studies

To investigate the market clearing performance and market outcomes of the proposed DSO, case studies are performed on 33-node and 240-node distribution systems. Studies are performed on a 24 hours operating timespan, where T={1,2,3,…,24}. In all case studies, the energy and regulation capacity prices in [109] are considered. The hourly factors in [110] are used to generate hourly prices. Hourly energy prices, capacity up/down prices, and hourly regulation signals are given in [102]. It is assumed that EVs are available between hours 16 to 24, where T'={16,17,18,…,24}. S^{up} and S^{dn} are assumed to be equal to 1. Voltage limit is considered to be 5%. Studies for cases with stricter voltage limits are not included due to the lack of space. For the sake of simplicity, the REAG production profile is considered deterministic with two production levels (high and low) and zero production cost. The probabilistic modeling of the REAG is out of scope of this chapter and is discussed in [103].

7.6.1 33-node Distribution System

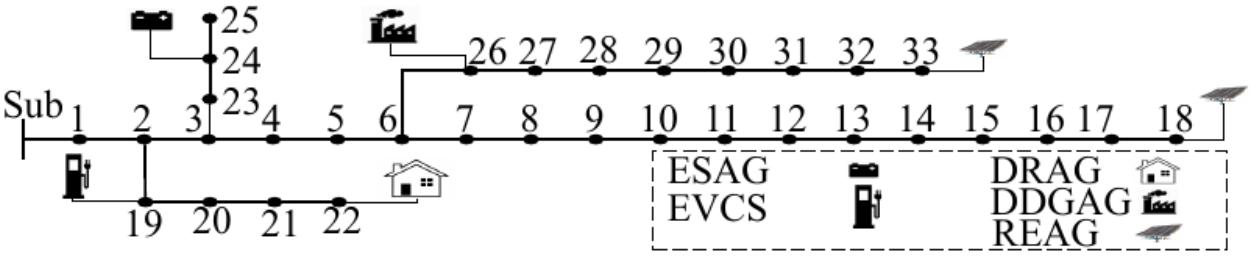

Figure 7.2 33-nodes distribution system.

The 33-node test system is a balanced radial network which is shown in Figure 8.2. The system contains 33 nodes, N={1,…,33}; 32 branches, J={1,…,32}; a DRAG, K_1={1}; an ESAG, K_2={2}; an EVCS, K_3={3}; a DDGAG, K_4={4}; two REAGs, K_5={5,6}. The test system data and load data are given in [111]. The two REAGs are considered to have identical energy production profile: 0.5 MW for hours 6-12 and 17-21; 0.4 MW for the remaining hours. The following parameters are assumed: $\eta_{k_2}^{ch}$=$\eta_{k_2}^{di}$=$\gamma_{k_3}^{ch}$=1, $\overline{P}_{k_1}$=1MW, $\overline{r}_{k_1}^{up}$=$\overline{r}_{k_1}^{dn}$=0.1MW, E_{k_2}=0.5MWh, $\overline{E}_{k_2}$=3MWh, $\overline{D}_{k_2}$=$\overline{C}_{k_2}$=$\overline{r}_{k_2}^{up}$ =$\overline{r}_{k_2}^{dn}$=1MW, $E_{k_3}^{int}$=0.2MWh, $\overline{R}_{k_3}^{c}$=0.5MW, $\overline{r}_{k_3}^{up}$=$\overline{r}_{k_3}^{dn}$=0.2MW, $\overline{CL}_{k_3}$=1MWh, $\underline{P}_{k_4}$=0 MW, $\overline{P}_{k_4}$=3MW, $\overline{r}_{k_4}^{up}$=$\overline{r}_{k_4}^{dn}$=0.5MW.

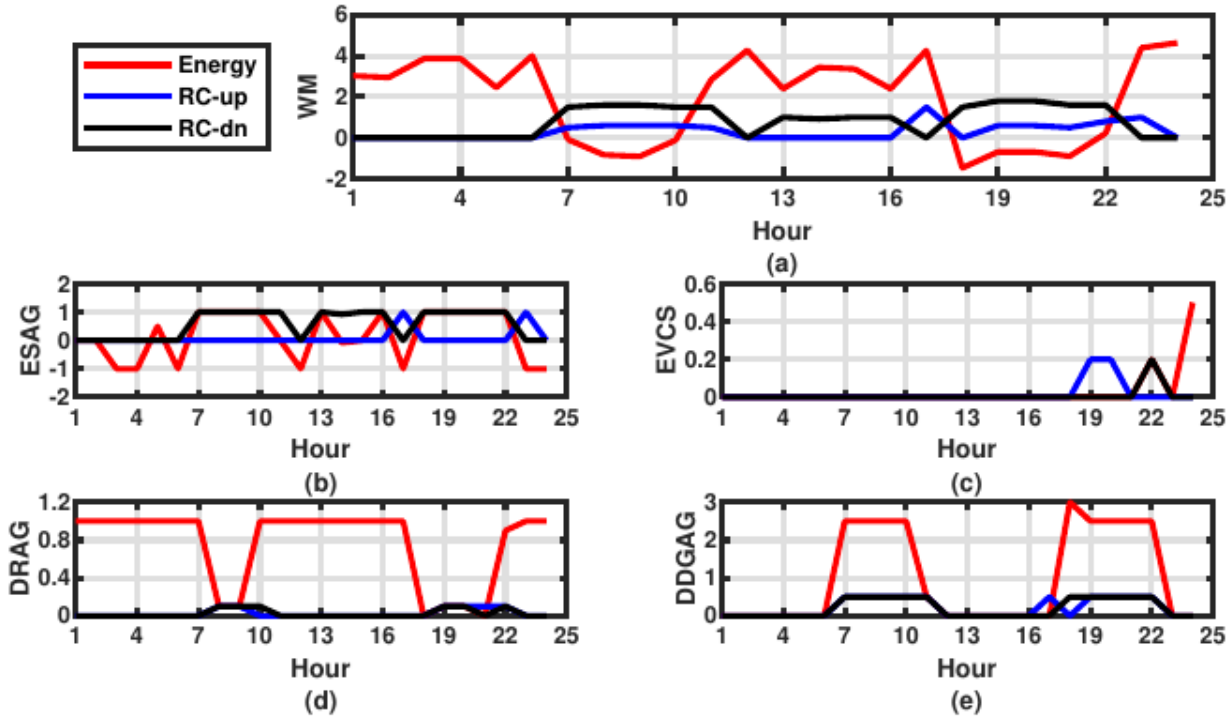

Figure 7.3 Hourly assigned energy, regulation capacity-up/-down services for the wholesale market (denoted by WM) and various aggregators for the 33-node system. The red, blue, and black curves denote awarded energy, regulation capacity-up/-down services, respectively. All Y-axis units are in MW.

Figure 7.3 shows the share of each market participant. The amount of energy/regulation bought/sold by the DSO from/to the ISO is shown in Figure 7.3(a). The awarded market share to the ESAG, EVCS, DRAG, and DDGAG is shown in Figure 7.3(b)-Figure 7.3(e), respectively. The DSO sells energy to the wholesale market at hours 8, 9, 18, 19, 20, and 21, during which the wholesale energy prices are high.

The DSO intends to assign regulation capacity-down more than regulation capacity-up to the ESAG since this could increase the ESAG's charge level which eventually contributes to lowering the total DSO operating cost by purchasing extra low-cost energy service from the ESAG.

The EVCS is assigned to provide regulation capacity-up at hours 19-20 since: 1) the wholesale capacity-up price is higher than the EVCS's capacity-up offering price, and 2) providing regulation capacity-up increases the charge level of EVCS.

At peak hours 8-9 and 18-21, the DRAG's offering price for buying energy is lower than that of the wholesale market. As a result, the wholesale market wins all the energy at these hours. However, the DRAG's regulation capacity offering price is lower than the wholesale market offering price for regulation capacity. Hence, the DSO assigns energy consumption equal to the regulation capacity-down provision to the DRAG that is necessary for providing regulation capacity-down.

The DSO assigns energy and regulation capacity provision to the DDGAG at peak hours 7-11 and 18-22, when the DDGAG's offering price is lower than wholesale price. The DSO intends to assign regulation capacity before assigning energy to the DDGAG at these hours since the wholesale regulation capacity price is higher than wholesale energy price. The DDGAG provides regulation at its maximum regulation capacity (0.5 MW). The DSO assigns its remaining capacity (2.5 MW) to energy provision. However, at hour 18, the DSO assigns energy provision to the DDGAG at its maximum capacity (3 MW), since at this hour, the wholesale energy price is higher than the wholesale regulation capacity price.

7.6.2 240-node Distribution System

The 240-node distribution test system is an unbalanced radial network in Midwest U.S. The system is fully observable with smart meters. The data of the system is given in [112].

The system contains 240 nodes, where N={1,…,240}; 239 branches, where J={1,…,239}. Multiple aggregators are considered as follows: ten DRAGs, where K_1={1,…,10}; two ESAGs, where K_2={11,12}; five EVCSs, where K_3={13,…,17}; ten DDGAGs, where K_4={18,…,27}; six REAGs, where K_5={28,…,33}.

Different offering prices are considered for individual aggregators of each type. Let π_{k_1}, π_{k_2}, π_{k_3}, and π_{k_4} be the offering prices for DRAG, ESAG, EVCS, and DDGAG in the 33-node test case, respectively. In this 240-node test case, the offering prices for DRAGs, ESAGs, EGCSs, and DDGAGs are random numbers generated between $0.9\pi_{k_1}$ and $1.08\pi_{k_1}$, π_{k_2} and $1.03\pi_{k_2}$, π_{k_3} and $1.12\pi_{k_3}$, $0.9\pi_{k_4}$ and $1.08\pi_{k_4}$, respectively.

The ESAGs and EVCSs are assumed to be identically allocated on each phase with the following parameters: $\eta_{k_2}^{ch}$=$\eta_{k_2}^{di}$=$\gamma_{k_3}^{ch}$=1, E_{k_2}=0.1 MWh, $\overline{E}_{k_2}$=0.8 MWh, $\overline{D}_{k_2}$=$\overline{C}_{k_2}$=$\overline{r}_{k_2}^{up}$=$\overline{r}_{k_2}^{dn}$=0.4 MW, $E_{k_3}^{int}$=0.2 MWh, $\overline{R}_{k_3}^{c}$=0.2 MW, $\overline{r}_{k_3}^{up}$=$\overline{r}_{k_3}^{dn}$=0.1 MW, $\overline{CL}_{k_3}$=0.5 MWh. The DDGAGs are assumed to be single phase with regulation limit of 0.1 MW and the following characteristics: the 1st, 2nd, 7th, and 8th DDGAGs have the capacity of 0.25 MW on phase A, the 3rd, 4th, and 9th DDGAGs have the capacity of 0.25 MW on phase B, and the 5th, 6th, and 10th DDGAGs have the capacity of 0.25 MW on phase C. The DRAGs are assumed to be single-phase with regulation limit of 0.05 MW and the capacity of 0.15 MW. The phase allocations of the ten DRAGs are the same as those of the ten DDGAGs. The REAGs are assumed to be single-phase with identical energy production profile of 0.15 MW for hours 6-12 and 17-21; 0.1 MW for remaining hours with the following phase allocation: the 1st and 2nd REAGs on phase A; the 3rd and 4th REAGs on phase B; and the 5th and 6th REAGs on phase C.

Figure 7.4 shows the energy market outcomes of the 240-node system. Figure 7.4(a), Figure 7.4(b), and Figure 7.4(c) show the DSO's wholesale market share on phases A, B, C, respectively. Although the DSO's retail market is unbalanced, the DSO's wholesale market share is three-phase balanced. By comparing market outcomes in the two test systems, one can see that the wholesale market buys less energy from the 240-node DSO than from the 33-node DSO, since retail market participants in the 240-node DSO have higher offering prices, therefore the 240-node DSO buys

energy from the ISO during most hours.

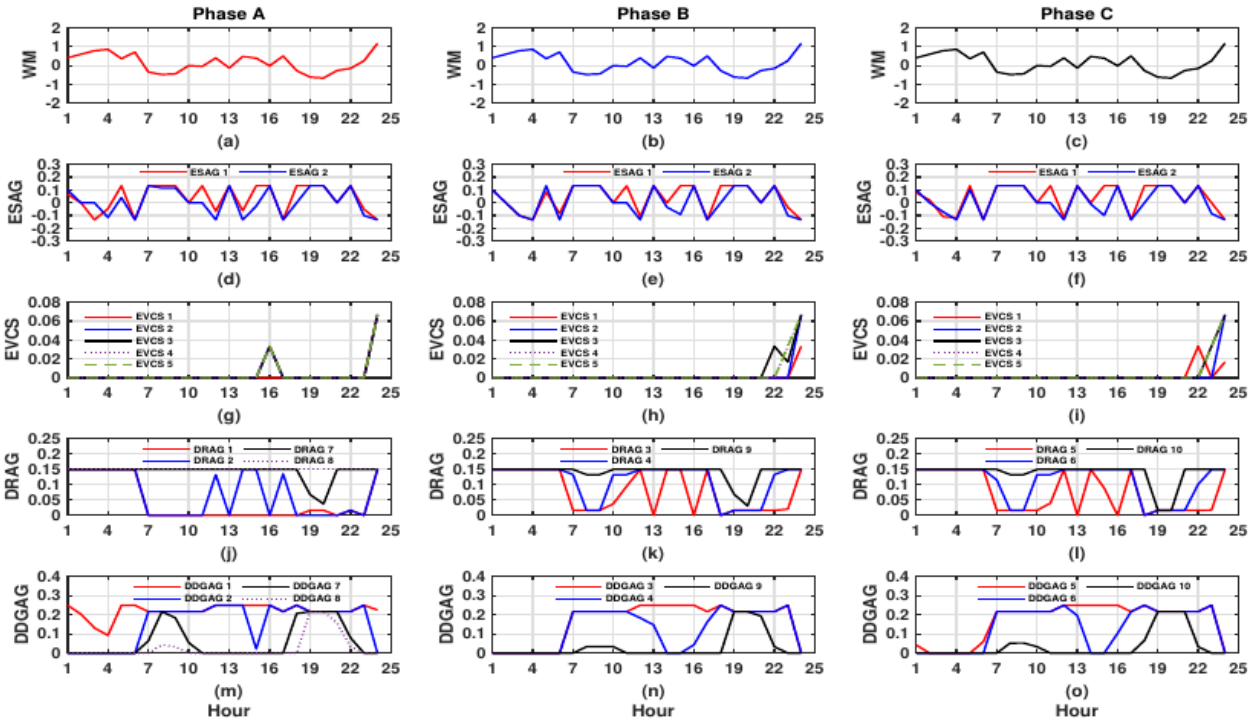

Figure 7.4 Hourly awarded quantities for the wholesale market (denoted by WM) and various aggregators for each phase in the wholesale and retail energy markets for the 240-node system. All Y-axis units are in MW.

The market share of ESAGs on phases A, B, and C is shown in Figure 7.4(d), Figure 7.4(e), and Figure 7.4(f), respectively. The DSO assigns more charging states to the 2nd ESAG than to the 1st ESAG since the 2nd ESAG's energy offering price is higher than that of the 1st ESAG. This phenomenon can be observed by comparing their curves as the 2nd ESAG's curve is under the 1st ESAG's curve for most of the time.

The market share of EVCSs on phases A, B, and C is shown in Figure 7.4(g), 7.4(h), and 7.4(i), respectively. The 5th EVCS consumes more energy than other EVCSs, since its offering price for buying energy is the highest among all EVCSs.

The share of DRAGs on phases A, B, and C is shown in Figure 7.4(j), Figure 7.4(k), and Figure 7.4(l), respectively. By comparing the share of 1st, 2nd, 7th, 8th DRAGs (all of which have demand response resources on phase A), one can see that the 8th DRAG consumes energy more than the others since its offering price for buying energy is higher than that of the others. Hence, the DSO sells more energy to the 8th DRAG. Similarly, among all the DRAGs with resources on phase B (and C), the 9th (and 10th) DRAG with the highest energy offering price on phase B (and C) consumes the most energy, respectively.

The market share of DDGAGs on phases A, B, and C is shown in Figure 7.4(m), Figure 7.4(n), and Figure 7.4(o), respectively. The offering price of the 1st DDGAG is lower than other three

DDGAGs on phase A. Hence, the DSO assigns the most energy provision to the 1st DDGAG among all DDGAGs on phase A. Figure 7.4(n) (and Figure 7.4(o)) shows similar results for the DDGAGs on phase B (and phase C).

7.6.3 Market Settlement

Table 7.1 LMP forecasting errors in Case 2

Cost ($)	Market participant						
	WM	ESAGs	DDGAGs	EVCSs	DRAGs	REAGs	IL
33-node	-1192.2	-157.8	-715.2	18.5	488.6	-603.4	2161.5
240-node	-221.2	-122.0	-789.3	33.8	684.3	-505.9	920.3

The costs of various market participants for buying/selling energy and regulation services in the DSO market in both 33-node and 240-node systems are given in Table. 7.1, where WM and IL denote the wholesale market and the inelastic load, respectively. In the 240-node system, the costs for aggregators of the same type are summed up together. It is clear that the summation of all the costs in each system is zero, leading to no surplus for the DSO when the retail market is cleared.

7.7 Conclusion

This chapter proposed a comprehensive DSO framework for market participation of DER aggregators in the three-phase unbalanced distribution network. Various kinds of DER aggregators were modeled. A three-phase unbalanced linearized power flow was introduced to consider unbalanced operating conditions in the distribution system. The retail market settlement procedure was discussed. At the wholesale-DSO coupling substation, the total payment received or compensated by the DSO under the wholesale price is identical to that under three single-phase D-LMPs for each phase at the substation.

Case studies were performed on the 33-node balanced distribution system and the 240-node unbalanced distribution system. The results in the balanced network show that the DSO sells energy to the wholesale market when the wholesale energy price is high. The DSO assigns regulation capacity- down services to the ESAG for increasing its charge level and decreasing DSO's operating cost. The DDGAG is cleared to sell energy during peak hours. There are opportunities for the EVCS to increase its charge level by providing regulation capacity-up. The DRAG purchases energy during off-peak hours. The results in the unbalanced system show that although the DSO's retail market is unbalanced, the DSO's share for participating in the wholesale market is three-phase balanced. The DSO assigns more charging states to the ESAGs with higher energy offering prices. In the unbalanced system, the DSO may buy energy from the DDGAG with higher energy offering price to submit a balanced offer to the ISO. The DSO sells energy to DRAGs and EVCSs considering achieving balanced operating conditions at the DSO-ISO coupling point.

8. Conclusions

This project aims at resolving market operation and participation challenges caused by the growing integration of utility-scale and distributed energy storage resources in both transmission and distribution systems. The report focuses on three core areas: 1) understanding market participation activities of utility-scale batteries in the wholesale energy, reserve, and regulation markets; 2) data-driven day-ahead and real-time price forecasting approaches for profit-seeking utility-scale batteries and aggregators of distributed batteries; and 3) the distribution system operator (DSO) framework for coordinating market participation activities of distributed batteries and other distributed resources. The following works are presented in this report.

- A comprehensive modeling framework is proposed for studying various market participation activities and operating patterns of utility-scale batteries in the energy and ancillary services markets, with detailed consideration of batteries' regulation market participation models and degradation cost models. Analysis on the impact of battery degradation on market participation strategies of utility-scale batteries is performed.
- A short-term decision model for an electricity retailer with BESSs and virtual bidding was proposed through a two-stage stochastic optimization framework. Case studies have shown that the integration of BESS contributed to the reduction of the retailer's cost and CVaR for different risk-aversion levels.
- Data-driven price forecasting approaches with improved forecasting accuracy are proposed, which allow profit-seeking battery owners and aggregators to forecast system-wide day-ahead and real-time locational marginal prices using public market data. The proposed approaches are built upon generative adversarial networks and convolutional long short-term memory networks which capture the spatio-temporal correlations among system-wide energy market data.
- A DSO framework is proposed to optimally coordinate the aggregators of various distributed resources for their wholesale market participation while operating the retail market, considering three-phase unbalanced distribution system operating constraints, as well as coordinated market clearing mechanisms between the balanced wholesale and unbalanced retail markets.

References

[1] Radovanovic, T. Nesti, and B. Chen, "A holistic approach to forecasting wholesale energy market prices," IEEE Transactions on Power Systems, pp. 1–1, 2019.

[2] S. Shafiee, P. Zamani-Dehkordi, H. Zareipour, and A. M. Knight, "Economic assessment of a price-maker energy storage facility in the alberta electricity market," Energy, vol. 111, pp. 537–547, 2016.

[3] H. Cui, F. Li, X. Fang, H. Chen, and H. Wang, "Bilevel arbitrage potential evaluation for grid- scale energy storage considering wind power and lmp smoothing effect," IEEE Transactions on Sustainable Energy, vol. 9, no. 2, pp. 707–718, 2017.

[4] P. Zou, Q. Chen, Q. Xia, G. He, and C. Kang, "Evaluating the contribution of energy storages to support large-scale renewable generation in joint energy and ancillary service markets," IEEE Transactions on Sustainable Energy, vol. 7, no. 2, pp. 808–818, 2015.

[5] J.-F. Toubeau, J. Bottieau, Z. De Greve, F. Vallee, and K. Bruninx, "Data-driven scheduling of energy storage in day-ahead energy and reserve markets with probabilistic guarantees on real-time delivery," IEEE Transactions on Power Systems, 2020.

[6] Q. Huang, Y. Xu, T. Wang, and C. A. Courcoubetis, "Market mechanisms for cooperative operation of price-maker energy storage in a power network," IEEE Transactions on Power Systems, vol. 33, no. 3, pp. 3013–3028, 2018.

[7] H. Mohsenian-Rad, "Coordinated price-maker operation of large energy storage units in nodal energy markets," IEEE Transactions on Power Systems, vol. 31, no. 1, pp. 786–797, 2015.

[8] E. Nasrolahpour, J. Kazempour, H. Zareipour, and W. D. Rosehart, "A bilevel model for participation of a storage system in energy and reserve markets," IEEE Transactions on Sustainable Energy, vol. 9, no. 2, pp. 582–598, 2018.

[9] J. Arteaga and H. Zareipour, "A price-maker/price-taker model for the operation of battery storage systems in electricity markets," IEEE Transactions on Smart Grid, vol. 10, no. 6, pp. 6912–6920, 2019.

[10] H. Ding, P. Pinson, Z. Hu, J. Wang, and Y. Song, "Optimal offering and operating strategy for a large wind-storage system as a price maker," IEEE Transactions on Power Systems, vol. 32, no. 6, pp. 4904–13, 2017.

[11] R. Khalilisenobari and M. Wu, "Optimal participation of price-maker battery energy storage systems (BESSs) in energy, reserve and pay as performance regulation markets," in 51st North American power symposium (NAPS), vol. 1, 2019, pp. 1–6.

[12] Y. Chen, Y. Wang, D. Kirschen, and B. Zhang, "Model-free renewable scenario generation using generative adversarial networks," IEEE Transactions on Power Systems, vol. 33, no. 3, pp. 3265–3275, May 2018.

[13] Y. Chen, X. Wang, and B. Zhang, "An unsupervised deep learning approach for scenario forecasts," in 2018 Power Systems Computation Conference (PSCC), June 2018, pp. 1–7.

[14] X. Geng and L. Xie, "A data-driven approach to identifying system pattern regions in market operations," in 2015 IEEE Power Energy Society General Meeting, July 2015, pp. 1–5.

[15] ——, "Learning the lmp-load coupling from data: A support vector machine based approach," IEEE Transactions on Power Systems, vol. 32, no. 2, pp. 1127–1138, March 2017.

[16] S. K. Aggarwal, L. M. Saini, and A. Kumar, "Electricity price forecasting in deregulated markets: A review and evaluation," International Journal of Electrical Power & Energy Systems, vol. 31, pp. 13 – 22, 2009.

[17] Federal Energy Regulatory Commission, "Order no. 841. electric storage participation in markets operated by regional transmission organizations and independent system operators," February 2018.

[18] "Battery Storage in the United States: An Update on Market Trends," U.S. Energy Information Administration, Tech. Rep., July 2020.

[19] "Electricity storage and renewables: costs and markets to 2030," International Renewable Energy Agency (IRENA), Tech. Rep., October 2017.

[20] IHS Markit, "As frequency regulation markets across europe saturate, new installations will be driven by new market opportunities and battery energy storage systems adding new sources of revenue." https://rb.gy/lxk6ei, 2020.

[21] "Battery energy storage technology overview and co-op case studies," NRECA, Tech. Rep., June 2019.

[22] H. Mohsenian-Rad, "Optimal bidding, scheduling, and deployment of battery systems in california day-ahead energy market," IEEE Transactions on Power Systems, vol. 31, no. 1, pp. 442–453, 2015.

[23] G. He, Q. Chen, C. Kang, P. Pinson, and Q. Xia, "Optimal bidding strategy of battery storage in power markets considering performance-based regulation and battery cycle life," IEEE Transactions on Smart Grid, vol. 7, no. 5, pp. 2359–2367, 2016.

[24] Y. Shi, B. Xu, D. Wang, and B. Zhang, "Using battery storage for peak shaving and frequency regulation: Joint optimization for superlinear gains," IEEE Transactions on Power Systems, vol. 33, no. 3, pp. 2882–2894, 2018.

[25] M. Kazemi and H. Zareipour, "Long-term scheduling of battery storage systems in energy and regulation markets considering battery's lifespan," IEEE Transactions on Smart Grid, vol. 9, no. 6, pp. 6840–6849, 2018.

[26] M. Kazemi, H. Zareipour, N. Amjady, W. D. Rosehart, and M. Ehsan, "Operation scheduling of battery storage systems in joint energy and ancillary services markets," IEEE Transactions on Sustainable Energy, vol. 8, no. 4, pp. 1726–1735, 2017.

[27] B. Xu, J. Zhao, T. Zheng, E. Litvinov, and D. S. Kirschen, "Factoring the cycle aging cost of batteries participating in electricity markets," IEEE Transactions on Power Systems, vol. 33, no. 2, pp. 2248–59, 2017.

[28] N. Padmanabhan, M. Ahmed, and K. Bhattacharya, "Battery energy storage systems in energy and reserve markets," IEEE Transactions on Power Systems, 2019.

[29] G. He, S. Kar, J. Mohammadi, P. Moutis, and J. Whitacre, “Power system dispatch with marginal degradation cost of battery storage,” IEEE Transactions on Power Systems, 2020.

[30] S. A. Gabriel, A. J. Conejo, J. D. Fuller, B. F. Hobbs, and C. Ruiz, Complementarity modeling in energy markets. Springer Science & Business Media, 2012, vol. 180, p. 250.

[31] A. Sadeghi-Mobarakeh and H. Mohsenian-Rad, “Optimal bidding in performance-based regulation markets: An mpec analysis with system dynamics,” IEEE Transactions on Power Systems, vol. 32, no. 2, pp. 1282–1292, 2017.

[32] K. Bruninx, Y. Dvorkin, E. Delarue, H. Pandžić, W. D’haeseleer, and D. S. Kirschen, “Coupling pumped hydro energy storage with unit commitment,” IEEE Transactions on Sustainable Energy, vol. 7, no. 2, pp. 786–796, 2015.

[33] “California independent system operator corporation, fifth replacement FERC electric tariff,” December 2020. [Online]. Available: https://rb.gy/5b68aq

[34] C. Barrows, A. Bloom, A. Ehlen, J. Ikaheimo, J. Jorgenson, D. Krishnamurthy, J. Lau, B. McBennett, M. O’Connell, E. Preston et al., “The ieee reliability test system: A proposed 2019 update,” IEEE Transactions on Power Systems, 2019.

[35] “Simulated Automatic Generator Control (AGC) Setpoint Data.” [Online]. Available: https://rb.gy/flegf8

[36] “PJM market data.” [Online]. Available: https://rb.gy/066puv

[37] “Lithium-ion batteries for large-scale grid energy storage,” April 2018. [Online]. Available: https://rb.gy/5bnric

[38] R. Fu, T. W. Remo, and R. M. Margolis, “2018 us utility-scale photovoltaics-plus-energy storage system costs benchmark,” National Renewable Energy Lab.(NREL), Golden, CO, US, Tech. Rep., 2018.

[39] Laresgoiti, S. Käbitz, M. Ecker, and D. U. Sauer, “Modeling mechanical degradation in lithium ion batteries during cycling: Solid electrolyte interphase fracture,” Journal of Power Sources, vol. 300, pp. 112–122, 2015.

[40] Amzallag, J. Gerey, J. L. Robert, and J. Bahuaud, “Standardization of the rainflow counting method for fatigue analysis,” International journal of fatigue, vol. 16, no. 4, pp. 287–293, 1994.

[41] R. Khalilisenobari and M. Wu, “Impact of battery degradation on market participation of utility-scale batteries: Case studies,” in 52nd North American Power Symposium (NAPS), April 2021. Accepted to appear.

[42] “U.S. Battery Storage Market Trends,” U.S. Energy Information Administration, Tech. Rep., May 2018.

[43] R. Khalilisenobari and M. Wu, “Optimal participation of price-maker battery energy storage systems in energy and ancillary services markets considering degradation cost,” arXiv preprint arXiv:2006.05659, 2020.

[44] M. Mousavi and M. Wu, “A DSO framework for comprehensive market participation of DER aggregators,” arXiv preprint arXiv:2006.06673, 2020.

[45] B. Xu, Y. Dvorkin, D. S. Kirschen, C. A. Silva-Monroy, and J.-P. Watson, "A comparison of policies on the participation of storage in us frequency regulation markets," in 2016 IEEE Power and Energy Society General Meeting (PESGM). IEEE, 2016, pp. 1–5.

[46] C. Schweppe, Spot pricing of electricity / by Fred C. Schweppe ... [et al.]. Kluwer Academic Boston, 1988.

[47] V. Kekatos, G. B. Giannakis, and R. Baldick, "Online energy price matrix factorization for power grid topology tracking," IEEE Transactions on Smart Grid, vol. 7, no. 3, pp. 1239–1248, 2016.

[48] Q. Zhou, L. Tesfatsion, and C. Liu, "Short-term congestion forecasting in wholesale power markets," IEEE Transactions on Power Systems, vol. 26, no. 4, pp. 2185–2196, 2011.

[49] G. Hamoud and I. Bradley, "Assessment of transmission congestion cost and locational marginal pricing in a competitive electricity market," IEEE Transactions on Power Systems, vol. 19, no. 2, pp. 769–775, May 2004.

[50] W. Deng, Y. Ji, and L. Tong, "Probabilistic forecasting and simulation of electricity markets via online dictionary learning," 2016.

[51] J. F. Toubeau, T. Morstyn, J. Bottieau, K. Zheng, D. Apostolopoulou, Z. De Grève, Y. Wang, and F. Vallée, "Capturing spatio-temporal dependencies in the probabilistic forecasting of distribution locational marginal prices," IEEE Transactions on Smart Grid, pp. 1–1, 2020.

[52] Y. Ji, R. J. Thomas, and L. Tong, "Probabilistic forecasting of real-time lmp and network congestion," IEEE Transactions on Power Systems, vol. 32, no. 2, pp. 831–841, March 2017.

[53] J. P. González, A. M. S. Roque, and E. A. Pérez, "Forecasting functional time series with a new hilbertian armax model: Application to electricity price forecasting," IEEE Transactions on Power Systems, vol. 33, no. 1, pp. 545–556, Jan 2018.

[54] Z. Zhao, C. Wang, M. Nokleby, and C. J. Miller, "Improving short-term electricity price forecasting using day-ahead lmp with arima models," in 2017 IEEE Power Energy Society General Meeting, July 2017, pp. 1–5.

[55] L. Wang, Z. Zhang, and J. Chen, "Short-term electricity price forecasting with stacked denoising autoencoders," IEEE Transactions on Power Systems, vol. 32, no. 4, pp. 2673–2681, 2017.

[56] Ziel, "Forecasting electricity spot prices using lasso: On capturing the autoregressive intraday structure," IEEE Transactions on Power Systems, vol. 31, no. 6, pp. 4977–4987, 2016.

[57] K. Zheng, Y. Wang, K. Liu, and Q. Chen, "Locational marginal price forecasting: A componential and ensemble approach," IEEE Transactions on Smart Grid, vol. 11, no. 5, pp. 4555–4564, 2020.

[58] O. Abedinia, N. Amjady, and H. Zareipour, "A new feature selection technique for load and price forecast of electrical power systems," IEEE Transactions on Power Systems, vol. 32, no. 1, pp. 62–74, 2017.

[59] O. Abedinia, N. Amjady, M. Shafie-khah, and J. Catalão, "Electricity price forecast using combinatorial neural network trained by a new stochastic search method," Energy Conversion and Management, vol. 105, pp. 642–654, 2015. [Online]. Available: https://www.sciencedirect.com/science/article/pii/S0196890415007712

[60] Y. Ma, P. Luh, K. Kasiviswanathan, and E. Ni, "A neural network-based method for forecast- ing zonal locational marginal prices," in IEEE Power Engineering Society General Meeting, 2004., 2004, pp. 296–302 Vol.1.

[61] X. Fang, B.-M. Hodge, E. Du, C. Kang, and F. Li, "Introducing uncertainty components in locational marginal prices for pricing wind power and load uncertainties," IEEE Transactions on Power Systems, vol. 34, no. 3, pp. 2013–2024, 2019.

[62] F. Ziel and R. Weron, "Day-ahead electricity price forecasting with high-dimensional structures: Univariate vs. multivariate modeling frameworks," Energy Economics, vol. 70, p. 396–420, Feb 2018. [Online]. Available: http://dx.doi.org/10.1016/j.eneco.2017.12.016

[63] Z. Zhang and M. Wu, "Real-time locational marginal price forecasting using generative adversarial network," in 2020 IEEE SmartGridComm Conference, 2020.

[64] J. Goodfellow, J. Pouget-Abadie, M. Mirza, B. Xu, D. Warde-Farley, S. Ozair, A. Courville, and Y. Bengio, "Generative adversarial networks," 2014.

[65] "Spp data," 2020. [Online]. Available: https://marketplace.spp.org/

[66] V. Dumoulin and F. Visin, "A guide to convolution arithmetic for deep learning," 2018.

[67] A. Radford, L. Metz, and S. Chintala, "Unsupervised representation learning with deep convolutional generative adversarial networks," 2015.

[68] M. Mathieu, C. Couprie, and Y. LeCun, "Deep multi-scale video prediction beyond mean square error," 2015.

[69] E. Denton, S. Chintala, A. Szlam, and R. Fergus, "Deep generative image models using a laplacian pyramid of adversarial networks," 2015.

[70] X. Zhou, Z. Pan, G. Hu, S. Tang, and C. Zhao, "Stock market prediction on high-frequency data using generative adversarial nets," Mathematical Problems in Engineering, vol. 2018, pp. 1–11, 04 2018.

[71] M. Claesen and B. D. Moor, "Hyperparameter search in machine learning," 2015.

[72] W. Polasek, "Time series analysis and its applications: With r examples, third edition by robert h. shumway, david s. stoffer," International Statistical Review, vol. 81, no. 2, pp. 323–325, 2013.

[73] MATLAB, "Estimate parameters of armax model," 2019. [Online]. Available: https://www.mathworks.com/help/ident/ref/armax.html

[74] "Tensorflow," 2019. [Online]. Available: https://www.tensorflow.org/

[75] Y.Chen, "A new methodology of spatial cross-correlation analysis," PLOS ONE, vol. 10, no. 5, p. e0126158, May 2015. [Online]. Available: http://dx.doi.org/10.1371/journal.pone.0126158

[76] "Miso market data," 2020. [Online]. Available: https://www.misoenergy.org/ markets-and-operations/real-time--market-data/market-reports/

[77] R. C. Garcia, J. Contreras, M. van Akkeren, and J. B. C. Garcia, "A garch forecasting model to predict day-ahead electricity prices," IEEE Transactions on Power Systems, vol. 20, no. 2, pp. 867–874, May 2005.

[78] K. Hubicka, G. Marcjasz, and R. Weron, "A note on averaging day-ahead electricity price forecasts across calibration windows," IEEE Transactions on Sustainable Energy, vol. 10, no. 1, pp. 321–323, 2019.

[79] Y. Zhu, R. Dai, G. Liu, Z. Wang, and S. Lu, "Power market price forecasting via deep learning," in IECON 2018 - 44th Annual Conference of the IEEE Industrial Electronics Society, 2018, pp. 4935–4939.

[80] "Short-term forecast for locational marginal pricing (lmp) data sets," in 2018 North American Power Symposium (NAPS), 2018, pp. 1–5.

[81] X. Shi, Z. Chen, H. Wang, D.-Y. Yeung, W. kin Wong, and W. chun Woo, "Convolutional lstm network: A machine learning approach for precipitation nowcasting," 2015.

[82] S. Hochreiter and J. Schmidhuber, "Long short-term memory," Neural computation, vol. 9, pp. 1735–80, 12 1997.

[83] "Iso new England real-time market data," 2020. [Online]. Available: https://www.iso-ne.com/isoexpress/

[84] Federal Energy Regulatory Commission, "Order no. 2222: Participation of distributed energy resource aggregations in markets operated by regional transmission organizations and independent system operators," 2020.

[85] Y. Chen, T. Zheng, X. Wang, and S. Oren, "Der market integration – opportunities and challenges," in Panel session at 2020 IEEE Power and Energy Society General Meeting, 2020.

[86] W. Warwick, T. Hardy, M. Hoffman, and J. Homer. (2016) Electricity distribution system baseline report. [Online]. Available: https://energy.gov/epsa/downloads/ electricity-distribution-system-baseline-report

[87] M. Di Somma, G. Graditi, and P. Siano, "Optimal bidding strategy for a der aggregator in the day-ahead market in the presence of demand flexibility," IEEE Trans. Ind. Electron., vol. 66, no. 2, pp. 1509–1519, Feb 2019.

[88] M. F. Anjos, A. Lodi, and M. Tanneau, "A decentralized framework for the optimal coordination of distributed energy resources," IEEE Trans. Power Syst., vol. 34, no. 1, pp. 349–359, Jan 2019.

[89] G. Liu, Y. Xu, and K. Tomsovic, "Bidding strategy for microgrid in day-ahead market based on hybrid stochastic/robust optimization," IEEE Trans. on Smart Grid, vol. 7, no. 1, pp. 227–237, Jan 2016.

[90] H. Xu, K. Zhang, and J. Zhang, "Optimal joint bidding and pricing of profit-seeking load serving entity," IEEE Trans. Power Syst., vol. 33, no. 5, pp. 5427–5436, Sep. 2018.

[91] H. T. Nguyen, L. B. Le, and Z. Wang, "A bidding strategy for virtual power plants with the intraday demand response exchange market using the stochastic programming," IEEE Trans. Ind. Appl., vol. 54, no. 4, pp. 3044–3055, July 2018.

[92] H. Yang, S. Zhang, J. Qiu, D. Qiu, M. Lai, and Z. Dong, "Cvar-constrained optimal bidding of electric vehicle aggregators in day-ahead and real-time markets," IEEE Trans. Ind. Informat., vol. 13, no. 5, pp. 2555–2565, Oct 2017.

[93] M. N. Faqiry, A. K. Zarabie, F. Nassery, H. Wu, and S. Das, "A day-ahead market energy auction for distribution system operation," in 2017 IEEE International Conference on Electro Information Technology (EIT), May 2017, pp. 182–187.

[94] P. Olivella-Rosell, E. Bullich-Massagué, M. Aragüés-Peñalba, A. Sumper, S. Ødegaard Ottesen, J.-A. Vidal-Clos, and R. Villafáfila-Robles, "Optimization problem for meeting distribution system operator requests in local flexibility markets with distributed energy resources," Applied Energy, vol. 210, pp. 881 – 895, 2018.

[95] C. do Prado, H. Vakilzadian, W. Qiao, and D. P. F. Möller, "Stochastic distribution system market clearing and settlement via sample average approximation," in 2018 North American Power Symposium (NAPS), Sep. 2018, pp. 1–6.

[96] S. Parhizi and A. Khodaei, "Interdependency of transmission and distribution pricing," in 2016 IEEE Power Energy Society Innovative Smart Grid Technologies Conference (ISGT), Sep. 2016, pp. 1–5.

[97] C. Bedoya, C. Liu, G. Krishnamoorthy, and A. Dubey, "Bilateral electricity market in a distribution system environment," IEEE Trans. Smart Grid, pp. 1–1, 2019.

[98] Bai, J. Wang, C. Wang, C. Chen, and F. Li, "Distribution locational marginal pricing (dlmp) for congestion management and voltage support," IEEE Trans. Power Syst., vol. 33, no. 4, pp. 4061–4073, July 2018.

[99] A. Hermann, J. Kazempour, S. Huang, and J. Østergaard, "Congestion management in distribution networks with asymmetric block offers," IEEE Trans. Power Syst., vol. 34, no. 6, pp. 4382–4392, Nov 2019.

[100] F. Shen, S. Huang, Q. Wu, S. Repo, Y. Xu, and J. Østergaard, "Comprehensive congestion management for distribution networks based on dynamic tariff, reconfiguration, and re-profiling product," IEEE Trans. Smart Grid, vol. 10, no. 5, pp. 4795–4805, Sep. 2019.

[101] D. Koraki and K. Strunz, "Wind and solar power integration in electricity markets and distribution networks through service-centric virtual power plants," IEEE Trans. Power Syst., vol. 33, no. 1, pp. 473–485, Jan 2018.

[102] M. Mousavi and M. Wu, "A dso framework for comprehensive market participation of der aggregators," in 2020 IEEE Power Energy Society General Meeting (PESGM), 2020, pp. 1–5.

[103] M. Mousavi and M. Wu, "A two-stage stochastic programming dso framework for comprehensive market participation of der aggregators under uncertainty," arXiv preprint arXiv:2009.08248, 2020.

[104] "California iso." [Online]. Available: https://goo.gl/bBGvVG

[105] B. Vatandoust, A. Ahmadian, M. A. Golkar, A. Elkamel, A. Almansoori, and M. Ghaljehei, "Risk-averse optimal bidding of electric vehicles and energy storage aggregator in day-ahead frequency regulation market," IEEE Trans. Power Syst., vol. 34, no. 3, pp. 2036–2047, May 2019.

[106] L. Gan and S. H. Low, "Convex relaxations and linear approximation for optimal power flow in multiphase radial networks," in 2014 Power Systems Computation Conference, Aug 2014, pp. 1–9.

[107] B. Chen, C. Chen, J. Wang, and K. L. Butler-Purry, "Sequential service restoration for unbalanced distribution systems and microgrids," IEEE Trans. Power Syst., vol. 33, no. 2, pp. 1507–1520, March 2018.

[108] E. Litvinov, F. Zhao, and T. Zheng, "Alternative auction objectives and pricing schemes in short-term electricity markets," in 2009 IEEE Power Energy Society General Meeting, 2009, pp. 1–11.

[109] D. Fooladivanda, H. Xu, A. D. Domínguez-García, and S. Bose, "Offer strategies for whole- sale energy and regulation markets," IEEE Trans. Power Syst., vol. 33, no. 6, pp. 7305–7308, Nov 2018.

[110] M. Mousavi, M. Rayati, and A. M. Ranjbar, "Optimal operation of a virtual power plant in frequency constrained electricity market," IET Gener. Transm. Distrib., vol. 13, no. 11, pp. 2123–2133, 2019.

[111] M. Mousavi, A. M. Ranjbar, and A. Safdarian, "Optimal dg placement and sizing based on micp in radial distribution networks," in 2017 Smart Grid Conference (SGC), 2017, pp. 1–6.

[112] F. Bu, Y. Yuan, Z. Wang, K. Dehghanpour, and A. Kimber, "A time-series distribution test system based on real utility data," arXiv preprint arXiv:1906.04078, 2019.

[113] Electric Choice. "Energy deregulation around the word: A comprehensive guide,". [Online]. Available: https://www.electricchoice.com/blog/energy-deregulation-world/

[114] L. M. Quilici, D. S. Powers, G. H. Therrien, B. O. Davis, and O. A. Prieto. (2019, July). Retail competition in electricity: What have we learned in 20 years? [Online]. Available: https://ceadvisors.com/wp-content/uploads/2019/07/AEPG-FINAL-report.pdf

[115] A. Swadley and. M. Yücel, "Did residential electricity rates fall after retail competition? A dynamic panel analysis," Energy Policy, vol. 39, no. 12, pp. 7702-7711, Dec. 2011.

[116] M. J. Morey and L. D. Kirsch, "Retail choice in electricity: What have we learned in 20 years?" Christensen Associates Energy Consulting LLC, Madison, WI, USA, Feb. 2016 [Online]. Available: https://hepg.hks.harvard.edu/publications/retail-choice-electricity-what-have-we-learned-20-years

[117] A. J. Conejo, M. Carrion, and J. M. Morales, Decision Making Under Uncertainty in Electricity Markets, 1st ed. New York, NY, USA: Springer, 2010, vol. 17.

[118] J. Yang, J. Zhao, F. Luo, F. Wen, and Z. Y. Dong, "Decision-making for electricity retailers: A brief survey," IEEE Trans. Smart Grid, vol. 9, no. 5, pp. 4140–4153, Sep. 2018.

[119] T. Chen, Q. Alsafasfeh, H. Pourbabak, and W. Su, “The next-generation U.S. retail electricity market with customers and prosumers – A bibliographical survey,” Energies, vol. 11, no. 8, pp. 1-17, Dec. 2017.

[120] M. Kohansal, E. Samani, and H. Mohsenian-Rad, “Understanding the structural characteristics of convergence bidding in nodal electricity markets,” IEEE Trans. Ind. Info., vol. 17, no. 1, pp. 124-134, Jan. 2021.

[121] J. C. do Prado and U. Chikezie, “A decision model for an electricity retailer with energy storage and virtual bidding under daily and hourly CVaR assessment,” IEEE Access, in press, DOI 10.1109/ACCESS.2021.3100815.

[122] D. Xiao and H. Chen, “Stochastic up to congestion bidding strategy in the nodal electricity markets considering risk management”, IEEE Access, vol. 8, pp. 202428-202438, Aug. 2020.

[123] U. A. Bhatti, Y. Yan, M. Zhou, S. Ali, A. Hussain, H. Qingsong, Z. Yu, and L. Yuan, “Time series analysis and forecasting of air pollution particulate matter (PM2.5): An SARIMA and factor analysis approach,” IEEE Access, vol. 9, pp. 41019-41031, Feb. 2021.

[124] H. Heitsch and W. Römisch, “Scenario reduction algorithms in stochastic programming,” Comput. Optim. Appl., vol. 24, nos. 2–3, pp. 187–206, Mar. 2003.

[125] PJM Data Miner [Online]. Available: https://www.pjm.com/markets-and-operations/etools/data-miner-2

[126] National Renewable Energy Laboratory [Online]. Available: https://www.nrel.gov/

[127] MATLAB Econometrics Toolbox [Online]. Available: https://www.mathworks.com/products/econometrics.html

[128] J. Lofberg, “YALMIP: A toolbox for modeling and optimization in MATLAB,” in Proc. IEEE Int. Conf. Robot. Autom., New Orleans, LA, USA, Sep. 2004, pp. 284–289.